



Event reconstruction for Dark Photon searches at NA64

Dissertation
zur
Erlangung des Doktorgrades (Dr. rer. nat.)
der
Mathematisch-Naturwissenschaftlichen Fakultät
Fachgruppe Physik
der
Bergischen Universität Wuppertal

vorgelegt von
Srijan Sehgal
aus
Bonn

Wuppertal 2019

Angefertigt mit Genehmigung der Mathematisch-Naturwissenschaftlichen Fakultät der Bergischen Universität Wuppertal

1. Gutachter: Prof. Dr. Bernhard Ketzer
2. Gutachter: Prof. Dr. Jochen Dingfelder

Tag der Promotion:
Erscheinungsjahr:

Acknowledgements

(Rewrite ...) Even though this thesis has my name on the front a number of people were involved in shaping its final form both in person and in spirit.

First and foremost I would like to thank my late grandfather Shanti Sarup Sehgal and grandmother Kusum Sehgal. Their constant motivation and belief in my abilities has and will always inspire me to achieve more.

I am very grateful to Professor Bernhard Ketzer for giving me an opportunity to write my thesis in his group. In spite of my many shortcomings and failures he has always been patient and supportive during the entire time and has been a role model I look up to. I would also like to thank Professor Jochen Dingfelder. I have always admired your lectures and am thankful that you agreed to be my second supervisor.

A special thanks to PhD students Michael Hösgen and Martin Hoffmann for helping with the editing of this thesis. Thank you to Michael for always answering my various questions and solving my problems without which this thesis would have never been completed. A big thanks to the whole AG Ketzer group for both the academic and moral support.

I am grateful to my father Ravi Sehgal, my mother Rajni Sehgal and my brother Sambhav for all the sacrifices they have made. Without their constant support studying at Bonn would have just remained a pipe dream. Lastly, I am thankful to the wonderful set of friends I am lucky to have. Thank you Svenja ,Georgios and Amitayus for the countless Mensa lunches which helped me remain sane throughout the thesis.

Contents

1	Introduction	1
2	Ultra High Energy Cosmic Rays and Neutrinos	7
2.1	Ultra High Energy Cosmic Rays	7
2.1.1	History	7
2.1.2	Origin	8
2.1.3	Propagation	10
2.1.4	Latest results	12
2.2	Ultra High Energy Neutrinos	16
2.2.1	History	16
2.2.2	Origin and Propagation	17
2.2.3	Neutrino Interactions and Detection	20
2.2.4	Latest results	23
2.3	Multimessenger Astronomy	24
3	Extensive Air Showers	27
3.1	Development	27
3.2	Characteristics	31
3.3	Detection	33
4	Pierre Auger Observatory	35
5	Neutrino Analysis $60^\circ < \theta < 75^\circ$	39
5.1	Detectors	39
5.1.1	MicroMegas	39
5.1.2	Gas Electron Multiplier	40
5.2	Track-Reconstruction Algorithm	41
5.2.1	Linear Regression	41
5.2.2	Kalman Filter	42
5.3	CORAL and PHAST	45
6	Neutrino Analysis DGH	47
6.1	Previously used method	47

6.2	Millepede	48
6.3	CORAL Implementation	51
6.4	Results	52
6.4.1	Positional Alignment	53
6.4.2	Angular Alignment	60
6.4.3	Positional+Angular Alignment	63
7	Source follow-up analysis	65
7.1	A' Production	65
7.2	Tracking Detectors	66
7.3	Calorimeters	67
7.4	Trigger Detectors	68
7.5	Reconstruction Results	69
7.5.1	Momentum Reconstruction	70
7.5.2	A' Reconstruction	72
8	Conclusion and Outlook	75
Bibliography		77
A	Testing hadronic models	81
B	Adapting DGH analysis to current Offline	87
List of Figures		89

CHAPTER 1

Introduction

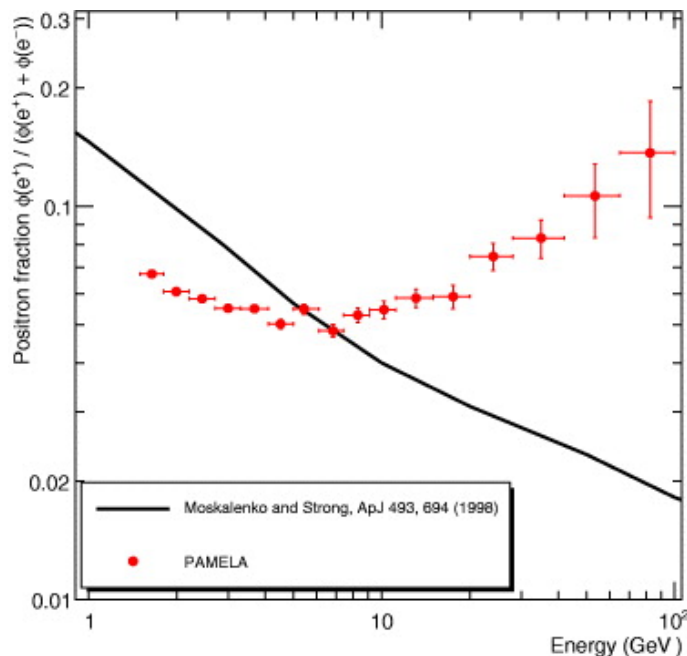


Figure 1.1: Positron fraction measured by PAMELA (red) along with a theoretical model (black) [1]

The need to understand how something works or why something is? is ingrained in every human. While attempting to find answers for these questions one either answers them conclusively or finds oneself asking additional questions stemming from the original. One such question which bothered physicists at the beginning of the 20th century and eventually led to the field of *astro-particle physics* was of so-called "atmosphere electricity" or ionization of air. After the pioneering discoveries by Theodor Wulf [] and Victor Hess [] who found the increase of this ionization rate with altitude and theorized the origin of this radiation to be not Earth but something above our atmosphere, the name *cosmic rays* was coined by Robert Millikan who believed these rays were originating from primary photons. This hypothesis

was rejected by the measurements done by Jacob Clay [] in 1927 who observed a latitude dependence of the intensity of cosmic rays concluding this to be a deflection of the primary cosmic rays by the geomagnetic field of the Earth which indicated that these rays must be charged particles. After this came the efforts of Rossi [], German group [] and Auger [] all independently discovering coincident signals in separated Geiger counters which they explained by the counters being struck by an extensive particle shower triggered by a primary cosmic ray. The phenomenon was named *sciame* by Rossi, *Luftshauer* by the German group and "Auger showers" by Auger and his collaborators. Auger went one step further by further estimating the primary energy of the cosmic ray via his superior setup giving rise to some current unknown mysteries of cosmic-ray physics, how are they created and where are they coming from. One of the known sources which is the Sun is too close to explain some other high energy CRs constantly hitting the Earth's atmosphere. Since then the field has only expanded with numerous experiments set up to characterize these cosmic rays.

The biggest of these experiments which looks for ultra-high energy cosmic rays(UHECRs) exists in 3000 km² patch of Argentinian pampa just outside of Malargue called the Pierre Auger Observatory []. It uses a combination of 1660 Water Cherenkov tanks which form the Surface Detector of the observatory and observe the air shower particles arriving at the ground along with Fluorescence Detectors/Telescopes which can look at the development of shower as it travels through the atmosphere. Built primarily to answer the question of the cut-off of the cosmic ray spectrum also known as GZK(full form cutoff), the observatory has provided immense contributions not only in the field of CRs but also in the fields of Geophysics(elves), something here(edit...) and multi-messenger physics(neutrino+photon searches). Currently, the Surface detector is undergoing an upgrade which will add a scintillator and radio detector on top of the Water Cherenkov tanks further increasing the sensitivity of the Observatory especially to the composition of the cosmic rays.

One of the challenges faced while looking for the sources of the cosmic-rays is the non-electrical neutrality of the incoming CRs. This means that CRs do not travel in straight lines from their sources and are affected by the magnetic fields and can also interact with the matter along the way[]. Combined with the fact that the possible sources are light years away from us without knowing the magnetic fields of the Universe it is very hard to detect the sources of CRs. Ultra High Energy Neutrinos (UHE ν_s) can help in this challenging search for the sources of CRs[]. Being electrically neutral and having a very low interaction cross-section these particles can travel large distances unaffected by the intervening matter and magnetic fields. Several scenarios which are discussed later in ?? describe how the UHE ν_s can be produced by cosmic-rays and can tell us about their sources. Moreover, UHE ν_s are also interesting as they can also help constrain or explain different production and propagation scenarios for various sources helping us see known astrophysical and cosmogenic objects in a new way. The success of Icecube Neutrino Observatory, a neutrino observatory located in the South Pole, in detecting the first astrophysical neutrinos and observations of the first steady source NGC 1068 [] and transient source [] have reinvigorated the whole astro-particle field. The Pierre Auger Observatory has also contributed to the search for UHE ν_s by trying to detect the EASs that can be induced by them. With its stellar sensitivity at high energy,

searches at Pierre Auger Observatory have provided some of the strictest upper limits on the diffuse flux of UHE neutrinos []. This has already led to constraints on various hypothesized models explaining cosmogenic neutrino production.

The last decade with the successes of LIGO/VIRGO [] in measuring the first Gravitational waves and IceCube in detecting the first astrophysical neutrinos has also rekindled a field which displays the true spirit of harmony in science and is called multi-messenger astronomy. The aim of the field is to establish a network that can coalesce all the information available through various messengers via which we can see the Universe and maximise the resources and experiments available at Earth. This also allows us to understand the sources better since the observation or non-observation of different messengers can help constrain the mechanisms behind their functioning. The beginning of this field can be traced back to the observation of the first cosmic rays in conjunction with solar flares further cementing the important role Pierre Auger Observatory can play for this field. One of the most important success stories of this field is the August 2017 detection of the neutron star collision [] first by the LIGO/VIRGO detector since the Gravitational waves are the fastest messengers and then 1.7s later by the Fermi Gamma ray space telescope and INTEGRAL. 11 hours later already alerted by these two experiments the optical counterpart was detected by multiple telescopes like Las Campanas Observatory and the Hubble Space Telescope. The event was also further seen in Ultraviolet(Neil Gehrels Swift Observatory), X-ray(Chandra X-ray Observatory) and radio(Karl G. Jansky Very Large Array). The non observation of neutrinos by both the IceCube and the Pierre Auger Observatory helped reach the important conclusion about the orientation of the jets which is hypothesized to be off-axis i.e. not pointing directly towards the Earth. Since neutrinos and Gravitational waves are the fastest of the messengers to reach the Earth, alerts issued by IceCube and LIGO/VIRGO are regularly used to follow up the events with other experiments. Subsequent observations of the blazar TXS 0506+056 [] with IceCube, FERMI-LAT and MAGIC and the observations of neutrinos from the plane of the Milky Way galaxy [] have helped establish the continued importance of multi-messenger astronomy.

In this thesis performance of one of the upgrades of the Pierre Auger Observatory done in 2013 is evaluated in the context of neutrino search. This upgrade consisted of introducing new triggers called Time over Threshold deconvoluted(ToTd) and Multiple of Positive Steps(MoPS) in 2013 to reduce the muonic background and effectively decrease the energy threshold for the array. Such triggers can be particularly important in the context of neutrino searches between 60° - 75° since they help in getting a better signal background separation. The effect of these triggers for both the diffused and point-source searches is investigated. The thesis also focuses on maximising the previously done neutrino searches in the zenith region 60° - 90° by investigating and updating the analysis presented in [], [].

The thesis is structured as follows, The next chapter ?? gives the theoretical background for UHE cosmic rays and UHE neutrinos and other important messengers with regard to the Pierre Auger Observatory. It also aims to discuss the various theoretical scenarios involved in their production and propagation. The chapter also aims to summarize the important recent results for these messengers and the various interesting open questions for them.

The next chapter ?? describes the phenomenon of Extensive Air showers which is used to indirectly detect both the cosmic rays and neutrinos at the Pierre Auger Observatory. To continue with understanding the detection in a more experimental context the next chapter ?? gives a detailed description of the Pierre Auger Observatory. The objective of the chapter is to try to give an exhaustive description of all the tools at the Pierre Auger Observatory necessary to detect neutrinos with a particular focus on the Surface Detector which is of primary concern for the analysis presented in this thesis. A small section is also dedicated to the recently completed AugerPrime upgrade and the exciting potential it offers especially for multi-messenger searches.

The second part of the thesis is dedicated to the neutrino search in the zenith angular region 60° - 90° . This part begins with the chapter ?? that gives a description of the neutrino search in the angular range 60° - 75° which is also the primary focus region for this thesis. The chapter is dedicated to provide a complete description of the choices made for the analysis with the proper reasoning. It reports the areas of potential improvements and also communicates the observed improvements to the neutrino search with the new triggers. A new *blind* search is performed to look for neutrinos in the data recorded at the Pierre Auger Observatory. The results are summarised at the end of this chapter and due to the non-observance of any neutrino like events, the corresponding limits to the neutrino flux are presented. The next chapter ?? intends to do the same for the zenith angular range 60° - 75° . The analysis is split into these two angular regions because of a difference expected neutrino signature in the detector and to maximise the probability of detecting neutrinos at the Observatory. The Observatory can also detect up-going showers in the zenith angular region 90° - 95° with the Surface Detector and 90° - 180° (???) with the Fluorescence Detector, but these searches are not performed in this thesis and only their final results are included to for comparison and to provide a holistic feel for the neutrino search at Pierre Auger Observatory.

The last part of this thesis presents an example of a neutrino follow-up analysis for the source (blabla) in chapter ???. Due to the non observance of any neutrinos in the data at the Pierre Auger Observatory an upper limit set by this analysis is also provided for interesting point source neutrino candidates. All the important results are the finally summarised in chapter ?? and a short outlook of the future directions for the analysis and the neutrino search at the Pierre Auger Observatory is put forward. The dissertation is completed by three appendices. The first describing the independent work done to compare the various hadronic interaction models for neutrino simulations and the second contains a technical overview of the changes made to implement the 60° - 75° neutrino search within Offline, the software framework of the Pierre Auger Observatory. Maybe will also add Fisher information later in the Appendix.

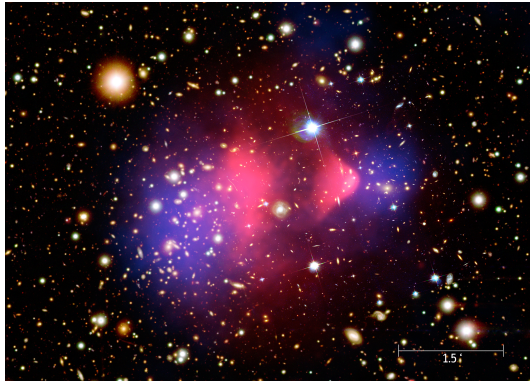


Figure 1.2: Composite image of the bullet cluster. The x-ray emission recorded by Chandra telescope is shown in pink. The blue overlay is the mass distribution of the clusters calculated from gravitational lensing effects. [2].

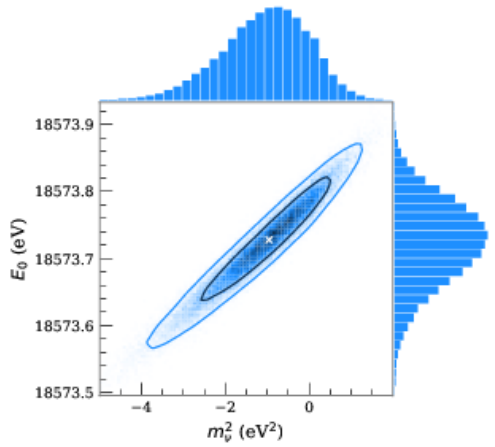


Figure 1.3: Scatter plot of fit values for the neutrino mass square and the effective β -decay endpoint E_0 together with 1- σ (black) and 2- σ (blue) error contours around the best fit point (cross). [3]

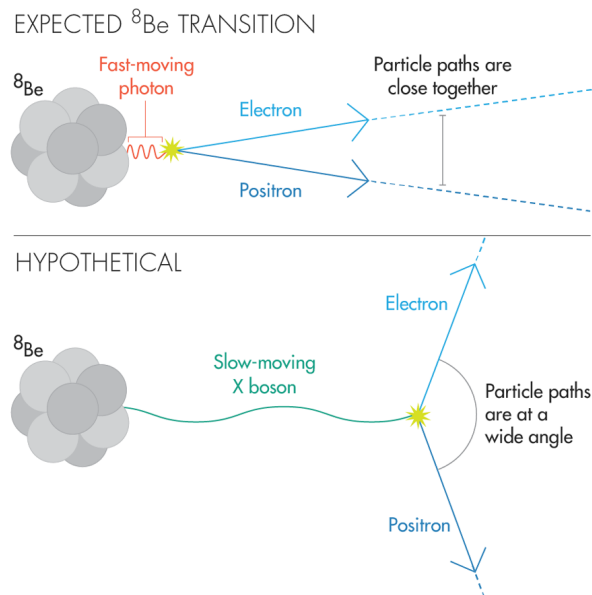


Figure 1.4: Hypothesized X17 Boson production [4]

CHAPTER 2

Ultra High Energy Cosmic Rays and Neutrinos

2.1 Ultra High Energy Cosmic Rays

2.1.1 History

As already mentioned in the introduction cosmic rays have been a source of investigation for more than a century now. Even before the balloon flight by Victor Hess it was Henry Becquerel, the discoverer of radioactivity who believed that the *atmospheric electricity*(ionization of air) was due to the radioactive substances present on Earth. In such a scenario the ionization rate should decrease the higher up you go in the atmosphere. The first measurements disproving this theory were performed by Theodor Wulf in 1909 with his own developed electrometer. His measurements published in the *Physikalische Zeitschrift* indicated a higher level of radiation at the top of the Eiffel Tower as compared to its base. Unfortunately the measurements were not widely accepted, and it would take three years till Victor Hess via his several balloon flights provided irrefutable measurements corroborating Wulf's observations.

Between 1911-1912 Victor Hess performed nine(2 in 1911 and 7 in 1912) balloon flights going as high as 5350m a.s.l to measure the dependence of ionization rate to altitude. He carried with him three Wulf electrometers, two tuned for γ rays and the third tuned for β rays [](1808.02927) which along with α were the only three known radioactive decays. His measurements published in the Proceedings of the Viennese Academy of Sciences [] showed that the radiation level decreased slightly up to a certain altitude (1 km) but after this height the radiation increased significantly and at the highest flown altitudes reached levels about twice in comparison to the ones at sea level. Some of his measurements were done during the night and one during a partial solar eclipse which further made him rule out Sun as a source of this radiation. With further confirmations via the measurements by Werner Kolhörster in 1914 and Robert Millikan, in 1925, Victor Hess was awarded the Nobel Prize in Physics in

1936.

Cosmic rays were still presumed to be gamma rays. This supposition was quickly negated by the efforts of Jacob Clay who via his measurements of the cosmic ray intensity at different latitudes by while sailing from Java to the Netherlands in 1927 [] showed that the geomagnetic field had a significant effect on the intensity. Further observations of the *East-West* effect, the directional dependent intensity due to the charge of the primary cosmic rays, predicted by Bruno Rossi [], by various experiments [] [] concluded that the intensity was greater from the west proving that cosmic ray primaries have a positive charge.

Today we use Cosmic Rays (CRs) to describe the highly energetic charged particles/nuclei travelling at very high speeds through space. The Earth is constantly bombarded by CRs some originating from the Sun but most of them from outside our Solar System. In more than 100 years since Victor Hess's balloon flight we have gathered a lot more information and have achieved a better understanding of CRs. We have detected CRs to energies 10^{20}eV which is an impressive feat since at these energies the expected flux drops below one particle/ km^2 . We know a lot more about the composition of the CRs and have also proposed models explaining their origin and their journey to Earth. CRs continue to be a source of fascination. Some of the achievements are summarised below along with some unanswered questions about CRs.

2.1.2 Origin

To understand the sources for cosmic rays one needs to understand the mechanisms that could impart huge amounts of energies to the tiny particles that actually reach the Earth. We already know that the low energy cosmic rays which reach our Earth are predominantly coming from the Sun. The evidence for this comes from the observation of an increase in these with a coincidence to violent activity of the sun. Most of the CRs and UHECRs do not exhibit this temporal coincidence and are thought to have been originated in our Galaxy or beyond respectively. There are two different mechanisms which could explain how the cosmic rays particles are accelerated to such high energies over large distances: *bottom-up* and *top-down*. The *top-down* approach assumes that the UHECRs are produced due to the decay or annihilation of extremely massive or exotic particles. Both of these mechanisms have been investigated with various experiments including the Pierre Auger Observatory. With the current observations the top-down models face significant challenges. The extremely high energies required for the annihilation of the hypothesised exotic particles and the lack of evidence for their existence makes it very difficult to both verify and rule out the top-down mechanism. The continued improvement in understanding of astro-particle physics and the early universe makes the study of UHECRs an exciting and active area for research with the mystery of their origin and propagation still looking for a solution.

Bottom-up scenario

There are many proposed ways in which CRs could get accelerated by astrophysical sources. One of the most widely accepted explanation which can explain most of the observed CRs

which originate from our Galaxy is the diffusive shock acceleration also known as Fermi acceleration. Qualitatively one can explain Fermi acceleration as follows: When a massive star reaches the end of its life cycle it can undergo a supernova explosion. During this the star core collapses and an intense shockwave propagates outwards towards the star's outer layers. As the shock wave progresses and moves through the interstellar medium (ISM) it sweeps up and compresses the surrounding gas and magnetic fields creating a region of very high pressure and magnetic turbulence known as the shock front. The charged particles can get trapped in such a shock front and repeatedly cross over this region of magnetic turbulence experiencing magnetic irregularities and constantly changing direction in a collision-less way thus experiencing electric fields each time they cross which accelerate them to higher energies. An illustration is shown in fig. The shock front is turbulent, and particles can cross it multiple times, gaining energy at each passage. Eventually some particles can acquire enough energy to escape the shock region and travel the required distances to reach the Earth. Such an explanation can explain the CRs originating in our Galaxy and point towards supernovae and its remnants as potential sources but to explain the UHECRs ($>10^{19}$ eV) we need other sources and mechanisms. The energy that can be produced by the accelerator is limited by the gyroradius of the accelerator. This has been illustrated by Hillas [] where he illustrated the potential sources of CRs on a plot of magnetic field strength vs size. A modified version of his original plot with inclusion of modern sources is shown in fig. 1.2.

Other accelerating mechanisms are as follows:

1. Supernova Remnants: Interactions of CRs with the magnetic fields within the remnants could lead to further acceleration.
2. Active Galactic Nuclei (AGNs): These are regions in the center of galaxies that are capable of producing highly energetic particles. The source of this capability is theorised to be supermassive black holes. The extreme conditions near the black holes such as strong magnetic fields and high-energy jets could accelerate UHECRs.
3. Magnetar Outbursts: Magnetars are neutron stars having a magnetic field 1000 times that of a normal neutron star. They are known to produce magnetically powered bursts which could potentially accelerate particles to UHECR level energies.
4. Pulsar Wind Nebulae: Rapidly rotating neutron stars, also known as Pulsars emit beams of electro-magnetic radiation. Such beams can collide with ISM creating a pulsar wind nebulae, a region similar to a shock wave front and can lead to production of UHECRs.
5. Galaxy Clusters: These are regions of massive galaxy populations bound together by gravity. These highly dense structures can accelerate particles either by themselves or via the shock waves associated with a potential merging of different galaxy clusters.
6. Relativistic shocks: Other type of astrophysical shocks such as those occurring in gamma-ray bursts or colliding stellar winds could also create scenarios which could accelerate particles to UHECR level energies.

The validity of all such hypothesised mechanisms can be checked by corroborating their spectral index predictions with that observed by the experiments.

citations
needed

Citations
needed ...

Top-down scenario

This is an alternative approach to explain UHECRs. The main idea behind these models is that the UHECRs are produced due to the decay or interaction of hypothetical, supermassive, or exotic particles that were produced in the early universe. Some of the proposed hypothesis are mentioned below:

1. Supermassive Dark Matter Particles: This is an extension of a concept that was first proposed to explain dark matter. In this hypothesis it is assumed that dark matter is composed of long-lived supermassive particles. If such particles exist they could potentially decay and produce UHECRs.
2. Cosmic Strings: These are one-dimensional topological defects which could have formed during phase transitions in the early Universe. The decay of these massive strings could also lead to production of UHECRs.
3. Other Topological effects: These include defects like monopoles or domain walls which could also produce exotic particles which can further decay into UHECRs.

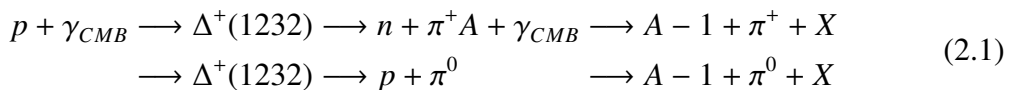
There are other scenarios such as breakdown of Lorentz invariance which attack the problem of UHECRs not by suggesting a new mechanism for their production but their propagation which can also have a major effect to the observations of CRs and UHECRs we observe at Earth. Some of these models can be constrained by again looking at the flux of the UHECRs. There are also experiments which try to directly look for these exotic particles [1]. So far, no evidence has been found to support the existence of these particles.

2.1.3 Propagation

However, production is just one part in the life of a CR/UHECRs. To get detected at Earth the CRs and UHECRs have to travel large distances through ISM during which they can suffer various losses which ultimately affects the spectrum we see on Earth. Some main processes include losses by ionization due to collision with ISM, Coulomb Scattering which can cause random changes to the direction, Synchrotron Radiation which can lead to emission of high energy photons and, consequently, energy loss for the cosmic ray particle and through collisions with high-energy photons from radiation fields leading to breakage of CR nuclei also known as Photodisintegration. Other propagation effects such as Bremsstrahlung and Inverse Compton Scattering due to interactions with the cosmic microwave background radiation(CMB) are the reasons high energy cosmic ray electrons cannot propagate large distances. Few other mechanisms include Adiabatic Energy Loss which can occur when a CR particle traverses through regions of high pressure or magnetic field strength to regions of lower pressure and magnetic field strength leading to a decrease in its velocity, Scattering due to going through magnetic turbulent areas or even an escape of UHECRs from our Galaxy can all affect the spectrum of CRs and UHECRs we see at Earth. One of the critical phenomenon to understand the cosmic ray propagation and to realize a theoretical limit to the energy of UHECRs is the Greisen-Zatsepin-Kuzmin (GZK) cutoff. This is discussed in more details below.

GZK Limit

The GZK cutoff was first proposed by Kenneth Greisen, an American physicist in 1966 in a paper titled "End to the Cosmic-Ray Spectrum?" [1]. He discussed the potential energy loss of high-energy cosmic rays due to interactions with the CMB. He calculated a threshold energy above which cosmic rays in his case protons would lose energy through interactions with CMB. In the same year, two Soviet physicists, Georgiy Zatsepin and Vadim Kuzmin, arrived at a similar prediction. Their calculations published in their paper "Upper Limit of the Spectrum of Cosmic Rays" [2] were consistent with Griesen's work and reinforced the concept of GZK cutoff. The energy cutoff calculated is about 5×10^{19} electronvolts(eV) or about 8 joules. The dominant mechanisms via which the proton can interact with the photons of the CMB are given below.



These processes are also called "Photopion Production". The thresholds for these reactions are of the order of a few hundred MeV for protons and GeV per nucleon for other nuclei. The predicted cutoff for protons is 50 EeV whereas for heavy nuclei it can range from about 80 EeV to several hundred EeV depending on the mass of the incident nucleus. The mean free path which represents the average distance a cosmic ray particle can travel before undergoing a significant interaction is 6Mpc for protons. This leads to the outcome that if a UHECR proton with energy above the GZK cutoff travels over a distance larger than 50Mpc then such a proton will suffer catastrophic losses and will never be observed on Earth. However, this consequence doesn't hold for heavy nuclei since for them Photopion production is not the dominant process via which they can lose energy. For ultra-high-energy cosmic rays (UHECRs) composed of heavy nuclei (e.g., iron, uranium), the dominant energy loss process during their propagation through the universe is photodisintegration. It can be described as:



The mean free path is still of the order of 10Mpc. Even though, Pierre Auger Observatory observes a suppression in the cosmic ray spectrum above the GZK cutoff [3], it does not claim it to be just due to GZK limit. It has also observed cosmic rays above the GZK cutoff. This issue along with its implications is discussed later in ???. One of the other consequences arising from the interaction with the CMB is interaction of high energy photons(gamma rays) to produce electron-positron pairs, $\gamma_{UHECR} + \gamma_{CMB} \longrightarrow e^+ + e^-$. This is an important consequence which alters both the expected UHECR spectrum and the CR spectrum at Earth and also just leaves UHE ν as one of the only known cosmic ray particles which can point back directly to their sources.

The production of UHE ν arising from the pions produced during the Photopion interaction are discussed later.

2.1.4 Latest results

The study of CRs to constrain their properties and the relevant sources requires measurements on Earth. The measurements which provide valuable information are the energy spectrum or flux observed at Earth, composition of the primary CRs arriving at Earth, their arrival direction and other relevant observations such as measurement of other messengers such as high energy photons and neutrons. These measurements and their implications are discussed in more detail below. The UHE ν , relevant for this thesis are discussed in a separate section.

Cosmic Ray spectrum

The cosmic ray spectrum measured by several experiments on Earth is summarised in figure. ???. Extending in energy from a few 100 MeV(solar CRs) it spans about 12 orders of magnitude up till the highest observed CRs 10^{20} eV. The flux decreases with increasing energy and follows a varying power law description:

$$\frac{dN}{dE} \propto E^{-\gamma} \quad (2.3)$$

where γ is the spectral index. The spectral index varies between 2.7 to 3.3 as measurements are made for higher energies. This signifies a decrease in the observed flux as the energy increases. The flux falls from $\sim 1m^{-2}s^{-1}$ at 10^{11} eV to $\sim 1m^{-2}yr^{-1}$ at 10^{16} eV to about $\sim 1km^{-2}yr^{-1}$ at 10^{19} eV. Such a steep fall also poses challenges for the experimental design and the corresponding size. This also affects the detection mechanisms employed to measure this spectrum, due to the very low flux expected at high energies, the measurements of the direct primaries becomes nearly impossible and an indirect detection using the property of the cosmic ray to trigger an air shower in our atmosphere is employed. This phenomenon and how it is used to measure CRs is discussed in the next chapter ??.

To better deduce the features in the cosmic ray spectrum one can scale the flux in the fig ?? by energy. The corresponding figure is shown in Fig. ???. Below 10^{13} eV CRs from the Sun dominate the spectrum. The galactic or extragalactic CRs of these energies cannot enter our solar system because of a variety of reasons. These include a combination of the Heliosphere, Termination Shock and solar modulation which block the low energy CRs. The Heliosphere which is a region influenced by the Sun's magnetic field and solar wind acts as a protective bubble around the solar system. Beyond the Heliosphere, the solar wind interacts with the ISM creating a region of termination shock which can cause scattering and deflection for incoming low energy CRs. Additionally, the solar activity cycle can cause changes to the Heliosphere which in turn also affects the incoming CRs. Beyond a few GeVs the Sun as a source of CRs drops off due to reaching its maximum acceleration. Between 10^{13} eV and 10^{18} eV the spectrum is dominated by CRs of galactic origin. This has been verified by comparing the spectral indices of the proposed acceleration mechanisms with the measured spectrum as mentioned before. A second proof also comes from the composition of the CRs observed in these energies but this is discussed later. *Supernovae and supernovae remnants*

remain the most promising sources which could explain their origin. The spectral index $\gamma \sim 2.7$ gives a good description of this region. Around 5×10^{15} one observes a steepening of the spectrum known as the *knee*. At this point the spectral index γ changes from 2.7 to 3.1. This is attributed to the galactic accelerators reaching their maximum potential for accelerating protons. Above the knee the sources are expected to reach their maximum potential for other heavier particles until galactic sources cannot accelerate CRs any further. This point is thought to be the origin of the second knee at 10^{17} eV. At this point the γ changes from 3.1 to 3.3. This is theorised to be a transition region in which the spectrum is believed to change from one of galactic origin to extragalactic origin. This region ends at about 10^{18} eV whereon the spectrum hardens noticeably to a $\gamma \sim 2.6$, originating what is referred to as the *ankle*. Further, with increasing energy the spectrum again steepens to $\gamma \sim 5.1$ reaching an eventual cutoff. The suppression of flux at these energies and the cutoff is still not properly understood yet and could be due to the following possibilities.

1. GZK Limit: One of the most prevalent ideas behind the suppression and the cutoff is the GZK mechanism which was discussed above. Due to the observations of CRs above the cutoff of 10^{19} eV by the Pierre Auger Observatory and a non-observance of expected composition(non proton primaries) and neutrino flux(GZK pion decay), GZK as the only reason for the observed cutoff in the spectrum is currently disfavored. However, tensions between the composition measurements of the Pierre Auger Observatory and the Telescope Array(TA), second-largest CR observatory, makes this topic still a subject of debate.

2. Maximum Rigidity: In this scenario the cutoff is due to the sources of the extragalactic CRs reaching their maximum potential for acceleration for different particles i.e maximum rigidity. Such a scenario is already observed in the spectrum for Galactic sources(*knee*). An indirect proof of this mechanism can come from the observed composition from the *ankle* region to the cutoff. If the composition shifts from lighter to heavier nuclei this would be a proof of a cutoff at the potential extragalactic sources.

3. Photo-disintegration: This effect was also discussed before in sec. ???. However, for such a scenario the cutoff would appear in steps depending on the mass of the nuclei.

It is likely that the cutoff and the suppression is not just because of one of the above-mentioned scenarios but is due to a combination of all the three. In theory, GZK and Photo-disintegration could explain the observed spectrum but the non-observance of GZK neutrinos and the composition measurements gather otherwise. It also shows that even though the CR spectrum gives a very nice overview other crucial measurements of composition and multi-messengers play an equally important ally to the spectrum measurements for constraining the origin and propagation of CRs.

Cosmic Ray composition

The types of particles the cosmic ray flux at Earth is made up of is called the cosmic ray composition. Such measurements with respect to energy offers a very useful insight into their origin. Direct measurement of the primaries is only possible for low energies and one e.g. is the AMS detector at the International Space Station []. For higher energies the mass of

the primary is reconstructed by measuring the phenomenon of Extensive Air Shower(EAS) which is described in more detail in Chapter ???. EASs are created when high-energy cosmic rays interact with the Earth's atmosphere producing a cascade of particles resembling a shower. Depending on the mass of the primary, the EAS induced in the atmosphere by the said primary has characteristic differences. For the same energy lighter nuclei such as protons will interact and produce an EAS much deeper in the atmosphere compared to heavy nuclei such as iron. There are various ways one could estimate the mass of the primary. The estimator used for this at the Pierre Auger Observatory is $\langle X_{max} \rangle$ which is the average depth at which the EAS development in the atmosphere reaches a maximum. The $\langle X_{max} \rangle$ values are also energy dependent, and it is observed that iron nuclei typically have values 100 g cm^{-2} lower than proton. The fluctuation in the spread can also be used to gauge the mass. For e.g. fewer fluctuations are expected for iron compared to proton. Other quantities such as the lateral distribution of the shower which is just the number of particles in a shower as a function of distance from the point of first interaction (core) also shows differences based on the primaries. For lighter primaries the distribution is broader i.e the number of particles decrease more gradually with distance from the core compared to a narrower distribution in the case of heavier primaries. The ratio of electromagnetic to muonic components first used by KASCADE [] can also be used to differentiate between the primaries, the lighter primaries have a greater electromagnetic component whereas the heavier primaries have a greater muonic component in the initiated EAS.

The process of estimating the mass requires a very robust simulation that can reconstruct an EAS perfectly for a certain primary and a direct observation of X_{max} . At the Pierre Auger Observatory The Fluorescence Detector, cf. chapter ??, is used to directly measure the X_{max} on an event by event basis. The recent results from the Pierre Auger Observatory are shown in fig ???. In both the figures the composition initially turns lighter and then seems to change from lighter to heavier nuclei at E 18.5 EeV. This could be an indication of the switch from a galactic component to an extragalactic component around the *ankle* and then the maximum rigidity scenario as mentioned in the section above.

However, the duty cycle of the Fluorescence Detector 14% compared to the Surface detector 100% leads to very limited statistics. Currently, this problem is solved by defining a new observable described in [](1710.07249.pdf) which has helped increase the number of events used to estimate the mass composition by nearly 14 times. The results for this are shown in fig ???. Additionally, the energy dependent mass composition can be fitted simultaneously with the cosmic ray spectrum observed at the Pierre Auger Observatory with the only required assumption being about the model used to produce and propagate the cosmic rays from the sources. The result of one such analysis [] is shown in fig ???. With the current Pierre Auger Observatory measurements for different mass components are required to best described the data with proton component completely disfavored for highest energies.

re-write
after look-
ing at the
paper

The future advancements of the AugerPrime which will further increase the capability of the Pierre Auger Observatory in measuring the mass composition. The addition of a Radio Detector can present an independent measurement of the X_{max} offering an important

crosscheck on the Fluorescence Detector measurement.

Cosmic Ray arrival directions

Even though, the CRs are mostly charged particles and can easily get deflected by the magnetic fields [] present in the cosmos one can still estimate the arrival directions of these CRs with the help of a good pointing resolution and an understanding of these magnetic fields. The pointing resolution depends on the detector and the Pierre Auger Observatory already has an excellent pointing accuracy of 0.7° . The magnetic fields on the other hand are complicated to deduce and model. However, this lack of knowledge can be ignored by just looking at CRs of high energies since the expected deflections for such cosmic rays are expected to be small. At Pierre Auger Observatory the arrival directions of more than 2,600 CRs above 32EeV were estimated and analysed to look for potential sources of these CRs []. The results are shown in fig. ?? The figure clearly shows the presence of Anisotropies which are deviations from uniformity across the sky. The annisotropies are also pointed away from the Galactic centre indicating that the UHECRs have an extragalactic origin. The hypothesis is further confirmed by the increase in anisotropy with energy shown in []. The presence of these anisotropies not far from the Galactic spiral arm as shown in fig ?? also give a further proof of an extragalactic origin of these UHECRs. Further, for low energies $E > 0.03$ EeV studies looking at large scale structures such as dipolar flux modulation in [] also show a shift of the anisotropy dipole more towards the galactic center with decreasing energy with a significance of 6σ . This can again be interpreted as a transition in CR sources from Galactic to extragalactic component. Even though this result is corroborated by the measurements done by KASCADE-Grande, IceCube and IceTop due to the decrease in sensitivity of the Pierre Auger experiment for these energies the result is not conclusive yet.

Some proposed sources for these UHECRs due to observations of excess UHECRs in their surrounding regions by the Pierre Auger Observatory are presented in [](ICRC proceeding). These include the Centaurus A region(4σ significance), starburst galaxies(3.8σ) such as NGC4945, M83 and NGC253. The Telescope Array has also found an excess close to the Perseus-Pisces supercluster(PPSC) with a significance of $3.0\text{-}3.2\sigma$. However, this is has been negated by the Pierre Auger Observatory and remains a topic of discussion. With the continued data taking and upgrade of the Pierre Auger Observatory the excess in the Centaurus A region is expected to reach a 5σ significance by 2025 which could make it the first steady source of UHECRs ever observed.

Other Messengers

The scenarios for the production and propagation of CRs discussed above also predict production of other messengers such as photons, neutrinos and neutrons. Neutrons and photons are discussed in this section while neutrinos in section ref. Neutrons being neutral and thus not affected by the magnetic fields of the Universe during their propagation can be useful for arrival direction studies. They are expected to be produced at the CR source

via photopion production or other nuclear reactions near the sources. One such e.g. is a collision between a ultra high energy proton to an ambient proton/photon []. Although, neutrons can lose significant amount of their acquired energy very quickly via β decay(mean lifetime 879 s) [] but in the ultra-relativistic regime neutrons originated in our Galaxy can still make it to Earth. At Auger, a neutron produces a non-distinguishable EAS as compared to a proton. Hence, only a source catalog correlated search can be performed at the Pierre Auger Observatory. The results of such a search are given in [](ICRC proceeding). No neutron like events have been found at Auger, but these results have already helped constrain some theorised production mechanisms for CRs. Future searches looking at transient or short-lived sources for neutrons are currently underway. Photons again offer another window to look into the origin, propagation and the sources of the CRs. They can either be produced via interactions of CRs with matter or radiation fields or during propagation through interactions with the CMB as mentioned in sec. 2.1.3. They along with neutrinos can also help constrain various top-down scenarios and help paint a more complete picture of the CR landscape. Observations for high energy photons have been carried out by specialised experiments such as ground-based Cherenkov telescopes like the High Energy Stereoscopic System (HESS) [], Fermi Gamma-ray Space Telescope, and the upcoming Cherenkov Telescope Array (CTA). The Pierre Auger Observatory can also contribute to this search in the ultra high energy regime by looking for proton induced EAS. Such EASs are expected to be different from the ones induced by CRs as they have a larger electromagnetic component and a rather small hadronic component. A more detailed description of the signature is provided in []. The results of a photon search performed at the Pierre Auger Observatory has been summarised in fig ?? together with the predicted flux from some popular production models. Due to the on-observance of photon like events at Auger the collaboration has set some of the stringiest limits for expected photon flux at high energies. This has already helped constrain some top-down scenarios ultimately leading to a much better understanding of the origin of UHECRs. Further, searches will also help constrain the mystery of the cutoff. UHE photon searches are also very useful for a multimessenger approach to astronomy and these contributions are discussed more in section ??.

2.2 Ultra High Energy Neutrinos

2.2.1 History

Neutrino(ν) [] (neut-neutral, ino-small) is an elementary particle belonging to the fermion class with a 1/2 spin. It was named by Enrico Fermi but first postulated by Pauli in 1930 as an explanation for conservation of energy, momentum and angular momentum in β decays. It rarely reacts in nature and only scatters via weak interaction. The neutrino was first observed in 1956 by the Cowan–Reines neutrino experiment [] by detecting the annihilation of neutron and positron produced by antineutrinos created in a nuclear reactor. Neutrinos can have three flavors electron neutrinos (ν_e), muon neutrinos (ν_μ), or tau neutrinos (ν_τ) depending

on the charged lepton (electron, muon or tau) accompanying them in their production. There are various mysteries involved with understanding this "ghost particle. One of these is the phenomenon of neutrino oscillations which is the intermixing of different neutrino flavors as it propagates through space. This has been observed in various experiments such as the Super-Kamiokande Observatory [] and the Sudbury Neutrino Observatories [] and was the recipient of the 2015 Nobel Prize for Physics since it was the first indication that neutrinos have some mass. This has led to various efforts to determine the mass of the three neutrinos []. Currently, only a hierarchical differentiation can be established [], the configuration of which is also not completely understood, and further experiments like Karlsruhe Tritium Neutrino experiment [] are underway to solve this mystery. Also, the very mechanisms with which neutrinos can acquire mass are currently not completely understood []. Neutrinos arriving at Earth through astrophysical sources such as the Sun have also played an important role in increasing our understanding of CRs and physics in general. The solar neutrino observations ultimately led to the postulation and discovery of neutrino oscillations. The observations of neutrinos from SN 1987A, a type II supernova in the Large Magellanic Cloud by Kamiokande II [] before the observation of any other messenger marked the dawn of non-solar neutrino astronomy and displayed the importance of neutrinos for multi-messenger physics. One of the most important experiment for this field has been the IceCube Observatory. Located at the South Pole the IceCube Observatory has revolutionised both neutrino and multi messenger astronomy. It has led to the first detection of astrophysical neutrinos [] and provided a measurement of their spectrum for high energies []. It has also contributed to the study of the neutrino oscillations[] and its mass hierarchy []. Recently, IceCube has further found the first source of steady state neutrinos in our cosmos which is the NGC1068 [] and has also led to the groundbreaking measurement of the neutrino spectrum from our Galaxy []. These results and their implications are discussed in more details in section ???. Its contributions to multi-messenger astronomy are also discussed later in section ???. For the highest of energies the Pierre Auger Observatory remains the only facility capable of detecting neutrinos. Neutrinos can help to understand various astrophysical processes such as the Big Bang where the neutrinos are hypothesised to have decoupled 1 second after leading to cosmic neutrino background (CNB) [] to the nuclear processes inside stellar objects. Each such process speculates a unique neutrino spectrum which can be probed with experiments to garner their viability. Figure ?? shows the unified neutrino spectrum with respect to energy. For this thesis the following sections are constrained to only the neutrinos of the highest energies(UHE ν) above 10^{16} eV. How neutrinos can help decipher the mysteries of UHECRs is also discussed below.

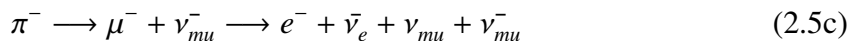
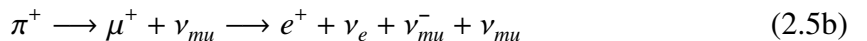
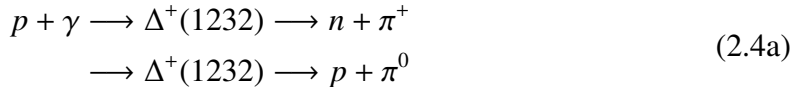
2.2.2 Origin and Propagation

UHE ν_s can be broadly classified to three categories based on their origin. These are astrophysical, originating from known/hypothesised astrophysical sources, cosmic/cosmogenic, originating from the interactions of UHECRs with the CMB or the Extra galactic Background light(EBL) and exotic, emerging from processes such as the Big-Bang, dark matter

annihilation etc. The reactions for the mentioned processes are as follows:

Astrophysical Neutrinos

Astrophysical neutrinos are thought to be produced by or around known sources of UHECRs. The most important ingredient that is required to produce $\text{UHE}\nu_s$ is the interactions of high energy protons and nuclei with matter or radiation fields which results in a photo-meson production followed by a charged pion decay. The decay length of pions is much shorter than the distances of the sources to Earth thus they decay and give rise to secondary neutrinos.



Other interactions such as Neutron Decay ($n \longrightarrow p + e^- + \nu_e$), electron/positron capture and β decays can also contribute to neutrino production. In most of these scenarios the expected flux ratio per flavor can be either $\nu_e : \nu_\mu : \nu_\tau = \bar{\nu}_e : \bar{\nu}_\mu : \bar{\nu}_\tau = (1 : 2 : 0)$ or $(1:0:0)$ with no direct known process for ν_τ production at the source. However, since neutrinos can oscillate which is a consequence of the mixing between the flavor $|\nu_\alpha\rangle$ and mass eigenstates $|\nu_i\rangle$ of neutrinos, given by the following relation:

$$|\nu_\alpha\rangle = \sum_i U_{\alpha i} |\nu_i\rangle \quad (2.6)$$

where $U_{\alpha i}$ is the mixing matrix formulated by Pontecorvo-Maki-Nakagawa-Sakata (PMNS) [1]. In a standard case where three neutrino flavors are considered this matrix is a 3x3 matrix parameterised by the three mixing angles ($\theta_{12}, \theta_{23}, \theta_{13}$) and a single phase called δ_{CP} . Starting from the expected source flavor ratio one can calculate the flavor ratio at Earth by knowing the above four mentioned parameters. One example of such propagation is shown in fig. ???. Since high energy tau neutrinos are not expected to be present in the atmospheric neutrino background the detection of such neutrinos at Earth could be an indication that the neutrino had an astrophysical origin.

Another important aspect to fully understand the origin and propagation of astrophysical neutrinos is determining the expected energies these neutrinos can acquire. On average the energy fraction that pions can get from the CR nucleons is about 20%. These relativistic pion

can then further pass on between 20-26% depending on the flavor and type of the neutrino. Approximately, the Energy fraction for the produced neutrinos in relation to the gamma and Nucleon is:

$$\langle E_\nu \rangle \simeq \frac{1}{2} \langle E_\gamma \rangle \simeq \frac{1}{20} \langle E_N \rangle \quad (2.7)$$

Depending on the type of source and how far the said source is one can calculate the maximum energy potential for sources. With the measurement of the diffused astrophysical flux ?? by IceCube upto 10^{16} eV these calculations can be directly constrained by measurement []. Since extra galactic sources can produce UHECRs upto 10^{20} eV which is corroborated by measurements of the Pierre Auger Observatory one can calculate an upper limit to the diffuse flux for neutrinos. Some of these calculations can be found in [] for Starburst galaxies, [] for AGNs and [] for Magnetars. The non detection of $\text{UHE}\nu_s$ at Auger can thus also act as an important tool to constrain the production mechanisms hypothesised for these sources. The potential of this is discussed later in section ??.

Cosmogenic Neutrinos

Cosmogenic neutrinos are produced due either as a consequence of the GZK mechanism discussed in section 2.1.3 or due to the interactions of UHERs with EBL. They were first suggested by Berensinsky and Zatsepin in 1969 []. The processes involved are similar to those for astrophysical neutrinos albeit the proton/nuclei interact with the CMB/EBL photon instead of the photons from the radiation fields. The two main processes are the same as that for the GZK mechanism i.e. photo-pion production 2.1 and photo-disintegration 2.2. CMB mainly affects the protons [] during their propagation which form a large fraction of the UHECRs traversing the universe while the EBL plays an important role in the case of other nuclei []. Since the process are the same the flavor flux expectations at Earth remain the same. However, the expected energies that the cosmogenic neutrinos can acquire differ drastically as compared to astrophysical neutrinos. The energy threshold for neutrinos produced due to interactions with CMB in the case of photo-pionproduction is of the order of 10^{18} eV while for photo-disintegration it is of the order of 10^{18} eV [](1505.04020.pdf). In case of interactions with EBL this lowers to about 10^{15} eV and 10^{14} eV for the two types of interactions. The exact properties of the neutrinos produced are directly dependent on the parent UHECRs which produce them. The properties of UHECRs such as the total flux, composition, maximum energies, production spectrum at the sources and their cosmological evolution(adiabatic losses) are all crucial factors which affect the secondary cosmogenic neutrinos produced by these UHECRs. A collection of some example of the expected cosmological fluxes for different scenarios can be found in [] []. An example is also shown in fig ???. The two distinct humps are due to the two associated production processes with the lower one being the photo-disintegration.

Measurements of cosmic ray observatories such as the Pierre Auger Observatory can also be used to calculate an expected neutrino spectrum based on assumptions on the composition and the cosmological evolution of the sources. Neutrinos thus can act as a very important

tool in constraining the composition of the incoming UHECRs and further their actual sources. They can also help to solve the question of the cutoff observed in the UHECR spectrum whether this is due to the GZK mechanism(proton dominated composition) or sources reaching their maximum potential as theorised by Hillas(mixed composition). The current results regarding this important study are discussed in the next section ??

Exotic Neutrinos

Neutrinos can also be produced as a result of self-annihilation or decay of dark matter particles. In dark matter annihilation scenarios, two dark matter particles come together and annihilate, leading to the production of standard model particles as a result. The specific flux of the neutrino depends on the properties of the dark matter particle. One such candidate for such a process could be a Weakly Interacting Massive Particle (WIMP), that is its own antiparticle (a Majorana fermion). In regions with a high concentration of dark matter, such as the centers of galaxies or galaxy clusters, WIMPs can come together and annihilate into standard model particles []. One of the annihilation channels of interest for producing very high-energy neutrinos is the annihilation into pairs of intermediate bosons, such as W^+W^- (W-boson pair), or Z^0Z^0 (Z-boson pair). These intermediate bosons can subsequently decay into quarks, leptons, and other particles, including neutrinos. The final state neutrinos can be very high-energy, potentially reaching energies in the PeV (peta-electronvolt) range and beyond. For dark matter decay a stable dark matter particle is supposed to spontaneously transform to other standard model particles including neutrinos cite.

(2203.17223.pdf)(CNB probably do not want to discuss this)

2.2.3 Neutrino Interactions and Detection

(<https://indico.mitp.uni-mainz.de/event/277/attachments/2666/3013/Scholberg1.pdf>)

The low interaction cross-section() [] of neutrinos which allows them to travel for large distances also make them almost impossible to detect. They can pass through vast amounts of material without leaving a significant trace. While at low energies processes such as Inverse Beta Decay are used to detect the neutrinos, at high energies neutrinos can interact via Charged Current(CC) and Neutral Current Interactions. In CC interaction, a neutrino interacts with a target nucleus with an exchange of W boson, transforming into a charged lepton corresponding to the flavor of the incoming neutrino and a hadron. The NC interaction is flavor blind and occurs with an exchange of the Z^0 boson and a nuclear recoil. Both reactions are shown in the equations below:

$$\nu_l(\bar{\nu}_l) + N \rightarrow l^-(l^+) + X \quad (2.8)$$

The products from the CC and NC interaction i.e a lepton and a hadron can be detected in multiple ways. Antineutrinos can also interact with atomic electrons leading to a W^- boson production called the Glashow resonance. The threshold antineutrino energy for such

a reaction to occur is 6.3 PeV. This process dominates the CC and NC interaction albeit only in a small energy range. Proposed in 1959, it was first observed at the IceCube Observatory []. Both CC and NC when interacting with the Nucleon undergo Neutrino-Nucleon Deep Inelastic scattering(DIS) where the interacting neutrino scatters off individual quarks inside nucleons (protons or neutrons), leading to the fragmentation of the nucleon and the creation of hadrons(Particles made of quarks). At low center-of-mass energies(TeV) accelerators can provide most of the information about the neutrino interaction with matter and the corresponding cross-section but at energies this estimation can either only be calculated via the detection of astrophysical and cosmogenic neutrinos or via a robust theoretical estimation based on quantum chromodynamics(QCD). The description of QCD at such high energies is still not completely understood, Moreover physics beyond the Standard Model can also be introduced for these energies which can further affect the neutrino cross-section estimation []. For the purpose of this thesis the neutrino cross-sections calculated in [] are used. [] provides an updated $\nu - N$ cross-section calculations with corresponding uncertainties, taking into account the full HERA [] data release and combining it with the DGLAP [] formalism of QCD. Based on the expected flux of the neutrinos, their cross-section and the energy of neutrino it is easy to calculate minimum detector sizes for high energy neutrinos. For example, for a neutrino of energy $E_\nu \sim 1PeV = 10^{15}eV$, the expected flux is $\frac{d^2N_\nu}{dtdA} \sim \frac{1}{cm^2 \times 10^5 yr}$, the cross-section is $\sigma_{\nu N} \sim 10^{-8} \sigma_{pp} \sim 10^{-33}$ and the targets can be estimated as $N_N \sim N_A \times V/cm^3$ where N_A is the Avogadro's number then the rate of expected events is given by:

$$N_\nu \sim N_N \times \sigma_{\nu N} \times \frac{d^2N_\nu}{dtdA} \sim \frac{1}{yr} \times \frac{V}{1km^3} \quad (2.9)$$

Therefore, to detect a neutrino at this energy range a detector with a minimum size of $1km^3$ is required. The type such large volume detectors for UHE ν depends on the particular techniques used to detect the products of neutrino interaction with nucleon.

The charged lepton can produce detectable signals via ionization, Cherenkov radiation or scintillation. Moreover, the lepton and hadrons can also trigger EAS which can also be detected. Both the lepton and the hadron can lead to a cascade. Depending on the flavor of the neutrino the interaction also leads to unique signals. The electron produced in the CC interaction of ν_e produces electromagnetic cascades in the propagation medium while a muon rarely produces a cascade like signature only undergoing radiation losses. In contrast, a tau lepton produced from ν_τ can propagate without interaction for a certain distance and then lead to a cascade. For NC reactions the leptonic cascade is missing and only a hadronic cascade can be observed. Low energy neutrinos or neutrinos produced in the atmosphere can also lead to similar cascades and act as background for high energy neutrino searches. Depending on the location and techniques employed such background is dealt in different ways. Some examples of different detectors based on the medium and the methodology employed for detection are as follows:

Ice and Water Cherenkov Detectors: IceCube Neutrino Observatory [] and its predecessor

AMANDA [] are examples of in ice Cherenkov detectors. The Observatory is located at the South Pole and uses a cubic-kilometer array of Antarctic ice to detect high-energy neutrinos. It consists of 80 strings carrying 60 photomultiplier detectors called DOMs situated between 1500m and 2500 m below the surface. Neutrinos interact with the optically clear ice nuclei, producing secondary particles that emit Cherenkov radiation. The detector's photomultiplier tubes capture the Cherenkov light, allowing reconstruction of the neutrino direction and energy. Muon tracks resulting from CC interactions can also be observed. Being underground partly shields IceCube from the atmospheric neutrino background, and it can also use the Earth as a shield to look for PeV upward-going neutrinos. The Observatory also consists of a surface array(IceTop) of ice Cherenkov tanks which further help in atmospheric background rejection and cosmic ray studies.

Water based Cherenkov detectors are used for neutrino detection since the first detection of neutrinos. Kamiokande II [] used a large underground water tank surrounded by PMTs to observe the first astrophysical neutrinos from SN 1987A []. Since the required detector volume for detection of a sufficient rate of neutrinos is very large, large stable natural water reservoirs are used to build such detectors. Some examples include the ANTARES [] and KM3Net [] located in the Mediterranean sea off the coast of France and the upcoming BAIKAL [] and P-ONE [] located in Lake Baikal, Russia and Pacific Ocean off the coast of British Columbia, Canada respectively. The actual detector and the principle remains the same as IceCube with the only change being the medium and upgrade of detectors depending on the advances in the field.

- **Radio Detectors:** These detectors are based on the detection of the Askaryan effect [] initiated by the neutrinos. The Askaryan effect is a phenomenon in which high-energy charged particles moving through a dense dielectric medium, produce coherent electromagnetic radiation in the radio frequency range. When the high-energy particles interact with the atoms and molecules in the dielectric medium, they generate a shower of secondary charged particles. As these secondary particles move through the medium they undergo a charge separation leading to the emission of coherent Cherenkov radiation in the radio frequency range. The effect typically produces radiation in the radio frequency range, from a few hundred megahertz (MHz) to several gigahertz (GHz). Experiments like ANITA [] have tried to detect the radio emission produced when neutrinos interact with the Antarctic ice []. RNO-G [], an in ice radio antenna array, is also under construction at Summit Station in Greenland to search for neutrinos above PeV energies. Detectors like AERA and GRAND could also use such a technique to detect EAS produced by neutrinos. The planned upgrade of IceCube, IceCube Gen-2 also plans to employ a large in ice radio array to increase its sensitivity to both astrophysical and cosmogenic neutrinos.
- **Acoustic and Radar Echo Detectors:** The cascade of secondary particles produced in a neutrino interaction in a medium can also generate an acoustic shockwave, also known

as a "thermoacoustic pulse," due to rapid heating and expansion of the medium. The resulting acoustic signal travels through the medium as a pressure wave and can be detected by sensitive acoustic sensors. Typically, large volumes of water or ice are used as the detection medium. The acoustic signal propagates through the medium and can be detected by underwater microphones (hydrophones) or other acoustic detectors. This techniques has not yet yielded a neutrino observation. It has been used at ANTARES as AMADEUS [] and at IceCube as SPATS [] to test the acoustic properties. ANDIAMO [] is a proposed acoustic neutrino detector which could use this technique in the future.

Radar Echo Telescope [] is a detector which aims to detect neutrinos using the radar echo method. The method is based on the reflection of a transmitted radar signal by the in ice neutrino cascade which acts as a short-lived mirror. The reflected signal is then detected at a receiving antenna. This technique is currently being tested in Greenland for Cosmic ray showers and might be employed to detect neutrinos in the future.

- **Air Shower Detectors:** Even though, the typical interaction lengths of UHE ν s are way larger than the atmospheric depth the neutrinos can still induce an EAS. Such EASs develop deep into the atmosphere in comparison to cosmic rays offering a distinguishing aspect for detection at cosmic ray observatories like the Pierre Auger Observatory. Pierre Auger Observatory tries to uses the said property to observe EeV neutrinos. EASs and the expected signature at the Pierre Auger Observatory for both cosmic rays and neutrinos is discussed in the next chapter ??.

2.2.4 Latest results

Astrophysical Neutrinos

spectrum After the measurements of astrophysical neutrinos at the IceCube Neutrino Observatory, the first plot and estimation of flux has been possible for high energy neutrinos. The flux spectrum as measured by IceCube is shown in fig ???. The flux was first published in 2013 [] and has since been refined with various analyses []. The plot shows the results of the summary of currently published analysis. The diffuse flux spectrum agrees across the various analyses within the overlapping energy regions. However there is a slight tension between the estimate of the spectral index which is obtained after fitting the flux spectrum. The measurements are also not enough to decide on the nature of the flux across the whole energy range and more measurements in the future would help understand the neutrino spectrum in more detail.

Sources Since neutrinos arrive at Earth pointing directly back to their source by plotting the candidate astrophysical neutrino events measured by the neutrino telescopes over a sky map can localise their sources of origin. Such studies have been performed by various neutrino telescopes such as ANTARES [], AMANDA [], BAIKAL [] and IceCube []. Only IceCube has found the most significant excess of 81 events in the TeV arriving from the

region within 0.18 degrees of active galaxy NGC1068(M77). The fig ?? taken from [] shows the hottest spot along with the excess. This observation has a significance of σ in comparison with ?. Hosting an active AGN surrounded by a dust torus makes it one of the ideal candidates for neutrino production []. The same analysis has also pointed out further neutrino source candidates PKS 1424+240 and TXS 0506+056. The latter of these is also important in the context of multi-messenger physics and is discussed later.

In 2023 IceCube has also published the first observation of diffuse emission of high-energy neutrinos from the galactic plane of our own galaxy, the Milky Way []. The result is at the 4.5σ level of significance, when compared to a background only hypothesis. However, the signal could also be due to a population of unresolved point sources near the galactic plane. This observation has opened a new way to observe our Milky Way galaxy and offers an evidence based proof confirming our understanding of both cosmic ray and neutrino physics. It also opens a new avenue for the application of multi-messenger astronomy. The fig ?? taken from [] shows the plane of the Milky Way galaxy as seen by different messengers.

Cosmogenic Neutrinos

Limits Both Pierre Auger Observatory and the IceCube neutrino Observatory have also performed searches to look for UHE ν which have a cosmogenic origin. These searches have led to some of the stringiest limit for such fluxes. These limits are shown in fig ???. The results from the Pierre Auger Observatory dominate for energies above 10^{18} eV and for lower energies IceCube provides the best limits. The lack of observations can help constrain various models for high energy neutrino production. These results can also help better our understanding of cosmic ray physics and in particular their composition. The lack of observation of the expected neutrino flux predicted by a pure proton composition scenario for cosmic rays is an important result in favour of mixed composition scenarios. This result further points towards the spectrum cutoff being more likely due to a maximum rigidity limit for the sources rather than a GZK limitation. The detection of cosmogenic neutrinos can help complete the picture of the neutrino and cosmic ray sky.

2.3 Multimessenger Astronomy

By combining the various messengers via which we can see the Universe can help understand the mechanisms behind their production and propagation better. By combining the observations of various dedicated experiments for gravitational waves(LIGO/VIRGO), Gamma rays(FERMI-LAT,CTA), neutrinos(IceCube) and cosmic rays(TA, Pierre Auger Observatory) a wholistic overview of an astrophysical process can be gathered. The detection from one messenger/experiment and a non-detection from another can also be informative since it helps refine our understanding or might even reveal a new phenomenon []. One of the most important aspect of this field is a fast communication network via which all the different experiments can share their observations as fast as possible. Supernova Early

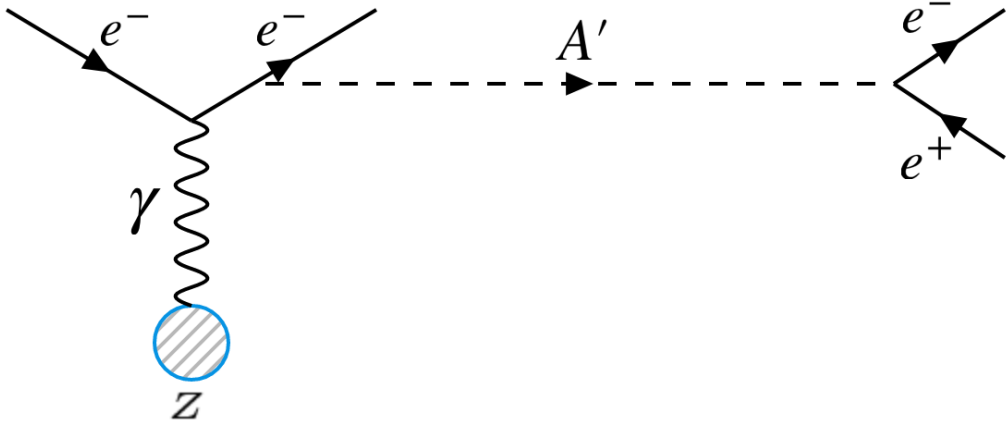


Figure 2.1: Visible mode

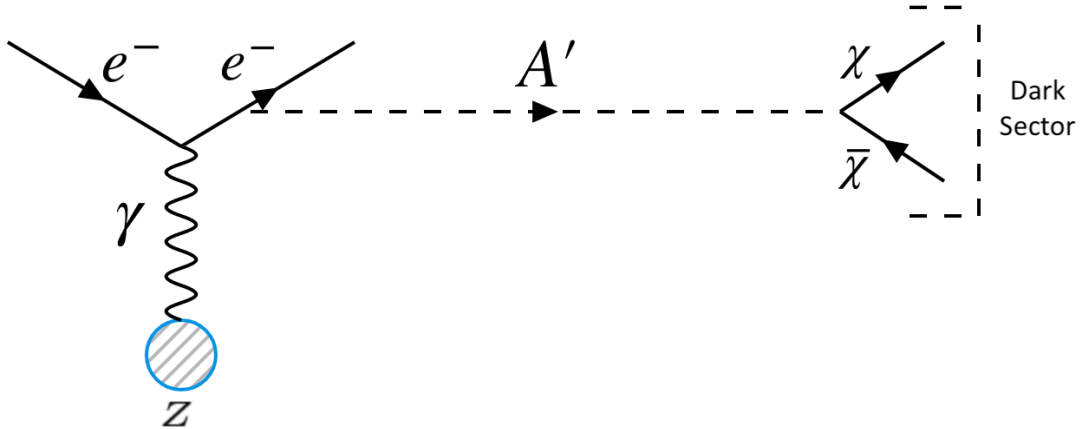


Figure 2.2: Invisible mode

Warning System (SNEWS) [], established in 1999 and The Astrophysical Multimessenger Observatory Network (AMON) [], created in 2013 are some examples of the networks used in multi-messenger astronomy. Some of the key observation of this field and the corresponding publications are summarised in table ???. As mentioned in the Introduction the Pierre Auger Observatory continues to contribute to these searches []. One of the best examples of this collaboration is [] where a spatial correlation search for neutrinos and CRs was performed as a joint effort between ANTARES, IceCube Observatory, Pierre Auger Observatory and the Telescope Array. The GW 170817 [] multi-messenger analysis using more than 70 observatories cemented the benefits and the potential of multimessenger astronomy.

The production and detection mechanisms discussed offer us the basic ingredients needed to set up an experiment for the detection of A' . One of the simpler layouts for such an

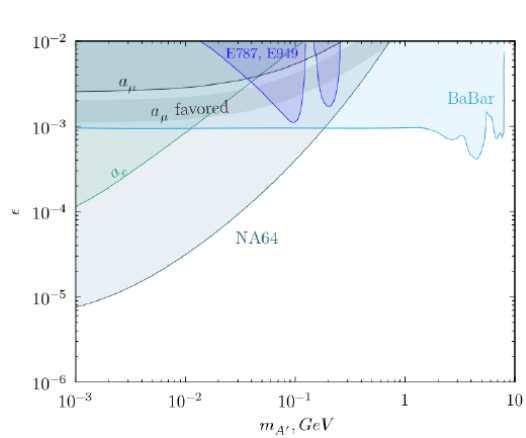


Figure 2.3: Current limits for invisible mode for 90% C.L. exclusion region in the $(m_{A'}, \epsilon)$ plane [5].

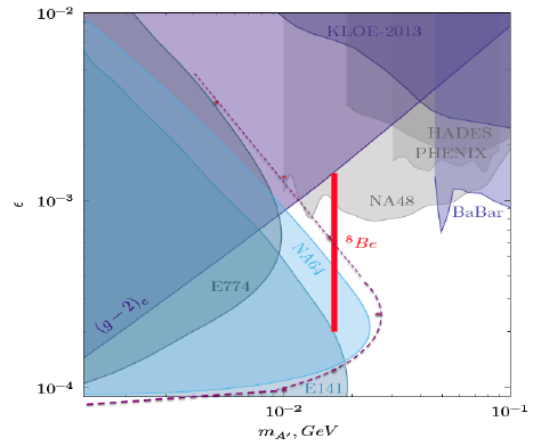


Figure 2.4: Current limits for invisible mode for 90% C.L. exclusion region in the $(m_{A'}, \epsilon)$ plane. The blue plane is with 2017 data and the dotted line is with 2017+2018 data for NA64. The red line is the region that might explain the X17 boson [5].

experiment is an electron beam dump experiment. NA64 falls in this category, the setup of which is discussed in the next chapter.

CHAPTER 3

Extensive Air Showers

As mentioned in the previous chapter An Extensive Air Shower (EAS) is a cascade of high-energy particles that are produced when an ultra-high-energy cosmic ray, typically a proton or a nucleus, collides with a particle in Earth's atmosphere. This cascade can span over hundred to thousands of meters based on the energy of the initial particle and the incoming angle. EASs offer the best way to look for UHECRs since the low flux of these particles make direct detection using detectors mounted on balloons and spacecrafts not feasible. The EAS can be detected at the ground via an array of detectors. To infer the properties of the CR from the EAS it creates, one needs to model and understand how an air shower develops in the atmosphere. This chapter describes the process of the initiation and the development of the shower induced by CRs and neutrinos. It also aims to describe the important characteristics of EASs which help in extracting the relevant information and the last section is devoted to the detection of the EASs using different detector systems.

3.1 Development

As the CR particle which is predominantly a proton collides with the nuclei of the atmosphere(N_2 , O_2 etc.) it produces pions and a few kaons. The neutral pions produced immediately decay to pairs of photons which in turn produce electrons via the process of pair-production. These electrons can then further produce photons via bremsstrahlung initiating a chain reaction which alternates between these two processes and forms the *electromagnetic component* of the shower. The charged pions can survive for a while but eventually decay to muon and a corresponding anti neutrino. These muons can either survive till the shower reaches the ground and form the *muonic component* or can also decay to electron thus contributing to the electromagnetic part. The neutrinos due to their low interaction cross-section mostly survive till they reach the ground and even further. Though not causing any problem for an EAS detector such neutrinos are the biggest background for a neutrino telescope. Kaons and charged pions due to their long lifetimes can also interact with the atmospheric nuclei producing additional pions which form the *hadronic component* of the shower. The hadronic component can

further contribute to both the electromagnetic and muonic component as more the shower propagates lesser the overall hadronic component becomes. A schematic of all the reactions with the different components is presented in fig ??.

The model the cascade of particles a detailed modelling of each component is required. These models help extract the basic properties of the cascade. A simplified model describing the electromagnetic component called the Heitler's toy model [] its hadronic extension and a general cascade equation are all discussed below. The specific development of a neutrino induced EAS is also discussed.

Heitler's Toy Model

Proposed by Heitler in 199 [], Heitler's Toy Model is a simplified perfect binary tree to understand and model an EAS development. The model characterises an EAS as a perfect binary tree. In such a scenario all particles produced in a shower equally share the primary energy available at the time of their creation. At each step which has a fixed size related to radiation length of the medium λ , the number of particles is supposed to be doubled with each having the same energy. The energy losses which may occur due to collisions are completely ignored. The shower development or splitting process is supposed to continue till a critical point where the energy required to create more particles becomes the same as energy lost by particles in the medium. At the critical point the shower has the maximum number of particles given by $N_{max} = E_0/E_c$ which is the ratio of the original energy to the critical energy. After this point the shower keeps getting absorbed in the atmosphere. The radiation length at this point is called the shower maximum denoted by X_{max} . This can be calculated to be $X_{max} = X_0 + \lambda_r \ln(E_0/E_c)$ where X_0 is the first interaction point in the atmosphere. A visualisation of the shower development according to the Heitler's model is shown in fig ??.

Such a simplified model works quite well for estimating the properties of the electromagnetic cascades although the N_{max} estimations do not match perfectly. The reason for this is the difference in the energy loss values for electrons and photons. For hadronic cascades an extension to the model was made. Other important properties of the shower such as lateral and longitudinal spread also requires to take into account the emittance direction and losses due to collision which are not taken into account for a simplified model. These are discussed in sec ?? . Even with its shortcomings the Heitler models gives a very good estimation for electromagnetic cascades and helps clearly categorise an air shower into three phases, the growth phase, the critical point phase and the tail phase.

Hadronic Extension

The Heitler model was extended by Matthews [] to characterise the hadronic cascades in an EAS. In his approximation when a hadron with Energy E interacts with a nucleon the total particles produced have a two-third charged component(charged pions) and a one-third neutral component with the initial energy equally divided based on the number fraction. The neutral component decays quickly and contributes its share of energy to the electromagnetic

component. The charged hadrons, provided they have not reached their critical energy in air(20 GeV), interact again repeating the initial process. Muons are only produced when the charged hadrons acquire an energy below the critical energy. The energy transfer for each component after n generations is given as $E_{had} = \left(\frac{2}{3}\right)^n E_0$ and $E_{em} = [1 - \left(\frac{2}{3}\right)^n]E_0$. Deeply penetrating air showers i.e a primary having a high energy and a low enough cross-section in air results in a lower number of muons produced and observed at ground and a primary having a high cross-sections vice versa. This fact is important as based on the number of muons to electrons observed at ground can help estimate the type of primary. The number of muons can be estimated in this model directly from charged hadrons when their energy reaches below the critical energy. For n generations $N_\mu = n_{ch}^n$ where n_{ch} are the number of charged hadrons and n can be written as $n = \frac{\ln(E_0/E_c)}{\ln(n_{tot})}$. Generalising by eliminating generations:

$$N_\mu = \left(\frac{E_0}{E_c}\right)^\alpha, \alpha = \frac{\ln n_{ch}}{\ln n_{tot}} \quad (3.1)$$

All the parameters in this model need to be estimated using detailed simulations []. α has been estimated to be in the range 0.82...0.9. Other factors such as production of particles which do not decay such as baryon-anti-baryon pairs [] can also affect the calculated values in this model. Other than the shower maximum and number of muons, the change of the depth of the shower maximum per decade in energy [] also called the elongation rate is given by $D_{10} = \frac{\langle x_{max} \rangle}{d\log_{10}E_0} = 2.3\lambda_r$. The elongation rate of electromagnetic showers in air is about $\approx 85g/cm^2$. The elongation rate theorem [] states that the elongation rate for hadronic showers is also D_{10}^{em} in the presence of Feynman scaling.

Another popular model to explain the development of air showers in particular the interaction with the nucleon is the superposition model []. In this model a nucleus with mass A is assumed to be a superposition of A independent nucleons each with energy $E_h = E_0/A$. With such an assumption one can reach the following conclusions:

$N_{em,max}^A(E_0) = AN_{em,max}^h(E_h/E_c) \approx N_{em,max}(E_0)$ i.e the fraction of energy transferred to the EM component at shower maximum has only an indirect dependence on mass via the dependence on primary energy.

$X_{max}^A(E_0) = X_{max}(E_0/A)$. This shows how the shower maximum has an inverse dependence on the mass of the primary i.e a shower initiated by heavier nuclei will develop higher in the atmosphere compared to one initiated by lighter nuclei.

$N_\mu^A(E_0) = A\left(\frac{E_0/A}{E_c}\right)^\alpha = A^{1-\alpha}\left(\frac{E_0}{E_c}\right)^\alpha$. This shows that heavier primaries will produce a larger number of muons compared to lighter primaries. For e.g. Iron showers contain 40% more muons than proton showers [].

$D_{10} = D_{10}^{had}\left(1 - \frac{d\langle \ln A \rangle}{d\log E}\right)$ Since Feynman scaling is known to be violated for higher energies thus the hadronic elongation rate is always less than the electromagnetic rate. Thus,

an increase in elongation rate towards 85 g/cm^2 is a direct indication of change of the mass composition.

Simulations have shown that the superposition model gives a more realistic description of many features of the shower []. However, it is still not a perfect description especially for heavier nuclei. Studies with photographic emulsion techniques have tried to create a better picture of the fragmentation of heavier nuclei []. This field is continuously evolving with better models and theoretical predictions being worked on based on our continually increasing database of observations.

Although these models help to understand the principle a full Monte Carlo simulation and a generalised analytical solution of the cascade equations is needed to fully recreate the EAS. Even after such an effort a few discrepancies such as the muon puzzle which is the mismatch in the number of muons predicted by the simulations in comparison to the measurements [].

LPM effect

Another process that can directly impact the development of high energy electromagnetic showers since it is the reduction of the bremmstrahlung and the pair-production cross-section is the Landau–Pomeranchuk–Migdal effect []. All the above models work under the assumption that the energy range is low enough for the LPM effect to not be applicable. If the medium is dense enough or at high energies the LPM effect also becomes important to fully estimate the development of an air shower. The implications of the LPM effect for air showers implemented in simulations can be found in [].

alexander
citation

Neutrino induced EAS

The development of a neutrino induced shower in comparison to a cosmic ray shower is important in the context of this study. Understanding the differences helps to identify the unique signature at a cosmic ray observatory like the Pierre Auger. The differences in the shower development can also help increase the sensitivity of a neutrino observatory like the IceCube. Unlike a cosmic ray particle a neutrino can interact at any depth. This is due to the low neutrino cross-section at $10^{18} \approx \dots$ in comparison, for e.g. the proton-nucleon cross-section which is $\approx \dots$. Thus, neutrino-induced showers require significantly higher neutrino energies to produce interactions with observable effects. The main channel via which an ultra-high energy neutrino can interact is either a CC or NC interaction. Neutrino-induced showers involve fewer particles in the initial interaction and often have a lower multiplicity of secondary particles compared to cosmic ray-induced showers. The development of the shower and the unique signature depend on the flavor of the neutrino as shown in fig ??.

An electron neutrino interacting via CC interaction produces an initial hadronic cascade which has fewer particles in comparison to a hadron-initiated shower from the CRs. The high energy electron/positron produced in the same initial interaction also produces an electromagnetic shower. At high energies the two showers are overlapped and depending on

the fraction of energy carried by the electron/positron governs the ratio of the electromagnetic to hadronic component for the shower.

A muon neutrino also produces an initial hadron cascade but in contrast to the electron neutrino interaction the resulting muon has a very low probability to decay and mostly passes through the detector undetected. The energy carried by the muon which is usually a large fraction is lost and only the hadronic cascade can be detected.

Tau neutrinos have a unique and particularly interesting signature even among neutrino showers. The initial interaction remains the same with the production of a hadronic cascade, but the resulting tau lepton has a decay length $\approx 10\text{km}$. This means that depending on the depth of the atmosphere the tau encounters on its way to the ground it can either decay and produce an electromagnetic cascade much later than the initial hadronic cascade or not decay at all. The asynchronous cascade signature is also known as "double-bang" effect and can occur both in air or a specific medium. Tau neutrinos can also be a source of upward-going air showers which can also be detected at an EAS detector. In this case the tau neutrinos can interact in the Earth's crust or in some natural obstruction like mountains around the detector leading to production of a hadronic cascade which gets absorbed and a tau lepton which can escape and produce an electromagnetic cascade in air that can be detected. The process is unique to tau neutrinos for an EAS detector since for the electron neutrino both the hadronic cascade and the electron is absorbed by the obstacle whereas for the muon neutrino the resulting muon is almost impossible to detect.

All three neutrino flavors can also undergo NC interactions. These also result in an initial hadronic cascade and a neutrino which usually does not interact and escapes being detected especially for an EAS detector. Thus, the signature is indistinguishable in comparison to a muon neutrino CC interaction. The probability of NC interaction is also lower than a CC interaction which also affects the overall number of EAS induced due to this channel.

3.2 Characteristics

Apart from the shower maximum and the number of muons at ground other observables are also required to fully characterise the shower and estimate the important quantities such as the mass, energy and the arrival direction of the incoming primary CR or UHE ν . Fig ?? gives an overall picture of the evolution of an EAS in air. The amount of atmosphere penetrated is measured in units of slant depth X , with a unit of g/cm^2 . The first interaction depth X_0 which is the slant depth until the first interaction of the primary particle with the nucleon. The shower begins from this point on and the vector along which the shower develops from the first interaction point is called the *shower axis*. The development continues till the shower reaches a maximum which was defined earlier and is denoted by X_{max} . After this point the shower depopulates caused by particle energy loss due to absorption or decay. The *longitudinal development profile* plotted in fig ?? gives a relation between the number of shower particle in dependence to the atmospheric depth. This relation is also called the Gaisser-Hillas function [] parametrised as follows.

$$N(X) = N_{max} \left(\frac{X - X_0}{X_{max} - X_0} \right)^{\frac{X_{max} - X_0}{\lambda}} \exp \left(\frac{X_{max} - X_0}{\lambda} \right) \quad (3.2)$$

X_0 and λ can be estimated by fitting the profile based on the above function and depend on the composition and energy of the primary. N_{max} is the number of particles observed at X_{max} . The integral of the longitudinal development profile gives an estimate of the total calorimetric energy deposited by the shower. The point where the shower axis vector intersects the ground is called the *shower core*. Shower axis is thus defined by the zenith θ , azimuth ϕ and the shower core position. If one looks at the shower head on the large thin disc like appearance consisting of highly energetic particles is called the *shower front*. The shape is due to the path length differences between the shower particles travelling away from the shower axis to the one travelling in the direction of the shower axis. The disc is thus thinner near the shower core and widens away from it. As the shower front intersects the ground the density and the timing of the particles detected at the detector form what is called the *shower footprint*. It is the primary observable used by a ground level EAS detector to measure and characterise the shower. The arrival time of the particles in the footprint can help determine the shower geometry whereas the density can be used to reconstruct the energy of the primary. The density is estimated as a function of the radial distance from the shower core on the ground by the *lateral distribution function*(LDF). The modern LDF function is an extension on the parameterisation given by Greisen [] and by Kamata and Nishimura [] and is given as:

$$\rho_e(r) = \frac{N_e}{2\pi R_M^2} C(s) \left(\frac{r}{R_M} \right)^{(s-2)} \left(\frac{r}{R_M} + 1 \right)^{(s-4.5)} \quad (3.3)$$

Define other variables

with $s = \frac{3}{1+2X_{max}/X}$ and the Moliere radius $R_M = 0.0265X_0(Z + 1.2)$.

Another important characteristic of an EAS are its universality features [] first pointed out by Hillas for electromagnetic showers []. In this formulation around the shower maximum the average development of an air shower is universal. An individual shower can be defined as a function of shower age s give by:

$$s = \frac{3}{1 + 2X_{max}/X} \quad (3.4)$$

Simulations have used such a universal feature to fit shower profiles reasonably well independent of the primary mass and energy []. This feature is a result of the nature of the development of the cascade process which hides the initial primary dependent fluctuations []. Air shower universality only holds for air showers induced by gamma rays, electrons, or positrons and breaks down for a hadronic cascade. It can still be used if each individual component of the shower can be disentangled. Although, not applicable for this study Universality is an important characteristic of the shower and has been used to estimate the proton-air cross-section |cite and other CR studies [].

3.3 Detection

At high energies due to the low flux EAS offer the best way to detect CRs. Low cost ground based detectors can be spread over large areas offering a cost effective way to study UHECRs. The shower can be seen through different emissions such as the Cherenkov, fluorescence and radio. The particles arriving at ground can also be directly detected. The different emissions which can be detected in context of EAS are described in this section along with an expected EAS signatures of a neutrino induced EAS which relates to the analysis presented in this thesis.

Fluorescence Detection

The phenomenon of fluorescence emitted by air showers above 10^{17} eV, known as "atmospheric fluorescence," involves the production of faint optical and ultraviolet (UV) light by the interaction of high-energy particles from extensive air showers with the nitrogen molecules in Earth's atmosphere. The energy levels of the nitrogen molecules determine the wavelengths of light that are emitted. The UV light emitted during the de-excitation process is typically in the near-ultraviolet range. The number of photons emitted directly correlates to the energy deposited by the shower particles. At altitudes between 5 and 10 km the yield has a height dependent rate of 4-5 photons per meter per charged particle. The photons can be seen at large distances up to 35km. The measurement of the light intensity through fluorescence telescopes with the help of the geometry of the shower axis offers a way to reconstruct the longitudinal profile of the shower and a subsequent energy estimation of the primary. Fluorescence telescopes are limited in their operational duty cycle which is about 10-15 % since they can only be operated on clear moonless nights. A proper reconstruction of shower variables via the emitted fluorescence light also requires a constant monitoring of the atmosphere to account for light yield corrections. The pioneering fluorescence light detection of EAS include experiments at Volcano Ranch [] and Fly Eye experiment []. Currently, this technique is also used at the the Pierre Auger Observatory and the Telescope Array.

Cherenkov Detection

Charged particles moving through the atmosphere can also produce Cherenkov light []. The EAS can be either detected via Imaging Cherenkov telescopes(IACTs) which can detect showers between 20GeV -100 TeV and are used for gamma ray astronomy. For CRs non-imaging Cherenkov detectors can be set up akin to a ground based particle detector array. Since the cherenkov cone is collimated around the shower axis the detectors need to be located with small spacing between them. For eg. For a particle at 10km height The Cherenkov cone has a radius of 120m. This property and the similar operational limitations like the fluorescence detection make this a not viable technique to detect UHECRs. For UHECRs due to the low flux the a ground based Cherenkov detector array will require a very large number of detectors and will still only have a duty cycle of 10-15%. The currently

operational experiments using the non-imaging Cherenkov technique for EAS detection include Yakutsk [] and Tunka [] etc. IACTs are very popular for gamma-ray astronomy and multimessenger detections with H.E.S.S. [], MAGIC [] and CTA [] currently operational.

Radio Detection

Particle detector arrays

CHAPTER 4

Pierre Auger Observatory

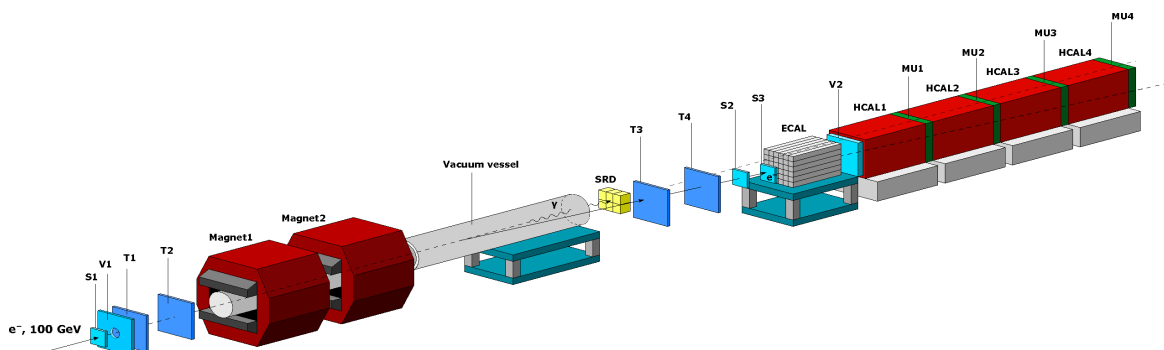


Figure 4.1: Invisible mode setup [6]

NA64 is a beam dump fixed-target experiment located at the H4 beam line of the Super Proton Synchrotron (SPS) at CERN. The objective of the detector is to look for rare dark matter candidates, primarily Dark Photons A' . A' is supposed to be emitted via a process similar to bremsstrahlung $e^-Z \rightarrow e^-ZA'$. The experiment is not a permanent fixture and has been in operation since March, 2016. Since its approval the setup has taken data a total of four times which included a two week test run in 2016 and four weeks of data taking each in 2016, 2017 and 2018. Each year the setup has slightly varied to account for different beam energies and expected background.

The SPS provides a primary proton beam of 400 GeV/c with $\simeq 10^{12}$ protons per spill which is then converted to electrons by incidence on a beryllium target. The e^- beam is in the momentum range 50 – 150 GeV/c with a maximal intensity $\simeq 10^7$ per SPS spill of 4.8s. The provided high-energy e^- beam with the large luminosity was needed since the A' couples very weakly to the SM. The beam is then characterized by passing it through scintillators (S1-S3), veto (V_1), two dipole magnets with an integral magnetic field of $\simeq 7 \text{ Tm}$ and trackers (MM-section(5.1.1), GEM-section(5.1.2) contained in tracking stations (T1-T4) which measure the e^- beam momenta to a 1% precision [7]. Additionally the combination of

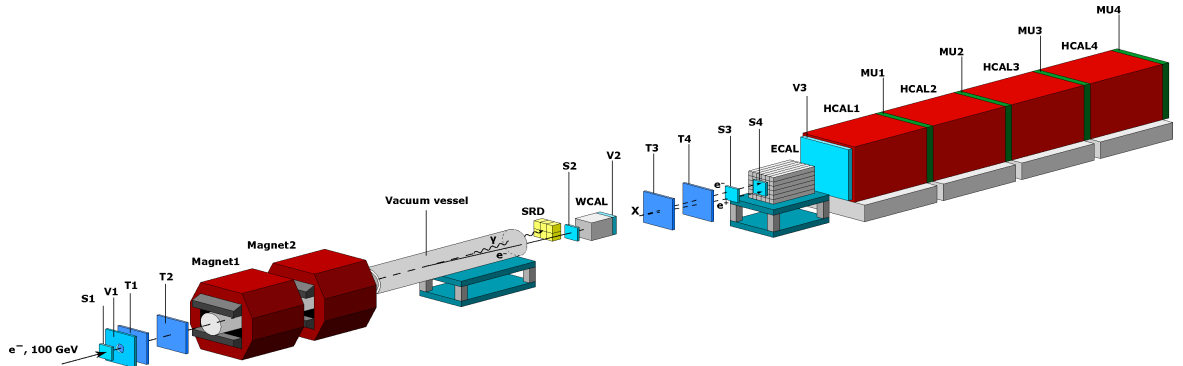


Figure 4.2: Visible mode setup 2017 [10]

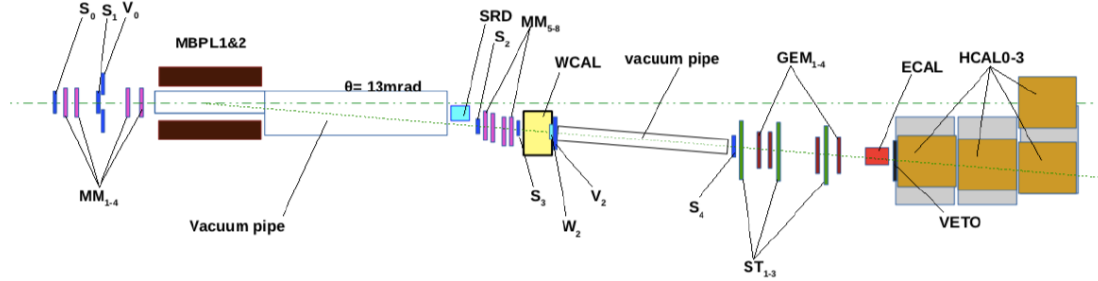


Figure 4.3: Visible mode setup 2018-top view [11]

magnets followed by a 15m long vacuum vessel and a PbSc synchrotron radiation detector (SRD) acted as a filter to reject low energy electrons and hadrons that might be present in the beam and would contribute to the overall background. They were separated by putting a cut on the amount of synchrotron radiation energy deposited by the respective particle [8]. The beam is then allowed to hit the electromagnetic calorimeter (ECAL) which acts as an active target. The ECAL consisted of 6x6 Shashlik-type modules each with 40 radiation lengths (X_0) of which the initial $4X_0$ is employed as a separate preshower(PS) detector. The ECAL had a resolution of $\delta E_{ECAL}/E_{ECAL} \approx 0.1 \sqrt{E_{ECAL}} [\text{GeV}]$ [6]. The combined information achieved by studying the shower and the SRD signal helped in suppressing the hadron contamination in the beam to a remaining fraction of $\lesssim 10^{-6}$ [9]. A combination of Veto(V_2) and hadronic calorimeter(HCAL) is situated downstream of the ECAL. They serve as a veto against muons, neutrals like high energy photons or hadrons produced in the target ECAL. The HCAL consisted of four modules (HCAL₁₋₄) separated by muon counters (MU_{1-4}) and were slightly shifted along the beam with each module consisting of 3x3 cells adding up to a total of ≈ 30 nuclear interaction length (λ_{int}). The HCAL had a resolution of $\delta E_{HCAL}/E_{HCAL} \approx 0.6 \sqrt{E_{HCAL}} [\text{GeV}]$ [6].

The above setup works well for the *invisible mode* ($10^{-4} \lesssim \epsilon \lesssim 10^{-3}$, $m_{A'} \lesssim 1\text{GeV}$) but requires modification for the search of $A'(X)$ in the *visible mode* ($10^{-4} \lesssim \epsilon \lesssim 10^{-3}$,

$m_{A'} \lesssim 100\text{MeV}$). To search for the visible decays a short tungsten calorimeter (WCAL) and a veto (V_2) were added right after the vacuum pipe and before the second set of tracking detectors (fig.(4.2)). The size of the WCAL was selected so that the leakage of particles is small and the sensitivity to short lifetimes is maximized. The distance between the WCAL and the ECAL for the visible mode searches was slightly varied(2.5m->5.6m) between 2017 and 2018 which allowed for the installation of a 3.1m long vacuum tube to create better spacing between the ECAL and WCAL for a better angular resolution to increase the sensitivity to X17 bosons [10]. A WCAL catcher was also installed in 2018 to prevent any leakage. Additionally the beam momentum was increased from 100GeV to 150 GeV in 2018 and one of the tracking station consisting of two MicroMegas (MM) was also shifted upstream of the WCAL. Counter (W_2) and straw detectors (ST_{1-3}) were also tested during the 2018 beam period(fig.(4.3)). Both *invisible* and *visible* mode setups were also used to look for rare SM events that involve a photon decaying to a dimuon pair via bremsstrahlung $e^-Z \rightarrow e^-Z\gamma; \gamma \rightarrow \mu^+\mu^-$. Comparing these rare events, which were obtained from real data, to our Monte Carlo(MC) simulated sample helped in estimating the validity and efficiency of our MC simulation [11].

In summary, NA64 tries to estimate and tag the beam e^-s using a combination of trackers, SRD and ECAL/WCAL, uses the said ECAL/WCAL as an active target and then collects the residue of the interaction in the downstream HCAL/ECAL+HCAL. It also utilizes the hard bremsstrahlung photon to dimuon conversion as a measuring stick for the reliability of the MC simulations. The reactions of interest were attempted to be observed with a combination of hardware and software triggers depending on the expected signature of the decay mode for A' .

Invisible Mode: $A' \rightarrow \chi\bar{\chi}$ signature:

$$\begin{aligned} & Beam(p \simeq 100 \text{ GeV}), \\ & E_{ECAL+PS}(< 100 \text{ GeV}), \\ & V_2(< E_V^{th} \simeq 1 \text{ MIP}), \\ & E_{HCAL}(< E_{HCAL}^{th} \simeq 1 \text{ GeV}). \end{aligned}$$

Visible Mode: $A' \rightarrow e^+e^-$ signature:

$$\begin{aligned} & Beam(p \simeq 150 \text{ GeV}), \\ & E_{WCAL}(< 150 \text{ GeV}), \\ & E_{WCAL+ECAL+PS}(\simeq 150 \text{ GeV}), \\ & V_2(> E_V^{th} \simeq 1 \text{ MIP}), \\ & V_3(< E_V^{th}), \\ & E_{HCAL}(< E_{HCAL}^{th} \simeq 1 \text{ GeV}). \end{aligned}$$

CHAPTER 5

Neutrino Analysis $60^\circ < \theta < 75^\circ$

This chapter gives a brief summary of the hardware and the software used to implement tracking for NA64. It begins with a description of the detectors used to track the incoming beam at NA64. Further it describes the algorithm implemented to fit tracks to the information received from the detectors. It ends with a brief description of the software where the said algorithm is implemented.

5.1 Detectors

NA64 uses two varieties of Micro-Pattern Gas Detectors (MPGD) to track the beam particles and estimate their momentum. MPGDs offer a high rate capability along with a spatial resolution $O(\mu\text{m})$, both of which are required for NA64. They work on the basic principle that charged particles moving through a medium interact with it in different ways losing some energy in the process. The interaction in case of MPGDs is a direct Coulomb interaction with the atoms present in the detector medium leading to their ionization. The two varieties are the following:

5.1.1 MicroMegas

MICRO-MEsh GAseous Structure (Micromegas) were invented in 1992 by Georges Charpak and Ioannis Giomataris [12] as an alternative to Multi-Wire Proportional Chamber (MWPC) [13] to counter its space resolution and rate limitations.

In a MicroMegas (MM) detector a metallic mesh is introduced between the anode and cathode. The mesh itself is supplied with a high voltage effectively separating the detector volume into two regions. When a charge particle traverses the detector region above the mesh it will ionize the atoms present in the medium. The electrons produced in this process drift towards the mesh where they encounter a high electric field reaching enough energy to create an avalanche. The electrons from the avalanche induce a signal on the readout electrodes

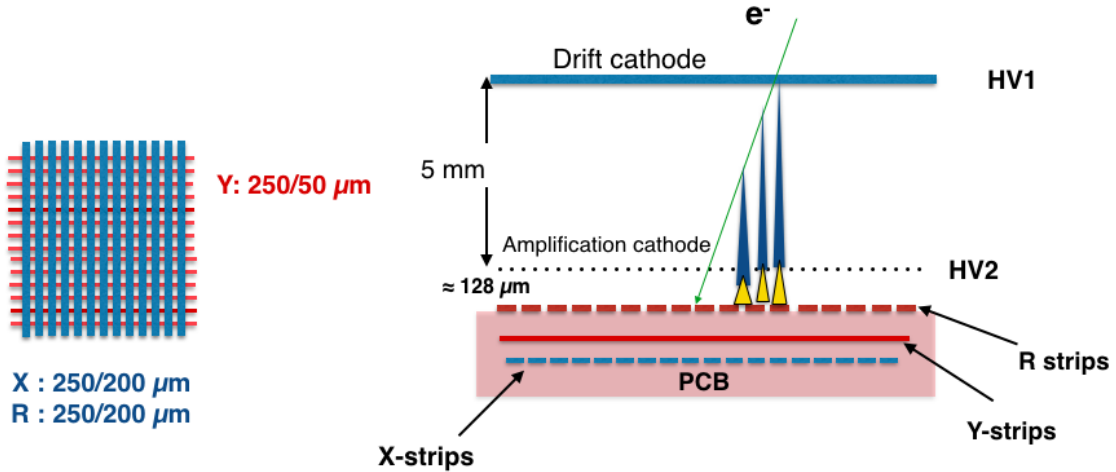


Figure 5.1: Left: Strip dimensions of the modules, Right:NA64 Micromega's working principle [14]

while the ions are collected by the mesh. A schematic of the detector is shown in fig.(5.1) and a more detailed description of the process can be found in [12].

The NA64 Micromegas are resistive Micromegas where the usual single readout layer is replaced with a layer of resistive strips (R) followed by additional readout layers below. They were developed at the CERN EP-DT-EF workshop [14]. The readout is made up of two layers of 320 strips(X and Y) perpendicular to each other, both rotated by an angle of 45° with respect to the global reference system and are therefore called U and V throughout the thesis. The strips which are parallel to the resistive strips have a lower capacitive coupling compared to the ones which are perpendicular leading to a slightly worse positional resolution in one plane. The detector was measured to have a gain of $\approx 2 \times 10^4$ at an amplification voltage of 540 V [14].

5.1.2 Gas Electron Multiplier

Gas Electron Multiplier (GEM) was invented by F.Sauli at CERN in 1997. They are cheaper and easier to manufacture compared to other tracking detectors and offer a flexible geometry thus can be used in different shapes and sizes. They have versatile applications as they can be used both as a standalone detector and as readout elements of a Time Projection Chamber (TPC).

A standard GEM detector consists of a single or multiple layers of GEM foils inserted between drift and charge collection electrodes. Each foil is made up of polymer coated with a thin metal layer on both sides. The foil is punched with a high density of holes. The holes are etched on both sides of the foil forming a double-conical structure as shown in fig.(5.2), other kind of hole shapes are also possible. When a differential voltage is applied to the electrodes the holes develop field lines as shown. Electrons drifting through the holes will

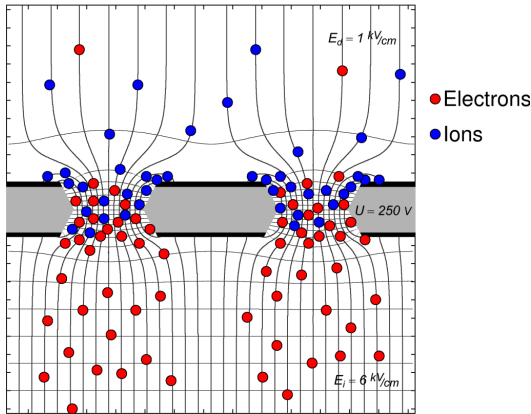


Figure 5.2: A sketch of GEM field lines [19].

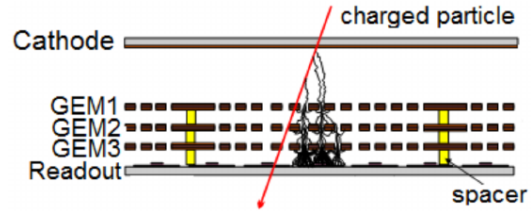


Figure 5.3: Schematic of a triple GEM detector along with the working principle [20]

follow the field lines gaining enough energy to ionize the filled gas leading to an avalanche. Electrons from the avalanche are then collected by the readout electrode. A more detailed description of the process can be found in [15].

The NA64 GEMs were developed at the Technical University Munich (TUM) [16] and resemble the ones developed for COMPASS [17]. They consist of three stacked GEM foils followed by a stripped readout. The readout consists of two layers perpendicular to each other (X and Y) which are aligned the same as the global reference system. The detector is filled with a mixture of Ar/CO₂ in a ratio of 70/30. The gain of the detector was measured to be $\approx 8 \times 10^4$ at detector voltage of 4050V [18].

5.2 Track-Reconstruction Algorithm

This section describes the methods used to fit a track to the output obtained from the tracking detectors and to extract momentum information of the beam from this data. For a simple setup this can be done by fitting a straight line through the hits on the detectors for the regions before and after the magnet obtaining the angle between the two lines to estimate the momentum. This method is described under Linear Regression. For a more complex tracking system and to simulate a more realistic picture for the beam and better alignment for the detectors, the Kalman filter algorithm is used to fit the tracks.

5.2.1 Linear Regression

Linear regression for track fitting involves fitting a straight line to the data points, hits in our case with the condition that the total error is minimized. The total uncertainty is calculated as a sum of squares of individual measurement errors. Since the final result is dependent on minimizing the sum of the squares this approach to linear regression is known as least-squares

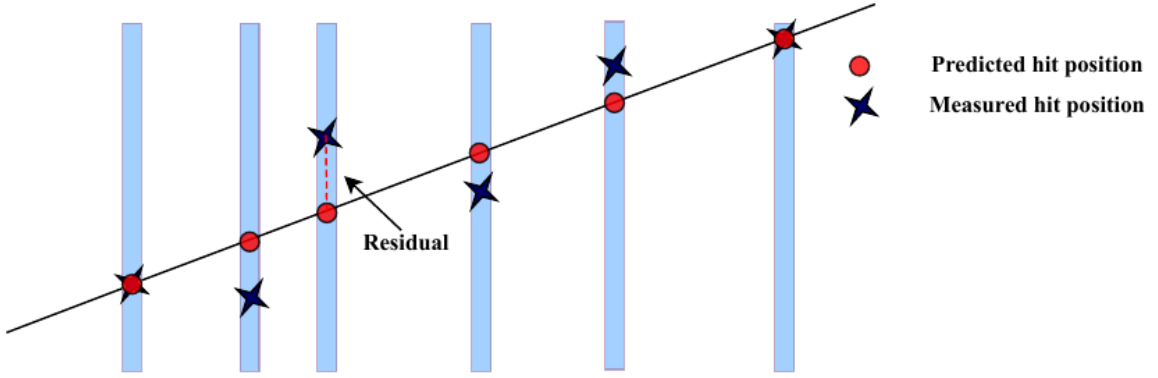


Figure 5.4: Linear regression pictorially.

approach. A simple mathematical description of the method is given below.

The equation of a straight line is given by $y = mx + c$, where m is the slope of the line and c is the intercept on the y axis in a Cartesian coordinate system. The final goal is to obtain a good estimate for the two parameters m and c . To obtain this estimate the square of error needs to be minimized. The error is the difference between the actual measurement (x_i, y_i) and the prediction from our model, the equation of straight line. This error is also known as the residual and is defined as $r_i = y_i - mx_i - c$ for an i^{th} measurement. Suppose that n hits are measured then to obtain an estimate for m and c we need to minimize $\sum_{i=1}^n r_i^2$. The minimized estimates have the following values:

$$\min(m) = \frac{\sum_{i=1}^n x_i y_i - 1/n \sum_{i=1}^n x_i \sum_{i=1}^n y_i - i}{\sum_{i=1}^n x_i^2 - 1/n (\sum_{i=1}^n x_i)^2} = \frac{\bar{xy} - \bar{x}\bar{y}}{\bar{x}^2 - \bar{x}^2} \quad (5.1)$$

$$\min(c) = \bar{y} - \min(m)\bar{x} \quad (5.2)$$

A more detailed mathematical description can be found in [21]. The quality of the fit can be evaluated by calculating the reduced chi-square $\chi^2_{red} = \frac{\chi^2}{ndf.} = \frac{1}{ndf.} \sum_i \frac{(r_i)^2}{\sigma^2}$ where σ is the resolution of each detector which might not be equal and $ndf.$ are the number of degrees of freedom available for the fit.

Linear regression can also be used for NA64 to fit for the bending due to the magnets by replacing the model function from the equation of the straight line to some polynomial function. Such a method is called polynomial regression [22].

5.2.2 Kalman Filter

Kalman filter is an estimation technique originally developed to predict rocket trajectories. In particle-physics it is often used as an iterative least-square estimation procedure for track fitting. Following is a brief description of the algorithm for track fitting which closely

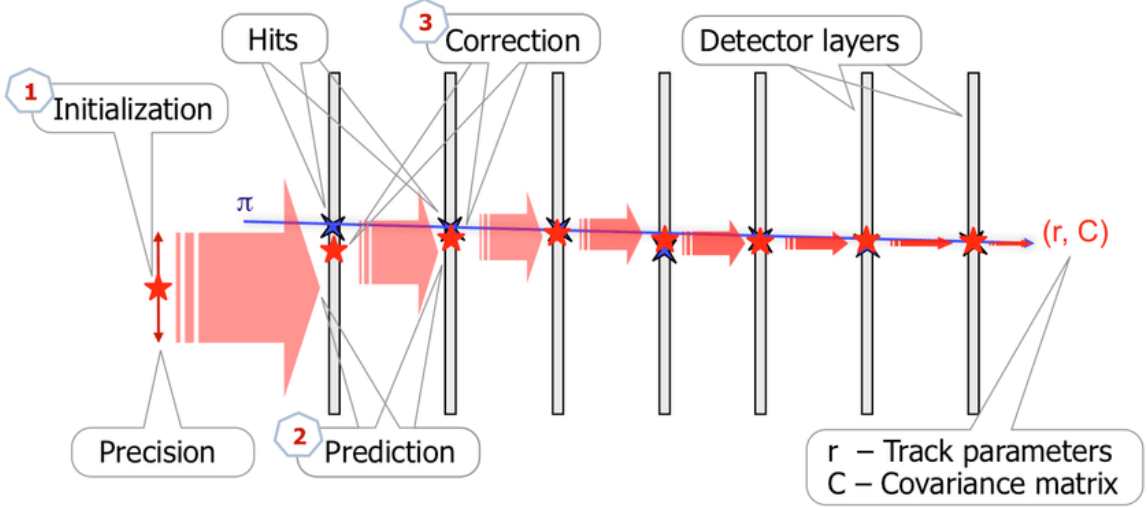


Figure 5.5: Pictorial representation of the working principle of a Kalman filter [25].

follows [23, 24].

Let's assume for a given track model x_k be the value of the "ideal measurement" at the intersection point between the track and the detector at some point k . This is also called the state vector of the system and in an iterative procedure where the value at location k is obtained from a previous location $k - 1$ can be written as :

$$x_k = f_k(x_{k-1}) + w_k \quad (5.3)$$

where f is the track model propagator function and in this form propagates from detector $k - 1$ to k and w_k is a random vector representing the noise between the two detector positions such as multiple scattering perhaps.

Now, the state vector is not a quantity that is measured directly by the detector. If we assume that m_k is the value of the measurement by detector k then it can be given as :

$$m_k = h_k(x_k) + \epsilon_k \quad (5.4)$$

$h_k(x_k)$ is the function of the state vector measured at the detector which in our case will be a position measurement by our tracking detector. ϵ_k represents a measurement noise which for an ideal measurement will be zero. We assume that both w_k and ϵ_k are independent random variables and have a mean value of zero. For a linearized system,

$$f_k(x_{k-1}) = F_k x_{k-1} \quad (5.5)$$

$$h_k(x_{k-1}) = H_k x_k \quad (5.6)$$

There are three key operations that need to be performed for the Kalman filter procedure.

These are ordered and described with respect to time specifically to handle multiple scattering in a proper manner.

- **Filtering** is estimating the "present" state vector taking into account all the present and "past" measurements. Filtering from m_1 to m_k includes filtering m_1 to m_{k-1} , then propagating from m_{k-1} to m_k and including m_k .
- **Prediction** is estimating the state vector at a "future" time.
- **Smoothing** is estimating the state vector at any point based on all the measurements.

The basic process can be described as follows. If we have an estimate at position x_{k-1} then it can be extrapolated to position x_k by using the system equation. The estimate at x_k is calculated as a weighted mean between the prediction from the system equation and the measurement from the measurement equation m_k . This estimate is passed to all the previous estimates in parallel by using the smoother which is running in a backward direction. Also if there is no process noise w_k then smoothing is equivalent to back extrapolation.

System equation:

$$x_k = F_k x_{k-1} + w_k \quad (5.7)$$

$$Ew_k = 0, \text{Cov}[w_k] = Q_k (1 \leq k \leq N) \quad (5.8)$$

Measurement Equation:

$$m_k = H_k x_k + \epsilon_k \quad (5.9)$$

$$E\epsilon_k = 0, \text{Cov}[\epsilon_k] = V_k = G_k^{-1} (1 \leq k \leq N) \quad (5.10)$$

As an example here are the different processes for one update step:

- Prediction - Extrapolation of the state vector

$$x_k^{k-1} = F_k x_{k-1} \quad (5.11)$$

Extrapolation of covariance matrix :

$$C_k^{k-1} = F_k C_{k-1} F_k^T + Q_k \quad (5.12)$$

- Filtering - Update of state vector

$$x_k = C_k [(C_k^{k-1})^{-1} x_k^{k-1} + H_k^T G_k m_k] \quad (5.13)$$

Update of covariance matrix :

$$C_k = [(C_k^{k-1})^{-1} + H_k^T G_k H_k]^{-1} \quad (5.14)$$

- Smoothing - Smoothed state vector

$$x_k^N = x_k + A_k (x_{k+1}^N - x_{k+1}^k) \quad (5.15)$$

where A_k is called the smoother gain matrix given by: $A_k = C_k F_{k+1}^T (C_{k+1}^k)^{-1}$

Other information such as residuals r_k , covariance matrix of residuals R_k and χ^2 for each step are also calculated and incorporated during the fitting process. A global χ^2_{trk} is a sum of all chi-squares from filtering. After the Kalman fitting we have three fits for the parameters at a particular hit at position k : a track fit for the part upstream i.e using measurements from 1 till k , a backward track fit for the part downstream using measurements from N till k and a fit for the whole track.

The Kalman filter can also be applied for a non-linear system such as in the presence of a magnetic field, by the replacement of the track propagator f_k with the first two terms of its Taylor series expansion. With this change the procedure is known as extended Kalman filter. This procedure is implemented in the track fitting libraries in CORAL. The computational time of the filter is directly proportional to the number of detector and does not depend much on the total amount of hits in an individual detector. A potential drawback of the algorithm is that it needs initial starting parameters for the state vector and its covariance matrix. This is usually solved by either fitting a small number of measurements with linear regression and then feeding it to the algorithm or by starting with an arbitrary value for the state vector and covariance matrix.

5.3 CORAL and PHAST

CORAL is the reconstruction and analysis software used at CCommon Muon and Proton Apparatus for Structure and Spectroscopy (COMPASS). PHysics Analysis Software Tool (PHAST) was developed later to separate the analysis from reconstruction and works on the output obtained from CORAL. CORAL was envisioned as a modular program that consists of standard libraries for different processes such as track reconstruction and alignment, that are controlled using external option files. Different detectors can be added externally in a detectors table (detectors.dat) which is fed to CORAL along with the measured data file. The libraries of the detectors that are used at the NA64 experiment such as the Micromegas, which are a little different compared to the standard COMPASS ones, were also added to CORAL [18].

The track reconstruction process in CORAL works in the following way. The detectors are divided into separate zones either depending on the magnets or depending on obstruction by a detector such as a calorimeter both of which is true especially in the visible mode for NA64. Zones before and after the magnets are fitted with straight line segments depending on the measurements. The line segments in each zone are then bridged together through the magnets which is sped up with an external Dico file. A Dico file consists of all the possible trajectories pre-calculated, for a particular geometry or setup. The last step in the track reconstruction process is a Kalman filter taking the initial information from the previous two steps and running over the entire track piece, combining the measurements into the final prediction. The momentum is determined according to the integrated magnetic field and the

bending angle observed for the fitted track. The option file for track reconstruction for NA64 controls the input and output files for the whole process and also contains information about various noise cuts implemented for the detectors which are described in detail in [18].

CHAPTER 6

Neutrino Analysis DGH

Measuring charged particles precisely and efficiently is a crucial part of any particle physics experiment. This need is intensified more for NA64 since we need a very accurate estimate for the beam momentum and energy to look for missing energy events for the *invisible mode*. NA64 also requires an accurate track reconstruction for the *visible mode* to look for e^+e^- tracks that might originate from a possible A' . While the experiment was being installed a big emphasis was given to measure the outer boundaries of the detectors using lasers. Nonetheless this precision is insufficient when extrapolated to get an estimate for the inner part of the detector. Since the detectors are expected to have a micrometer precision, track based alignment will provide a better estimate for the actual detector positions and will help improving the errors in the final physics analysis. This chapter describes the program **Millepede** implemented for the track based alignment for NA64 and also reports the different types of alignment performed for the current setup. The results of alignment program are also compared to the standalone alignment method described in [26].

6.1 Previously used method

The previously used method [26] which was used for alignment in NA64 is a simple residual fit and shift. A short description of the steps involved in this procedure is as follows:

1. The raw data which contains the hit information along with the detectors table is fed to CORAL for track reconstruction. Kalman filter is used for track reconstruction.
2. The output from the reconstruction is obtained in form of a mini data storage (mdst) format which is analysed using PHAST.
3. Residuals are calculated and fitted with a standard Gauss function to extract the peak for the residuals. An example for a specific plane is shown in fig.(6.2). This procedure is performed for each plane of the detector.

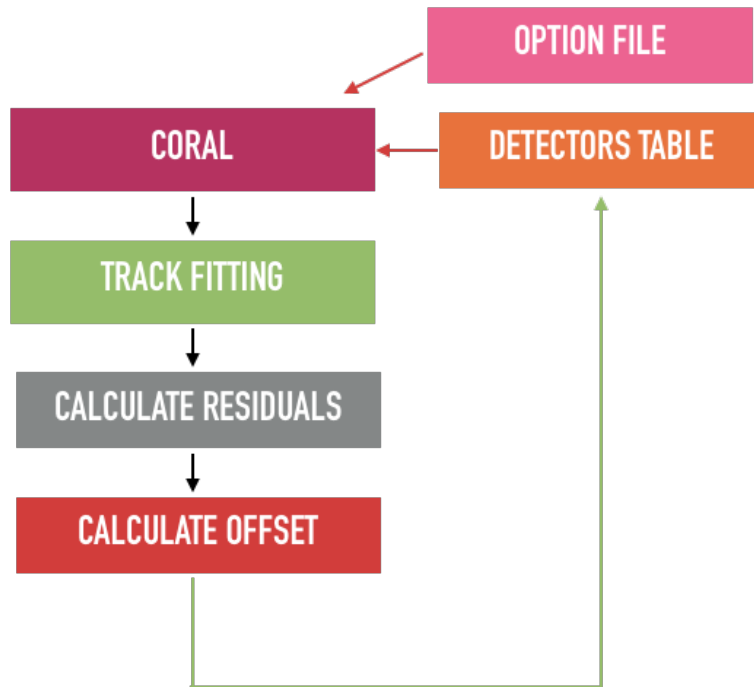


Figure 6.1: Pictorial representation of the previously used method

4. The fitted peaks are the shifts for the detectors and for a good alignment should be centered to zero. These shifts are applied to the detectors table. For the next iteration the new updated detectors table is used as an input to CORAL.
5. The number of iterations are selected by looking at the change in the reduced chi-square. This procedure is not automated at this point.

Such a procedure has many limitations and can even lead to situations where there are simultaneous shifts in opposite directions. This procedure can only align for the X and Y planes of the detector and is not currently structured to include rotation of the planes of the detector. These problems are described in detail by V.Blobel in [27].

6.2 Millepede

Millepede is an iterative alignment program that uses the linear least square method to fit and minimize all the relevant alignment parameters. The method and the initial implementation was developed by V. Blobel from the University of Hamburg and is maintained by Deutsches Elektronen-Synchrotron (DESY) [28]. It is a smarter implementation of the previously used method that decreases the computation time while giving comparable results. The alignment parameters that Millepede tries to minimize can be separated into two categories: *global* and *local*. Global parameters consist of sets of values that affect all data such as expected

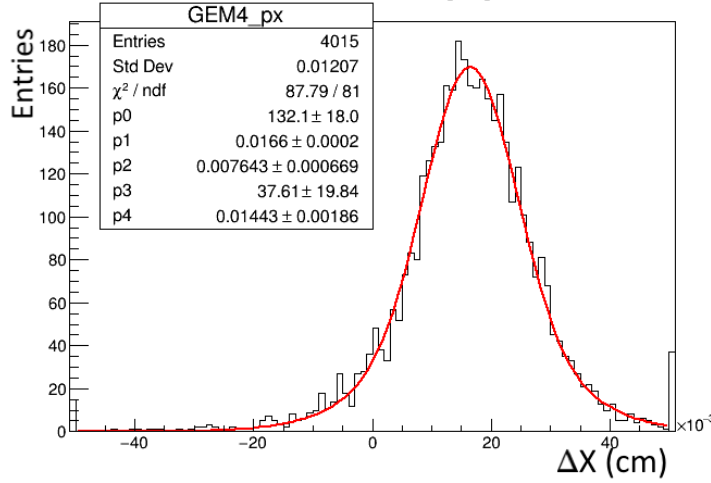


Figure 6.2: Fitting of the residual for the X plane of GEM4

shifts for the detectors. On the other hand local parameters are values that are concerned with a single track such as slope, curvature etc. The previously used method ignores the global parameters and only aligns using individual tracks from measured events. If one of the detectors has a lot of noise for some reason the iterative residual based alignment may fail. This and many other reasons such as an inability to tangle correlated parameters while aligning makes the previously used method inferior compared to Millepede.

Following is the mathematical description of the Millepede algorithm which is closely adapted from [29, 30]. Let the local parameters be denoted by l_j where j is the running index dependent on the complexity with which the track is described. For a general measurement the set of measurements at a detector plane k is given by

$$y_k = l_1 \cdot \delta_{1k} + l_2 \cdot \delta_{2k} + \dots l_n \cdot \delta_{nk} = \sum_{j=1}^n l_j \cdot \delta_{jk} \quad (6.1)$$

where δ_j are some known constant factors. For example if the track measured at a detector, at position k , is a straight line track then: $y_k = l_1 \cdot 1 + l_2 \cdot S_k$, where l_1 is the intercept and l_2 is the slope of the measured track. Here we assumed that the measurements are only dependent on local parameters. Similarly if we include global parameters g_j then

$$y = l_1 \cdot \delta_1 + l_2 \cdot \delta_2 + \dots l_n \cdot \delta_n + g_1 \cdot h_1 + g_2 \cdot h_2 + \dots g_u \cdot h_u = \sum_{j=1}^n l_j \cdot \delta_j + \sum_{i=1}^u g_i \cdot h_i. \quad (6.2)$$

Linearising the above equation for a single point measured at location x_i and track k yields:

$$y = f(x_i; \mathbf{g}, \mathbf{l}) + \left(\frac{\partial f(x)}{\partial \mathbf{g}_i} = d_i^{global} \right)^T \Delta \mathbf{g} + \left(\frac{\partial f(x)}{\partial \mathbf{l}_i} = d_i^{local} \right)^T \Delta \mathbf{l}_k \quad (6.3)$$

with $f(x_i; \mathbf{g}, \mathbf{l})$ being the mathematical model predicting the track and $\Delta \mathbf{g}$ and $\Delta \mathbf{l}$ are the corrections applied to global and local parameters after one iteration of a track fit.

The least square method requires us to solve the following matrix equation:

$$\begin{bmatrix} \sum_k C_k^{global} & \dots & H_k^{global-local} & \dots \\ \vdots & \ddots & 0 & 0 \\ (H_k^{global-local})^T & 0 & C_k^{local} & 0 \\ \vdots & 0 & 0 & \ddots \end{bmatrix} \times \begin{bmatrix} \Delta \mathbf{g} \\ \Delta \mathbf{l}_k \end{bmatrix} = \begin{bmatrix} \sum_k b_k^{global} \\ \vdots \\ b_k^{local} \\ \vdots \end{bmatrix} \quad (6.4)$$

here C is a symmetric matrix formulated as $C = \sum_{k=1}^m w_k d_k d_k^T$ with $w_k = 1/\sigma_k^2$ being the weight assigned to each measurement and m being the total number of global parameters being fitted and d_k being the derivative of the model with respect to the global parameter. A similar formulation is made for local parameters. H_k is a matrix formulated in a similar way as to C and is defined as $H = \sum_k w_k d_k^{global} (d_k^{local})^T$. b is the correction vector defined as $b = \sum_k w_k r_k d_k$ with r_k being the residual as defined in sec.(5.2.1).

The Millepede algorithm implements a simultaneous fit for all tracks, including both local and global parameters. Since we only care about corrections to the global parameters the computation is sped up by focusing on $\Delta \mathbf{g}$ calculation for each iterative step and solving the equation $\Delta \mathbf{g} = (C^{global})^{-1} b^{global}$.

The step by step process of the Millepede minimization can be explained as follows:

1. Fit the track using a fitter such as Kalman and extract the best values for local parameters.
2. Collect derivatives d_k for all local and global parameters that need to be minimized.
3. Update the matrices C^{global} and b^{global} for each track by simple addition. An extra step is needed to update matrix $C := C - HVH^T$ which indirectly includes the changes applied to the local parameters while updating the global parameters.
4. Repeat the above steps for all the available tracks.

After all the tracks have been computed and the relevant global matrices have been calculated the final equation $\Delta \mathbf{g} = (C^{global})^{-1} b^{global}$ is solved. The inversion while calculating this equation is made even faster by partitioning the matrix into symmetric sub-matrices which is one of the special features of Millepede and is described in detail in [29].

The whole process of looping over all tracks and then computing the correction to the global parameters counts as one iteration of the Millepede algorithm. The selection for

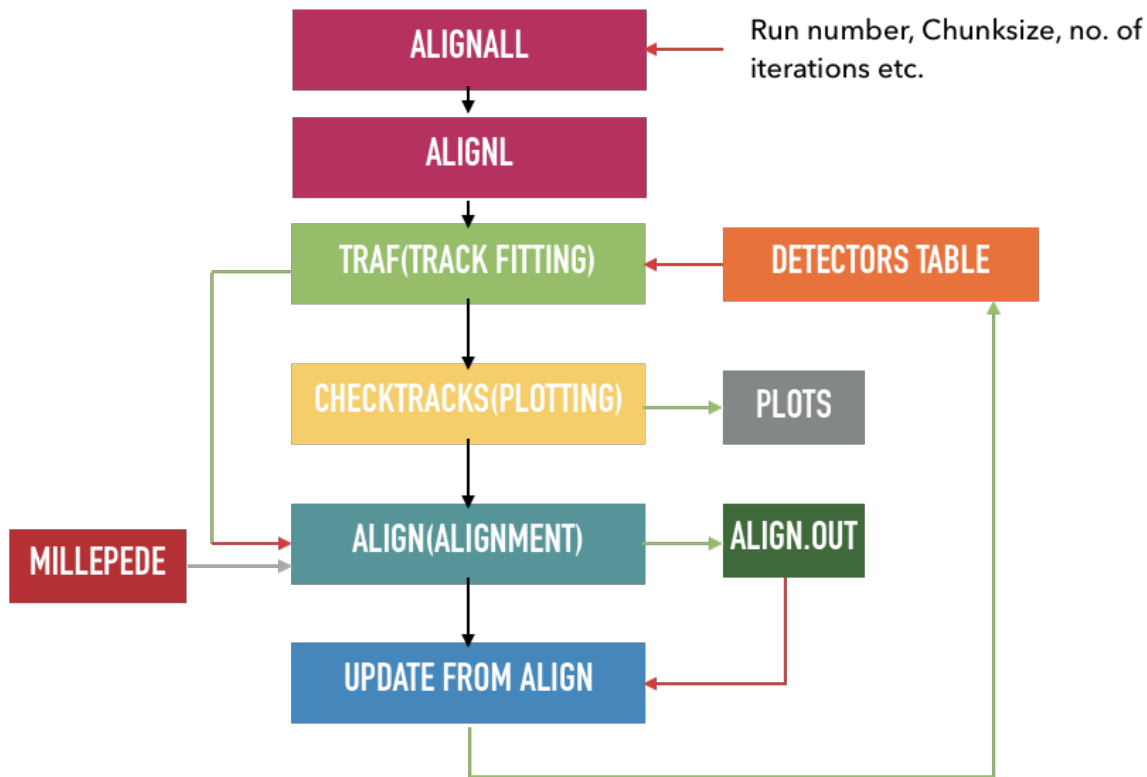


Figure 6.3: CORAL implementation of Millepede. The black lines signify the order of the steps while the green and red lines depict output and input respectively.

the number of iterations depends on the number of global parameters being used and the correlation between them if any.

6.3 CORAL Implementation

The Millepede program is included as a separate library "millepede.f" in CORAL. The algorithm is written in FORTRAN and H.Pereira [31] introduced an interface for the algorithm into CORAL. The options available for global parameters that can be minimized are positional(U) alignment, angular(T) alignment, pitch(P) alignment, alignment for the z position of the detector along the beam and many more which are not relevant for our tracking detectors.

The alignment method used in CORAL works on the standard Millepede condition which minimizes the sum of χ^2_{red} with respect to the local and global parameters. The method in CORAL is controlled using separate option files similar to the ones used in track fitting. The data flow for the whole alignment process is described in fig.(6.3).

⇒ "Alignall" and "Alignl" are bash scripts which are used in standard COMPASS alignment for staging the required data files for which the alignment needs to be performed. They

also stage external files that CORAL needs such as the Dico file (faster bridging) for track fitting. The bash scripts are also involved in data management and in cleaning up of intermediate files produced during the alignment procedure. The bash scripts control the data flow and invoke different option files. the process begins by invoking the track fitting in CORAL which starts the alignment procedure. These scripts were adapted to work with NA64 and new options were introduced for the experiment.

- ⇒ Track fitting uses the standard option file used for track reconstruction in NA64 with a few extra options. The most important option that is required to fill the root trees on which alignment works is "main do alignment". Other options such as whether to use the magnets and tracks having a non-zero momentum for alignment can also be set depending on the requirements. Both of these were used for the results mentioned in this thesis.
- ⇒ Next the "checktracks" option is called. This option is used for plotting and checking the effect of each alignment step. It helps to achieve an immediate quality check and can be useful to spot errors in track reconstruction. It also gives basic information such as the alignment performance per iteration. For the first iteration step it gives the results of track reconstruction done on the setup where no software alignment was performed.
- ⇒ Further, the "align" option is summoned. The "align" option is fed with the track reconstruction output from CORAL along with the detector positions. Moreover, the kind of global parameters that need to be minimized are specified at this stage. Other options such as aligning specific detectors, track selection cuts and inputting specific detector resolutions are also available. The Millepede minimization is invoked at this point. The "align" option gives an output with the required correction for each detector, for the particular global parameter that was aligned.
- ⇒ Next the output from the "align" option is fed to "updateFromAlign". This tool applies the correction to the detectors table to create a new "detectors.dat" which is used for track fitting in the next iteration if multiple alignment iterations are performed.

6.4 Results

The alignment procedure was performed for the data collected during the 2017 invisible mode run for NA64. During this period, data taking and calibration were performed using a 100 GeV e^- beam. The results of the alignment were tested by performing track fitting on the last obtained detectors table after all Millepede iterations were completed. The tracks used to obtain the quantifiable values for judging the results were chosen such that one hit from **each** detector plane contributed to the fitted track. In 2017 there were four Micromegas (MM1-MM4) upstream of the magnets and two Micromegas (MM5-MM6) and four GEMs (GEM1-GEM4) downstream of the magnets. The total number of detector planes

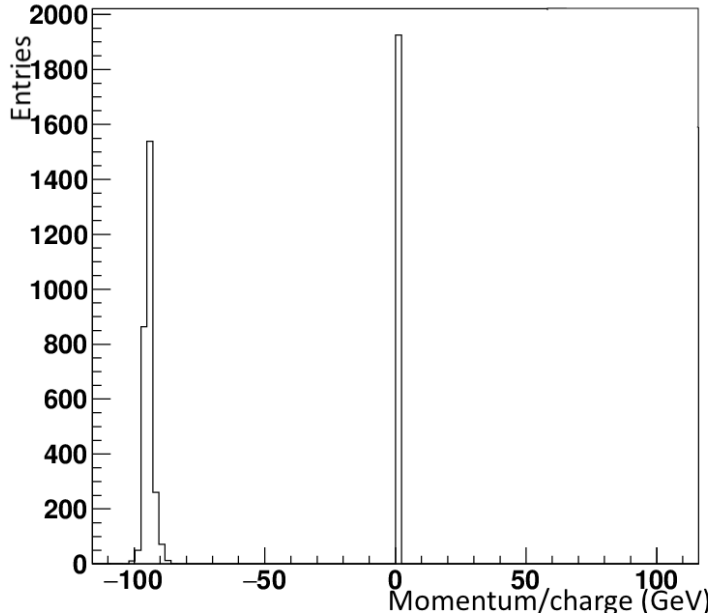


Figure 6.4: Charge over momentum distribution of all fitted tracks during alignment

available during the NA64 operational period were 19 since the Y plane of GEM3 was not operational. Since both the track fitting and alignment processes use detector resolution during minimization it is important to mention that for these results the resolution for GEMs was fixed at $50\mu m$ and for Micromegas it was fixed to be $100\mu m$. A random physics run with number 3211 was chosen to observe the results of the procedure. The results from this run were also compared to the ones obtained by the previously used procedure in [26]. 500000 events per run were analyzed and CASTOR file system was used to access the data to study the process for a future run-by-run alignment application on the CERN computer cluster (lxplus). Different global parameters were minimized to study their individualized effects. The final conclusion about the quality of the alignment was drawn upon by looking at the reduced chi-square χ^2_{red} distribution and the distribution of residuals.

6.4.1 Positional Alignment

The first global parameter which was aligned using the Millepede algorithm were the X and Y positions of the tracking detectors. In CORAL each readout plane of the detector is available to be aligned individually. Positional(U) alignment refers to the alignment done to achieve an optimal (x,y) position for each detector plane. During the U alignment all detector planes were left free for movement in the (x,y) positions. However, other positional variables such as the angle with respect to the geometric reference system, z position and the pitch of the detectors were fixed. The tracks used for alignment were chosen to have $\chi^2_{red} < 100$ and a $-110\text{GeV} < p/\text{charge} < -90\text{GeV}$. The momentum over charge cut fig.(6.4) made sure that

only tracks that were bridged through the magnets were used for alignment. The results from the alignment are shown in figures (6.5), (6.6) and (6.7).

Ideally the residual distribution for a perfectly aligned detector should be centered around (0,0) which signifies that the measured hit position is accurately fitted during the track fitting procedure. As it can be seen from the figures, initially the residual distribution of almost all the detectors is displaced. Even though the observed displacement is small $O(0.02\text{cm})$, such a shift can hamper the positional resolution of the detectors which is expected to be of the $O(\mu\text{m})$. This provides us with a visual proof that a software alignment is very much necessary. The final residual distribution after the Millepede alignment is much more uniform and is mostly centered around (0,0). The effect of the alignment is also measured by calculating the χ^2_{red} of all the selected tracks before and after alignment. We see in fig.(6.8) that the distribution shifts to a lower value which signifies that the alignment resulted in tracks with a lower χ^2_{red} i.e a better fit.

The Millepede implementation was also compared to the previously used method (sec.(6.1)). The χ^2_{red} comparison is shown in fig.(6.9). We again observe a lower χ^2_{red} distribution for the tracks in comparison to the one from the previously used method, though in this case the difference is not as drastic as the one seen before. This figure gives us a quantitative indication that the Millepede alignment method is in-fact better than the one which was previously used, which was expected. Although, the difference between the methods is not very large which shows that the previously used alignment method gives a reasonable detector alignment. The individual residual distributions of the detectors for the previously used method are presented in appendix (A).

Looking closely at the residual distribution for the GEM detectors in fig.(6.5) one also observes a strange correlation between the residuals of the two planes. This behaviour is not expected since residuals in individual planes of the same detector should ideally be independent of each other (perpendicular strips). Such a distribution might be observed if there is an inherent angle between the two strip layers which even though highly unlikely cannot be completely ignored. This explanation is checked using angular alignment in the next section. Another reason for this behaviour might be due to our Micromega detectors. As mentioned before these detectors are set up such that they are rotated by a 45° angle with respect to the global reference system which is also the reference system of the GEMs. Since the observed correlation also has an approximate angle similar to that of this rotation, the bad resolution of the Micromegas particularly in one plane as explained earlier might be the reason of these observations. This reasoning was checked by refitting the tracks and recalculating the residuals for the GEMs for the case where MM5 and MM6, the two downstream Micromegas were switched off and not used during the track reconstruction. The results of this check can be seen in fig.(6.10). From the figure it is clear that the correlation in GEMs was due to the downstream Micromegas. Once they are switched off we are still left with a fairly large spread for the X residual, this might be due to the spread in the momentum when the beam passes through the magnet since X is the bending plane for our magnetic field. The increased events observed in the histograms on the right are due to the total number of events analysed in the run which was doubled while performing the initial track fitting.

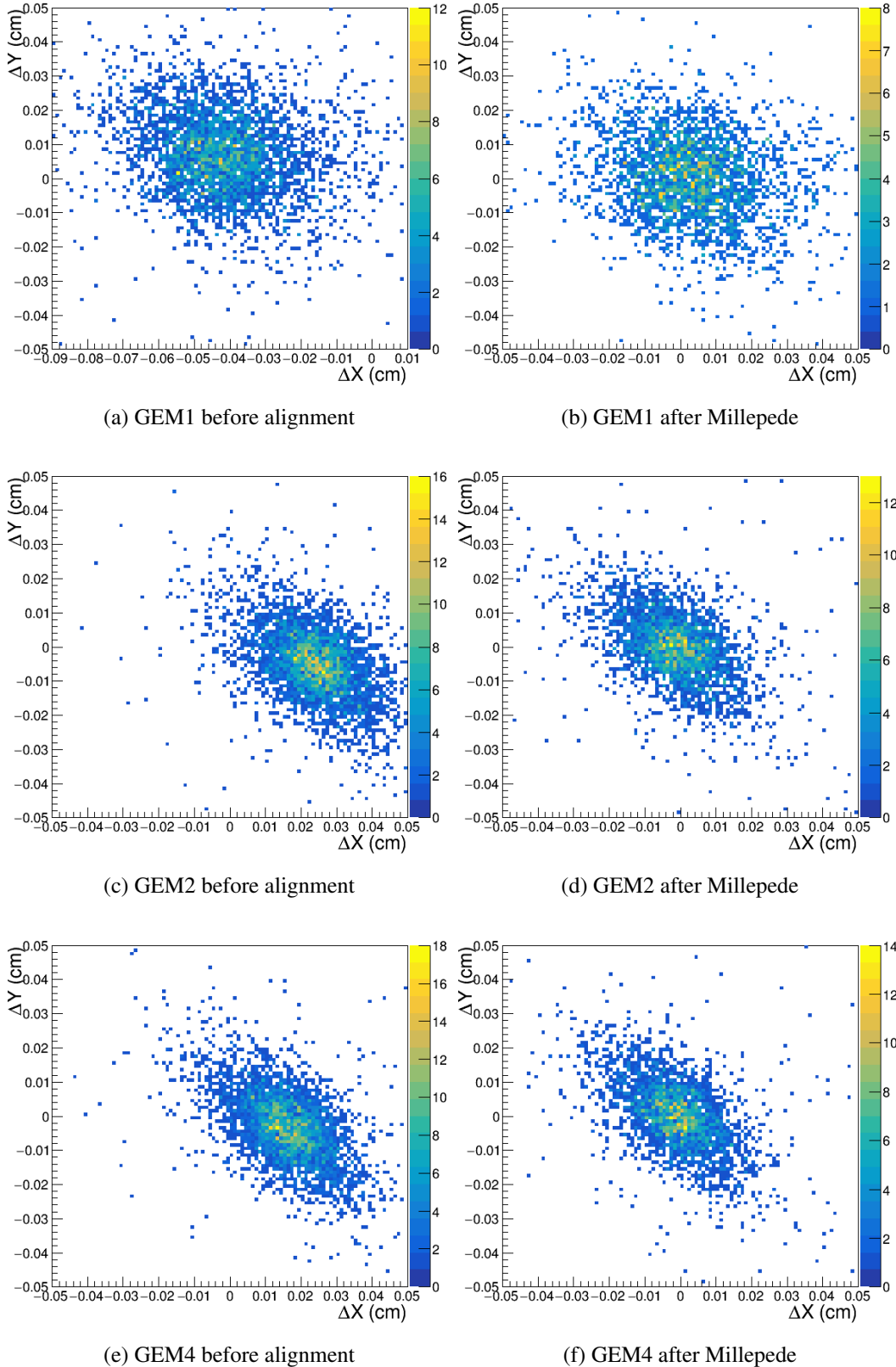


Figure 6.5: Residual of GEM detectors

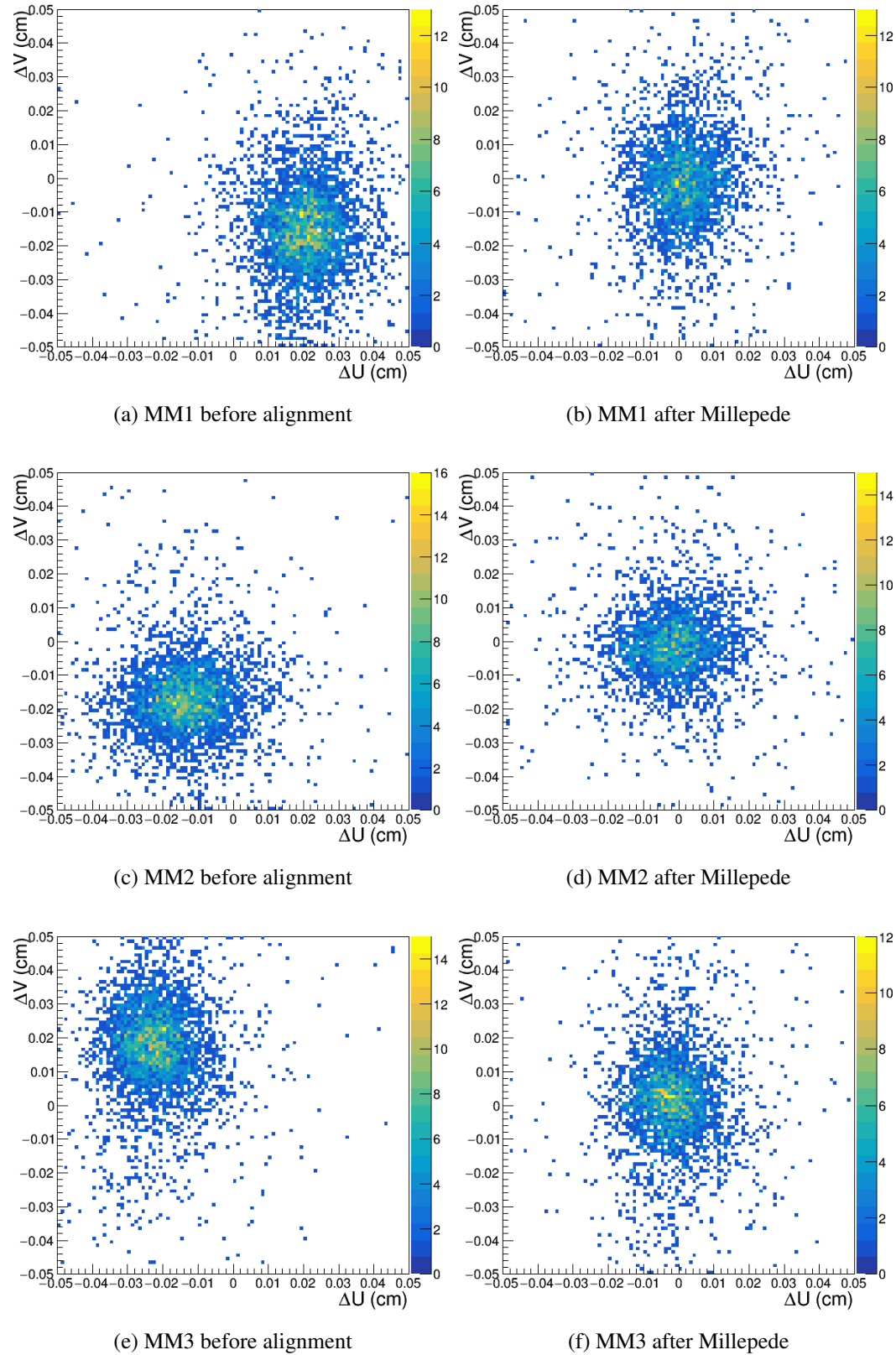


Figure 6.6: Residual of Micromega detectors

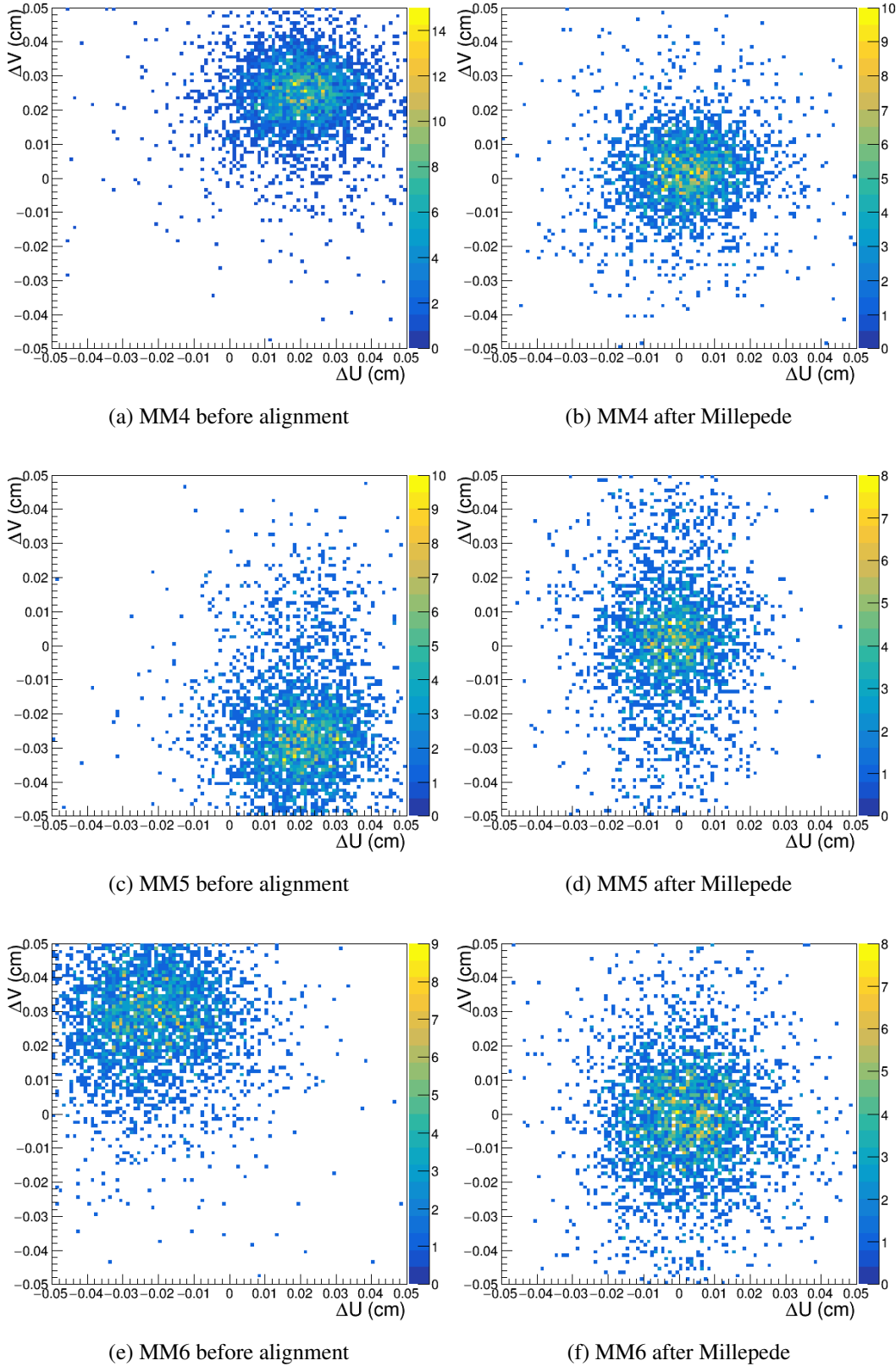


Figure 6.7: Residual of Micromega detectors

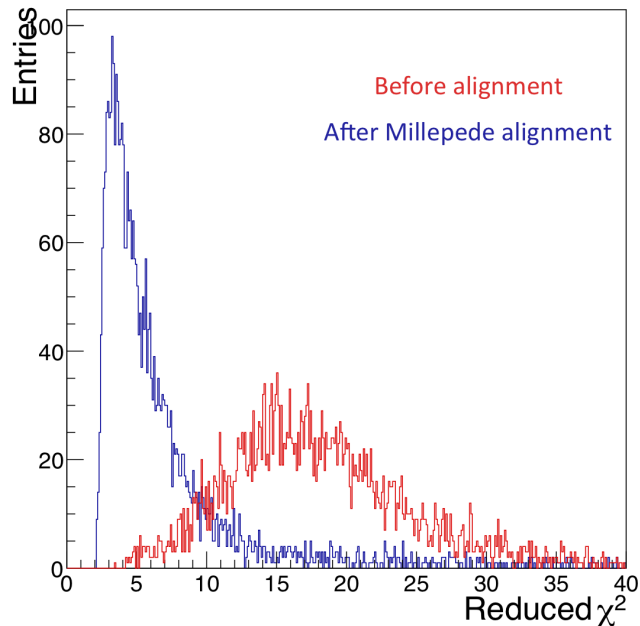


Figure 6.8: χ^2_{red} comparison before and after Millepede alignment implementation

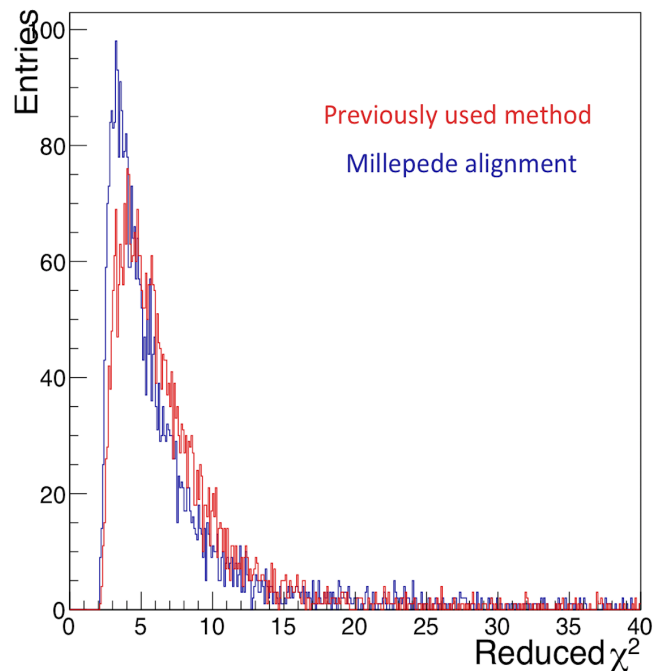


Figure 6.9: χ^2_{red} comparison of previously used method with Millepede alignment implementation

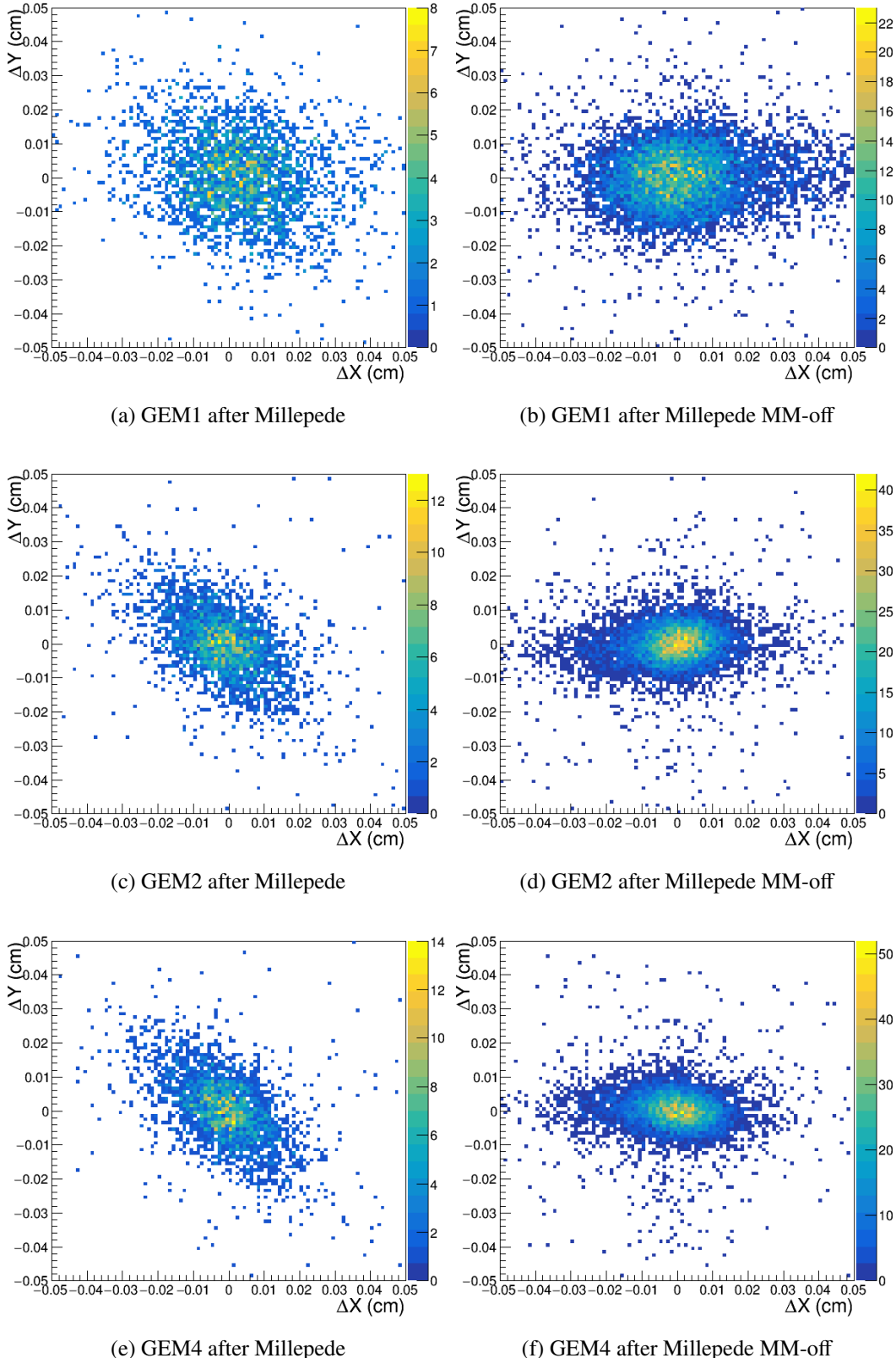


Figure 6.10: Residual of GEM detectors with downstream Micromegas switched off

6.4.2 Angular Alignment

Another global parameter that can impact the tracking resolution is the angular displacement. Each plane of the detector has a particular angle with respect to the global reference system. In the case of the GEM detectors used in our setup one plane is at 0° with respect to the global system and this plane is named the X plane, on the other hand the Y plane, which is the readout plane perpendicular to X is at 90° w.r.t the global system. This essentially means that the reference system for our GEMs is the same as that of the experiment. In the case of the Micromegas, the internal detector reference system is rotated by 45° w.r.t the global system. To check whether an angular alignment was needed after the previously performed positional alignment for our setup, the obtained residuals were plotted against the position of hit for each plane of the detector. The results for the GEM detectors are shown in fig.(6.11) while the ones for the Micromegas are given in appendix(A). It was observed that for most of the detectors the residuals have no dependence on the position except for the case of GEM1, particularly for the X plane. To correct for this dependence an angular alignment was performed.

The angular(T) alignment was performed using the detectors table obtained after six iterations of the positional alignment(U) mentioned before. Initially during the T alignment only the X and Y planes of GEM1 were left free to rotate and all the other detector positions along with their respective angles were fixed. This was done to measure the impact of the alignment for one single detector. GEM1 was chosen since it was seen that the residuals for the X plane of the detector seemed to have a dependence on the position of the hits in the detector. The tracks used for alignment were chosen to have $\chi^2_{red} < 100$ and a $-110\text{GeV} < \text{p/charge} < -90\text{GeV}$. The result of the T alignment for GEM1, X plane is shown in fig.(6.12). As it is seen in the figure the impact of the T alignment is minimal. However, it is important to mention that the result shown here was obtained after three iterations of the Millepede algorithm since the further iterations failed. The failure was during the CORAL part of the procedure which prohibits a change in the angle greater than 5° for the GEM detectors. In spite of this restriction the three iterations should be more than enough to solve the angular displacement which is not the case. It was also found that the individual X and Y planes of the detector do not stay perpendicular to each other after the T alignment. This is unexpected since even though in CORAL they are treated as separate detectors, in reality the angle between them in the detector reference frame is fixed by construction. The observed angles for the planes were 89.563° for the Y plane and -0.324° for the X plane after alignment i.e there is about a 0.2° shift in the inherent angle between the two readout planes. This was confirmed to be a possibility which might have arisen during the detector construction particularly the chemical etching process [15] used to construct the readout strips. This might also explain the angular dependence of the residuals observed in GEM1. Fig.(6.13) shows the χ^2_{red} before and after T alignment. We do see some shift towards a lower value but the overall shape of both the distributions is similar, reiterating the fact that the impact of the angular alignment is minimal for our setup at least in the case where we only align for one detector.

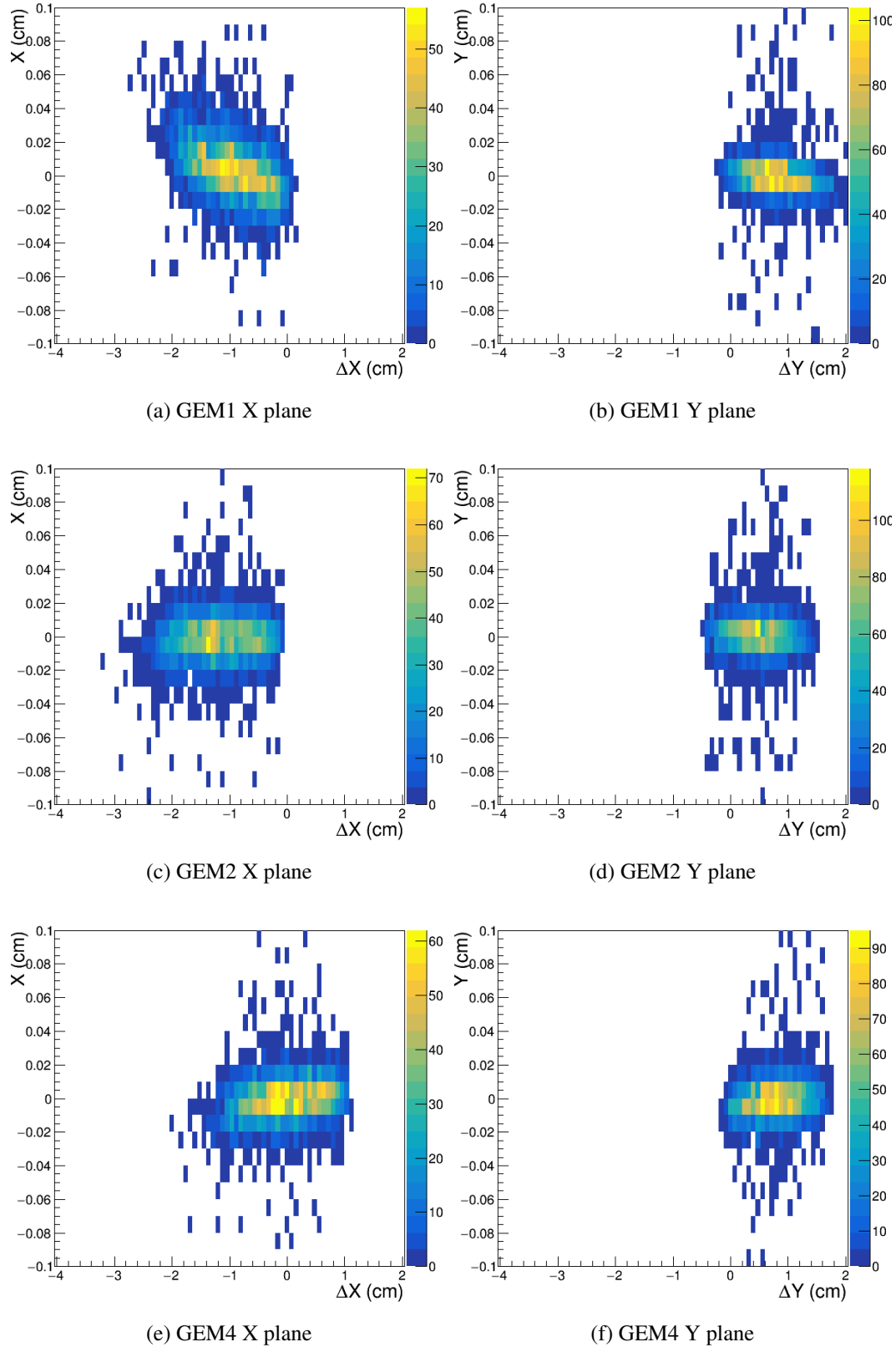


Figure 6.11: Residual vs position for GEM detectors

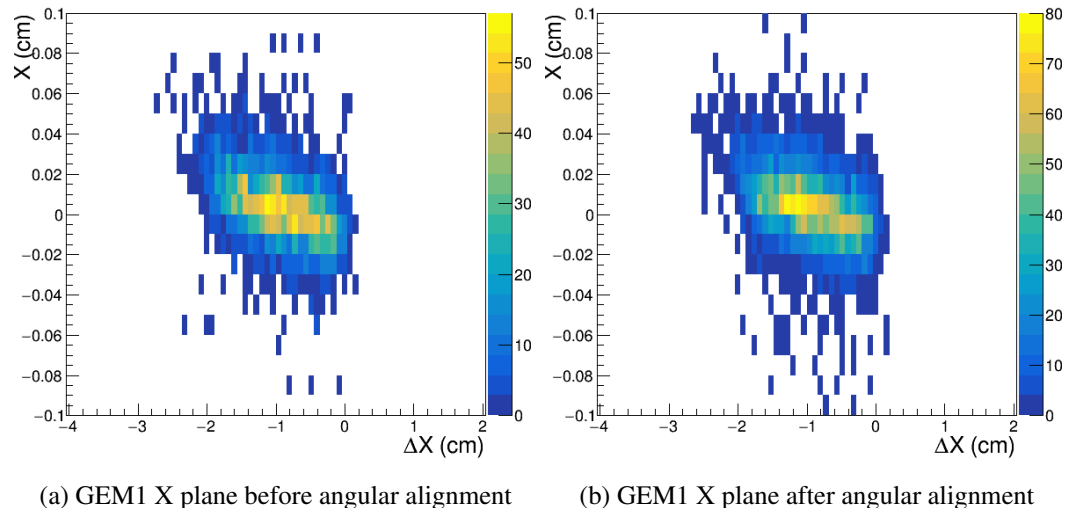


Figure 6.12: Angular alignment

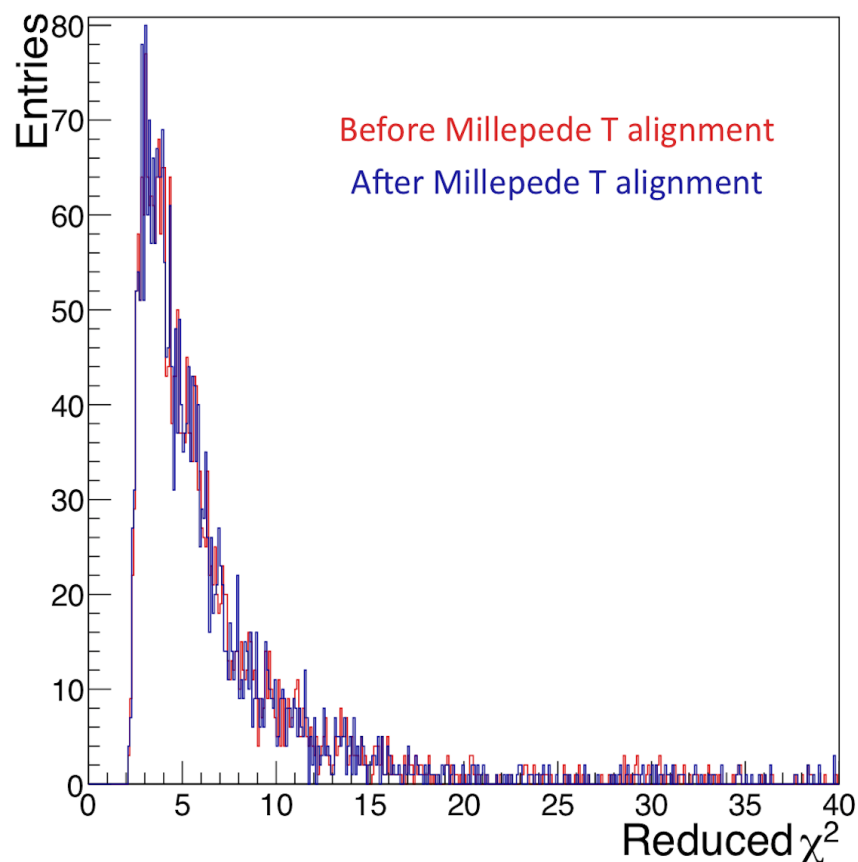


Figure 6.13: χ^2_{red} comparison before and after Millepede T alignment implementation

6.4.3 Positional+Angular Alignment

The end goal with the whole alignment procedure is to obtain the best possible alignment for each detector. Hence, the procedure was studied with both U and T alignment turned on. Since the slight shift in the angle which was observed during U alignment was only present in a small number of detectors and is more prominent in GEM1 the impact of a U+T alignment was similar to that of U alignment. This alignment was performed just to check whether the alignment algorithm works if multiple global parameters are minimized in unison. The alignment was observed to be operational and the χ^2_{red} obtained was similar to that shown in fig.(6.8). The impact of the T alignment might not be visible for the particular run that was analyzed since the angular displacement for the detectors was minimal. However, for a future run by run alignment a full U+T alignment should be performed to correct for any possible angular displacement since for NA64 the experimental setup is constantly changing.

CHAPTER 7

Source follow-up analysis

The MC simulation for NA64 visible mode for the 2018 setup has been implemented by the collaboration in GEANT4. The information from the MC simulation is currently reconstructed in a standalone reconstruction program similar to how it is done for real data. This chapter tries to document how the simulation is implemented. This is an important facet since the type of process we are trying to study is not part of the SM and is required to be implemented as an extra step to a standard GEANT4 simulation. Though these processes were added in the physics code [32, 33] it is still important to document how they are included in a simulation.

Since one of the main goals is to implement the data analysis chain in CORAL, reconstructing the MC simulation output (MCTruth) in CORAL is a part of this goal. Thus, the chapter also details the changes made to the MCTruth to make it compatible with CORAL along with the results of the said reconstruction.

7.1 A' Production

A' production in the NA64 simulation has been described in [32]. A short summary for the procedure is as follows:

- The emission probability for A' production for an active target which in our case is fixed to be Pb is given as $P_{emission} = \rho N_A \sigma_{tot}^{A'} \Delta L_i / A$ where ρ is the density of the target, N_A is the Avogadro's number, $\sigma_{tot}^{A'}$ is the total cross-section for the A' production in a bremsstrahlung like reaction as mentioned before, ΔL_i is the step length of the electron path in the target and A is the atomic weight.

The total cross-section is approximated by using IWW approximation however as it is seen in the fig.(7.1), ETL calculation is more accurate and complete. The error in the cross-section calculation is fixed by introducing a K-factor defined as $K = \sigma_{IWW}^{A'} / \sigma_{ETL}^{A'}$.

- A sample variable u_1 is randomly sampled from a uniform distribution over the unit

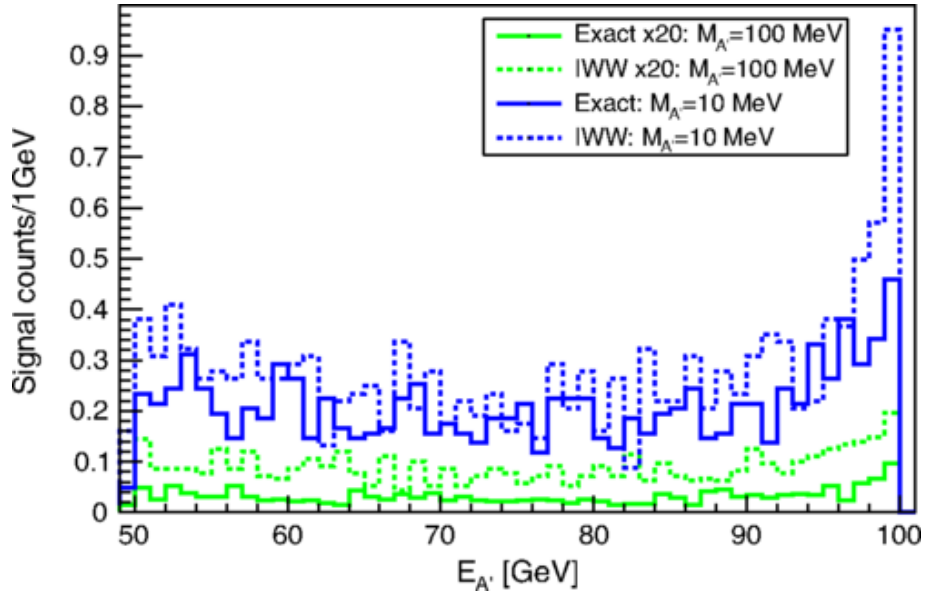


Figure 7.1: Number of simulated signal events at two A' masses as a function of Dark Photon energy [32]

interval $[0,1]$. If u_1 is found to be smaller than the emission probability $P_{emission}$ the simulation for A' proceeds further.

- For an A' emission a random picking for the relevant kinetic parameters x , $\cos\theta$ and the azimuthal angle ϕ is done. The simulation for A' emission and decay continues if the parameters are accepted after rejection sampling.
- Next the kinetic energy for the emitted A' is set. Based on this value it is checked whether at the simulated A' mass the dark photon can escape the subsequent WCAL catcher which is directly after the active target for the visible mode. If this is true then the A' is simulated to decay into e^+e^- and the relevant information about A' and the decay particles which include mass, decay position and momentum is recorded.

7.2 Tracking Detectors

NA64 consists of two sets of tracking detectors namely Micromegas and GEMs. In the visible mode simulation two Micromegas named MM1 and MM2 are placed upstream of the two magnets and two more named MM3 and MM4 are placed right after the vacuum tube and before the WCAL. Four additional GEM detectors are placed right after the downstream WCAL. Both GEMs and Micromegas have the same implemented internal structure in the simulation. The structure consists of an Argon gasbox surrounded by two Mylar layers on

either side. An additional layer of Copper and PCB is added after the second Mylar layer. The gas volume is set as sensitive for both Micromegas and GEMs.

While processing the output of the simulation for the tracking detectors the following information about each particle traversing the detector is recorded- x,y and z hit positions, energy deposited, trackID of the particle, the PDG [34] encoding of the particle and the kinetic energy. The trackID is a unique ID which GEANT4 gives to each particle simulated and tracked during the simulation. The trajectories and the origin of *all* the simulated and tracked particles are not saved in the current format. Some trajectories such as those of the beam particle and the simulated A' along with its decay products is available. Saving all trajectories should be considered in the future since the information is useful for reconstruction.

To reconstruct the simulation output it was modified to a format that can be read in CORAL described more in appendix(B). This comprised of including information such as a unique identifier for each tracking detector (Detector name + DetectorID), particle trajectories for relevant simulated particles and splitting the information to individual detector planes for implementation in CORAL. Additional options were provided in the track fitting option files to activate MC decoding. The reconstruction in GEMs proceeds in the following way:

1. For an event CORAL reads in the hit positions for the individual detectors and checks the validity of the TrackIDs against provided trajectories.
2. Next it moves on to the detector response simulation where it uses the hit data along with extra simulation parameters to simulate three amplitudes for each detector. The simulation parameters include space resolution of the detector (mm), effective gain of the detector along with the standard deviation, signal width (mm) and time resolution (ns) if the timing information is available. The simulation parameters are fed through the track option file.
3. The simulated amplitude is calculated as follows, $amp = \frac{1}{\sqrt{2\pi}} \frac{(\text{Energy deposited} \times (\text{Effective gain} + \sigma_{\text{Gain}}))^2}{\text{signal width}}$ with inbuilt cuts to remove meaningless hits.
4. The simulated amplitude for the hit is then assigned to the nearest readout strips it might corroborate to.
5. The amplitudes for each strip are then passed to clusterization and tracking.

The reconstruction for the tracking detectors is evaluated by looking at the reconstructed momentum.

7.3 Calorimeters

As mentioned before, NA64 consists of three types of calorimeters namely WCAL, ECAL and HCAL in the visible mode setup. The WCAL is simulated to consist of three layers similar to the real setup. These are the pre-shower, main and the catcher. After the simulation

the total energy deposited in each layer is calculated for each simulated event. The ECAL also has the same structure in GEANT4 simulation as that of the experiment. It is separated into two layers of 6x6 cells each. Lastly, the HCAL consists of 4 modules with 3x3 cells each. These modules are shifted incrementally in the x position to cover the angle acquired by the beam after it passes through the magnets. Unlike the real setup the last module is not placed in the line of sight of the incoming beam before the magnets. Especially for ECAL and HCAL only the total energy deposited in each cell for each simulated event is processed. No other information regarding the hit positions of the particles that go through the calorimeters is collected.

The required format for calorimeters so that they can be read and reconstructed in CORAL is the same as the tracking detectors. An example of the formatted simulation output which was fed to CORAL along with its description is given in the appendix(B). During the reconstruction, the simulated data is just pushed through without any changes for all the calorimeters. Clusterization and track matching is not done since the opening angle of the $e^+ e^-$ pair produced due to the decay of A' is expected to be very small such that the currently used dimensions of the individual cells in the ECAL cannot separate the individual particle showers. This leads to the shower being contained within a minimum of one and maximum of two cells if the particle hits the boundary. Hence clusterization makes no sense. This fact is reiterated by the reconstruction results. In addition, since we have no information regarding the individual hit positions track matching cannot be performed in the current reconstruction. However, to study rare SM events such as dimuon production a clusterization in the HCAL to detect individual muon showers may be required.

7.4 Trigger Detectors

This category includes detectors like the SRD, Veto, Scintillators and Counters. In the 2018 simulation the SRD, VETO in front of the HCAL along with Wcounters(W0-2) were replicated. The SRD is split into SRD counters in the transverse direction similar to the one in the real setup (fig.(4.3)). The MC simulation consists of two counters instead of the three present in the real setup.

For this class of detectors only the information regarding the total energy deposited in the detector is important. Hence, during the reconstruction similar to the calorimeters, this information is pushed through for each detector. The reconstructed data for the triggers and the SRD can then be used in the further analysis by applying similar cuts on the energy deposited as that of the real data.

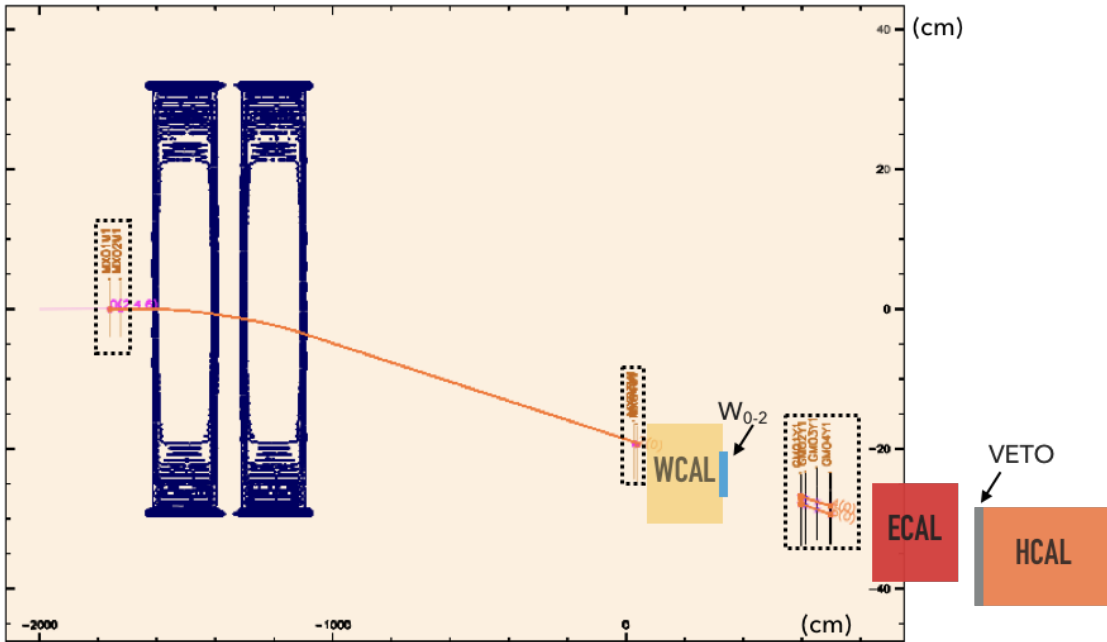


Figure 7.2: Track reconstruction display from CORAL.

7.5 Reconstruction Results

All of the studies mentioned below offer a proof of principle that the MC reconstruction in CORAL is operational and can be used in a more detailed analysis if required.

Fig.(7.2) shows the track reconstruction display output from CORAL along with a few modifications to depict the simulated detectors. The blue lines in the figure represent the measured magnetic field maps of the two magnets, the blue loops depict the change in magnetic field and the uncolored region signifies a uniform field in that area. The pink track on the left is the trajectory of the beam particle which hits the upstream Micromegas (MM1-MM2). The first orange track which ends at the downstream Micromegas (MM3-MM4) is used to extract the momentum of the incoming beam. These are studied in more detail in section(7.5.1). Further the energy deposited in the WCAL and the Wcounters (W0-2) is recorded. The event which is being shown here is one where a Dark Photon was produced. This was checked by looking at the sum of energy deposited in the calorimeters and the two tracks reconstructed in the four GEM detectors located after the WCAL. The two tracks are of the corresponding decay products of the A' which are the e^+e^- . These events are described more in section(7.5.2).

7.5.1 Momentum Reconstruction

The momentum reconstruction in CORAL was checked by selecting the reconstructed tracks which were bridged through the magnets successfully. It was made sure that all tracking detectors upstream and downstream that are involved in momentum reconstruction had a contribution to the track i.e each detector had a hit which was used to reconstruct the final fitted track. In our case this meant the four Micromega detectors.

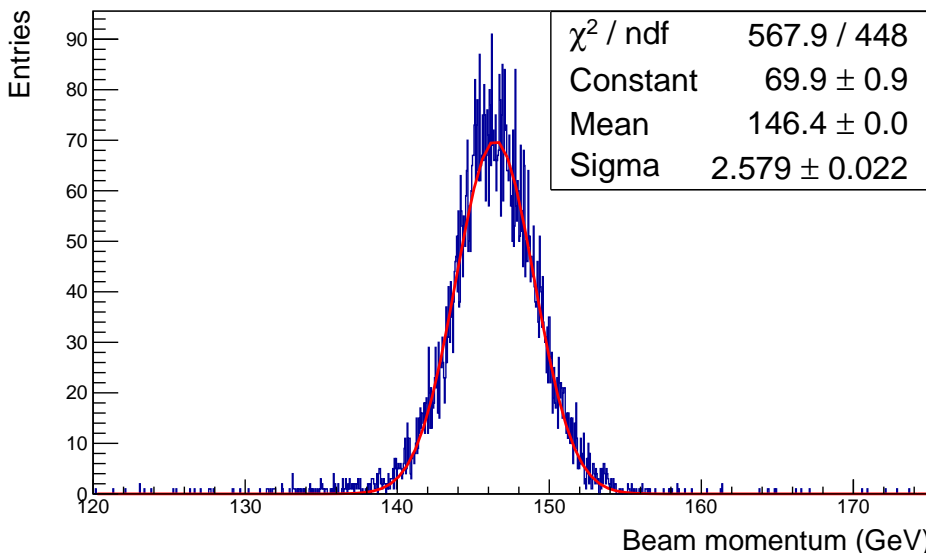


Figure 7.3: Reconstructed beam momentum in CORAL along with fit parameters.

Fig.(7.3) shows the reconstructed beam momentum. The momentum was fitted with a standard Gaussian function. The extracted momentum after reconstruction has a value of 146.4 GeV with an error of 2.58 GeV. Even though we have a beam which has a momentum of 150 GeV after simulation, we observe that the reconstructed beam momentum is much lower. Since the detectors in the reconstruction were placed at the exact position as that of the simulation, the reason for the observed beam momentum distribution can be either attributed to the difference in the integrated magnetic field between the simulation and the reconstruction or it can also be due to some systematic error of the track reconstruction and momentum determination algorithm. The Gaussian spread in the reconstructed momentum should be due to the resolution of the detectors mimicked in the reconstruction.

The magnetic field in the simulation is implemented as a box field with an integrated field strength of 7.85 Tm while in the reconstruction the measured field maps of the magnets made for the physics runs are used. Even though the integrated magnetic fields for both the implementations are almost the same the bending effect which might be present due to the fringe fields is only simulated during the reconstruction. This might be the reasons for the the underestimation of the calculated beam momentum compared to the one simulated.

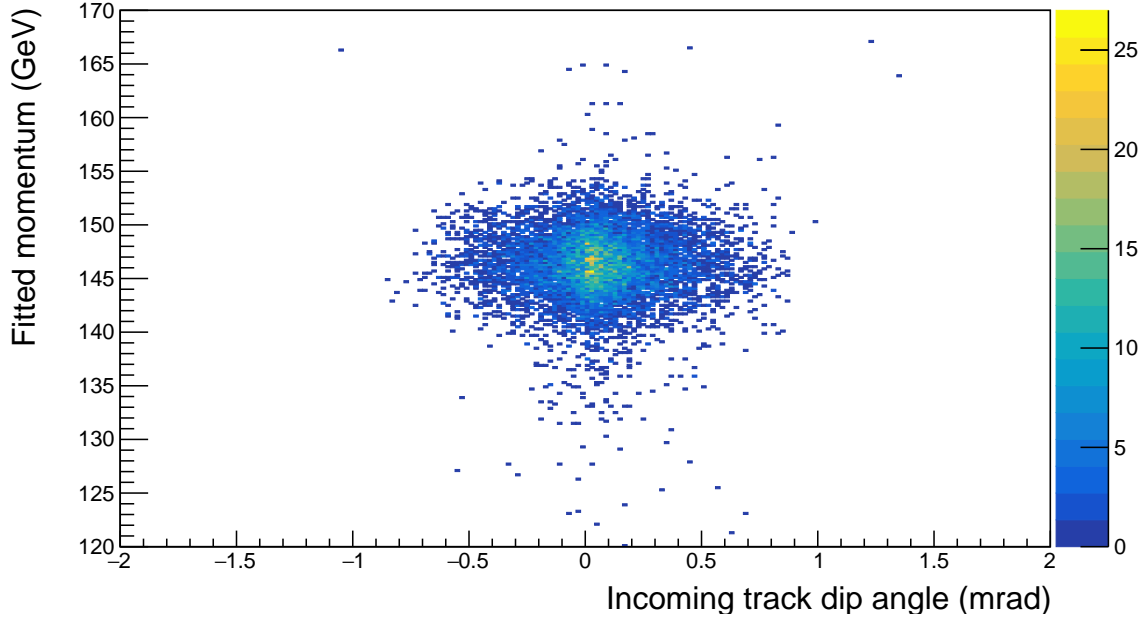


Figure 7.4: Fitted beam momentum vs dip angle of incoming track.

To check the performance of the tracking algorithm for momentum reconstruction the angles of the incoming track were compared to the fitted momentum after track fitting. Figures (7.4) and (7.5) show the obtained result. Both of the angles are chosen from the fitted track piece which is upstream of the magnet. The dip angle is defined as the angle of the track which moves it in a plane parallel to the magnetic field lines hence during the bending process this angle is not affected and does not contribute to the momentum reconstruction. As seen in the fig.(7.4) the fitted momentum over the distribution of the dip angle is uniform which is as expected.

The azimuthal angle is the angle of the track piece which moves it in a direction perpendicular to that of the magnetic field. This is the angle affected by the bending field of the magnet and is critical for momentum reconstruction. As we see in fig.(7.5) there is a correlation between the fitted momentum and the incoming track's azimuthal angle. This shows that during the reconstruction, tracks with varying azimuthal angles were reconstructed which led to a spread in the reconstructed beam momentum. This might add some systematic uncertainties to the beam momentum observed and should be investigated further examining the reconstruction algorithm in CORAL in future studies.

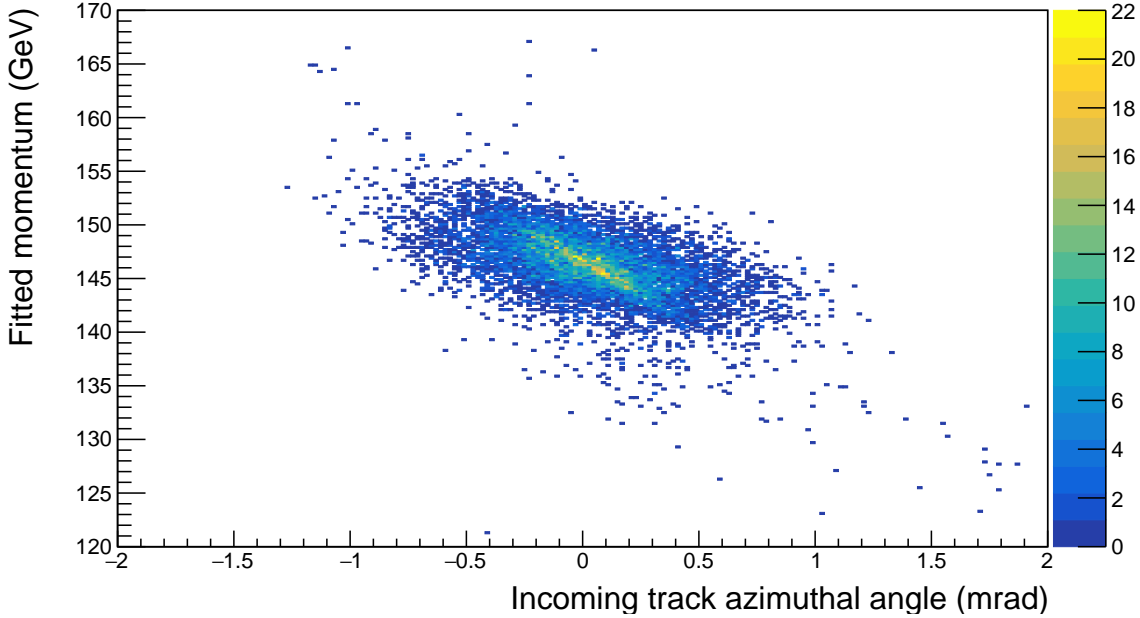


Figure 7.5: Fitted beam momentum vs azimuthal angle of incoming track.

7.5.2 A' Reconstruction

The A' reconstruction in CORAL was looked at in two stages. The first included identifying the A' events in the reconstructed sample and the second included studying the decay products of the A' which are the e^+e^- .

The A' events were selected by applying the following cuts:

1. $142 \text{ GeV} < E_{WCAL} < 150 \text{ GeV}$.
2. $E_{W_{0-2}}, E_{ECAL} > 0 \text{ GeV}$.
3. Two tracks in downstream GEM detectors.
4. $E_{VETO} = E_{HCAL} = 0 \text{ GeV}$.

These cuts helped separate the A' events from the rare dimuon events mentioned before. The angular distribution of the two track events were analyzed and is shown in fig.(7.6). The figure shows that most of the e^+e^- pairs produced from the decay of A' have a small outgoing angle. This is as expected since we assume that the A' which might be produced in a real physics event might be highly boosted in the forward direction which will result in a smaller opening angle for the decay products. The current expected limit for this opening angle for $1 \lesssim m_{A'} \lesssim 25 \text{ MeV}$ at $E_{A'} = 20 \text{ GeV}$ is $\theta \ll 2 \text{ mrad}$ as mentioned in [10]. This also validates our reasoning to not implement shower clusterization in the downstream calorimeters since

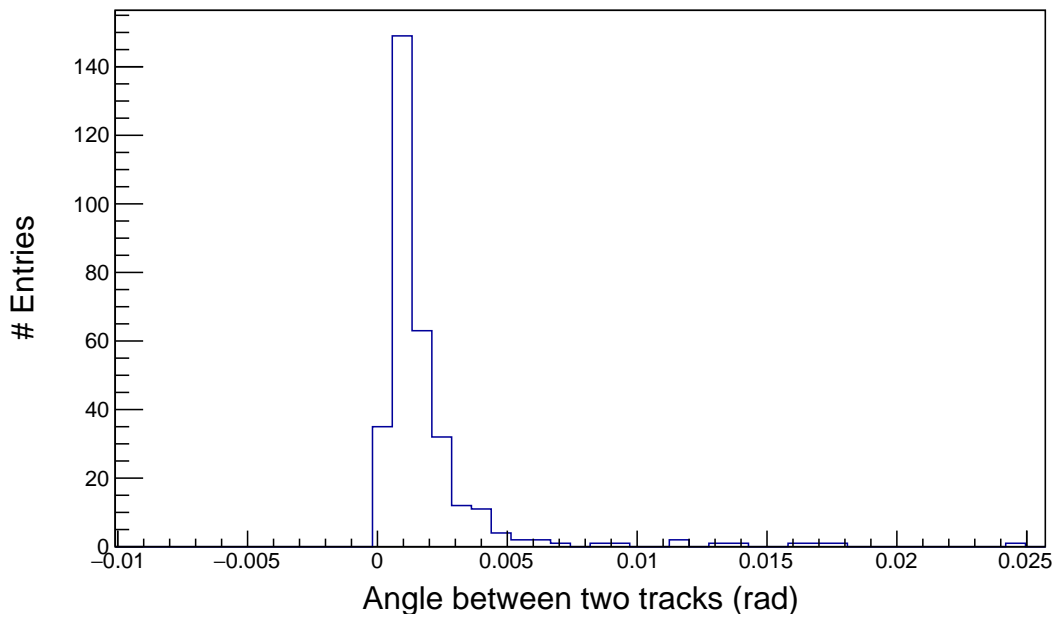


Figure 7.6: Angle between the outgoing e^+e^- tracks

at such small angles, with the current size of our individual calorimeter cell, the shower will not achieve the necessary separation required for identifying individual particles.

CHAPTER 8

Conclusion and Outlook

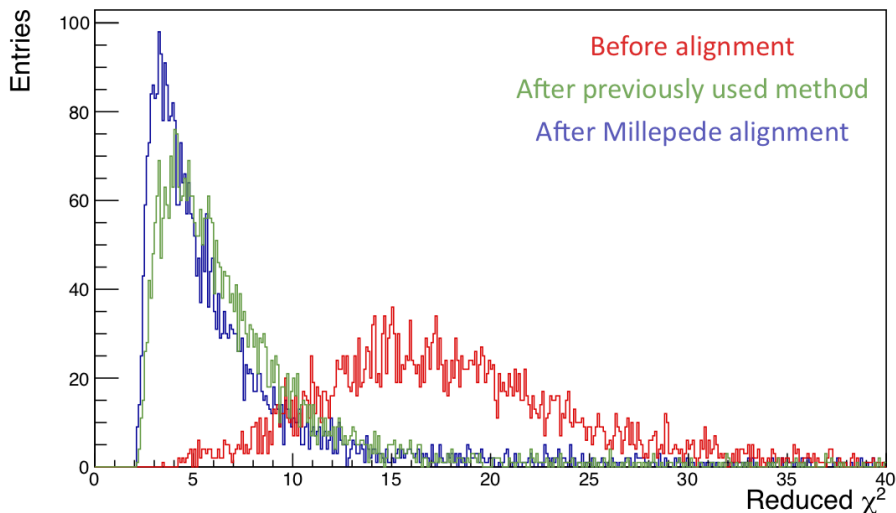


Figure 8.1: χ^2_{red} distribution for selected tracks showing the impact of Millepede alignment.

Alignment

During the course of this thesis a successful positional and angular alignment was performed for run 3211 using the Millepede alignment tool. As it is evident from fig.(8.1), a **run by run alignment** is required for the NA64 experiment to maximize the positional resolution of the tracking detectors. This in turn will make the beam momentum determination more precise which is a high priority for NA64. **Millepede** is one of the best available tools, is now compatible with the NA64 setup and can be used for this purpose.

Outlook

Since the results from the alignment also depend on the individual detector resolution a better estimate of the resolutions for both Micromegas and GEMs might be required before a final run by run alignment is performed.

Another global parameter which can be looked into is the forward or backward tilt of the detector. If the detector is tilted in either one of these directions it can lead to a missallocation of hits, in turn affecting track fitting since CORAL assumes the detector to be perfectly aligned. This misallocation can be fixed by varying the pitch of the detector which is the distance between the readout strips. Even though the pitch of the detector is fixed by construction, the movement simply mimics the tilt of the detector and is generally of the order of few μm . Although the expected impact is very small it is something which can be looked into more since it is already operational in Millepede. A future z positional alignment is also available and can also be looked into in the future.

MC Reconstruction

The second task which was performed during this thesis is the reconstruction of the MC simulation for the 2018 setup in CORAL. This involved transforming the output of the simulation which is obtained from the collaboration to a format which is compatible with CORAL. The reconstruction is confirmed to be working. As a proof of principle the reconstructed beam momentum distribution is checked and confirmed to be reasonable. An attempt was also made to check the A' reconstruction by looking at the angular distribution of its decay products. The distribution was as expected for the simulated A' mass $m_{A'}$. The MC simulation is also described briefly in the thesis.

Outlook

The angular dependence of the fitted beam momentum needs to be looked into further. This might add to the uncertainties during the determination of the reconstructed beam momentum. It seems to be related to the track fitting algorithm used by CORAL. Further rare dimuon events, $e^-Z \rightarrow e^-Z\gamma; \gamma \rightarrow \mu^+\mu^-$ can be used to estimate the efficiency of the MC reconstruction in CORAL. Such events could not be observed during this thesis since the current MC sample which was reconstructed is too small. Bigger samples of simulation already exist and can be processed in the future. Even though the reconstruction was done for the visible mode setup, it is also functional for the invisible mode since all of the detectors implemented are the same except for the WCAL. Hence, MC reconstruction for the invisible mode can be easily done by just plugging in the setup specific detectors table. The results of this thesis help further the goal of performing a full physics A' analysis in CORAL in the future.

Bibliography

- [1] I. Cholis, D. P. Finkbeiner, L. Goodenough, and N. Weiner, *The PAMELA positron excess from annihilations into a light boson*, Journal of Cosmology and Astroparticle Physics **2009** no. 12, (2009) 007–007,
<http://dx.doi.org/10.1088/1475-7516/2009/12/007>.
- [2] NASA, *Credit: X-ray: NASA/CXC/CfA/M.Markevitch et al.; Optical: NASA/STScI; Magellan/U.Arizona/D.Clowe et al.; Lensing Map: NASA/STScI; ESO WFI; Magellan/U.Arizona/D.Clowe et al.*),
<https://chandra.harvard.edu/photo/2006/1e0657/more.html>.
- [3] KATRIN Collaboration, M. Aker et al., *An improved upper limit on the neutrino mass from a direct kinematic method by KATRIN*, Phys. Rev. Lett. **123** no. 22, (2019) 221802, [arXiv:1909.06048](https://arxiv.org/abs/1909.06048) [hep-ex].
- [4] L. R.-I. Natalie Wolchover, *Evidence of a ‘Fifth Force’ Faces Scrutiny*,
<https://www.quantamagazine.org/new-boson-claim-faces-scrutiny-20160607/>.
- [5] *Recent results of the NA64 experiment at the CERN SPS*, vol. 212 of *European Physical Journal Web of Conferences*. Mar, 2019.
- [6] NA64 Collaboration, D. Banerjee et al., *Search for invisible decays of sub-GeV dark photons in missing-energy events at the CERN SPS*, Phys. Rev. Lett. **118** no. 1, (2017) 011802, [arXiv:1610.02988](https://arxiv.org/abs/1610.02988) [hep-ex].
- [7] D. Banerjee, P. Crivelli, and A. Rubbia, *Beam Purity for Light Dark Matter Search in Beam Dump Experiments*, Advances in High Energy Physics **2015** (2015) .
- [8] S. N. Glinenko, *Search for MeV dark photons in a light-shining-through-walls experiment at CERN*, Phys. Rev. **D89** no. 7, (2014) 075008, [arXiv:1308.6521](https://arxiv.org/abs/1308.6521) [hep-ph].
- [9] E. Depero et al., *High purity 100 GeV electron identification with synchrotron radiation*, Nucl. Instrum. Meth. **A866** (2017) 196–201, [arXiv:1703.05993](https://arxiv.org/abs/1703.05993) [physics.ins-det].

Bibliography

- [10] D. Banerjee, V. Burtsev, A. Chumakov, D. Cooke, P. Crivelli, E. Depero, A. Dermenev, S. Donskov, R. Dusaev, T. Enik, and et al., *Search for a Hypothetical 16.7 MeV Gauge Boson and Dark Photons in the NA64 Experiment at CERN*, Physical Review Letters **120** no. 23, (2018), <http://dx.doi.org/10.1103/PhysRevLett.120.231802>.
- [11] NA64 Collaboration Collaboration, S. Glinenko, *NA64 Status Report 2019*, Tech. Rep. CERN-SPSC-2019-024. SPSC-SR-255, CERN, Geneva, Jun, 2019.
<https://cds.cern.ch/record/2677228>.
- [12] G. Charpak, J. Derré, Y. Giomataris, and P. Rebougeard, *Micromegas, a multipurpose gaseous detector*, Nuclear Instruments and Methods in Physics Research Section A: Accelerators, Spectrometers, Detectors and Associated Equipment **478** no. 1, (2002) 26 – 36, <http://www.sciencedirect.com/science/article/pii/S0168900201017132>, Proceedings of the ninth Int. Conf. on Instrumentation.
- [13] F. Sauli, *Principles of Operation of Multiwire Proportional and Drift Chambers*,
- [14] D. Banerjee et al., *Performance of Multiplexed XY Resistive Micromegas detectors in a high intensity beam*, Nucl. Instrum. Meth. **A881** (2018) 72–81, [arXiv:1708.04087 \[physics.ins-det\]](https://arxiv.org/abs/1708.04087).
- [15] F. Sauli, *The gas electron multiplier (GEM): Operating principles and applications*, Nuclear Instruments and Methods in Physics Research Section A: Accelerators, Spectrometers, Detectors and Associated Equipment **805** (2016) 2 – 24, <http://www.sciencedirect.com/science/article/pii/S0168900215008980>, Special Issue in memory of Glenn F. Knoll.
- [16] A. B. et al., *Design, construction and test of a GEM-detector*. PhD thesis, 2008. Technical Thesis, Technical University Munich.
- [17] B. Ketzer et al., *Triple GEM tracking detectors for COMPASS*, IEEE Trans. Nucl. Sci. **49** (2002) 2403–2410.
- [18] M. Hösgen, *GEM Detectors for the Tracking System of the Missing Energy Experiment NA64 at CERN SPS*. Master thesis, University of Bonn, 2017. BONN-IR-2017-March2017.
- [19] DESY, *DESY TPC information*,
https://flc.desy.de/tpc/basics/gem/index_eng.html.
- [20] F. Murtas, G. Croci, A. Pietropaolo, G. Claps, C. Frost, E. Cippo, D. Raspino, M. Rebai, N. Rhodes, E. Schooneveld, M. Tardocchi, and G. Gorini, *Triple GEM gas detectors as real time fast neutron beam monitors for spallation neutron sources*, Journal of Instrumentation - J INSTRUM **7** (2012) .

Bibliography

- [21] J. F. Kenney and E. S. Keeping, (1962) "Linear Regression and Correlation." Ch. 15 in *Mathematics of Statistics , Pt. 1, 3rd ed.* Princeton, NJ: Van Nostrand, pp. 252-285, 1962.
- [22] S. M. Stigler, *Gergonne's 1815 paper on the design and analysis of polynomial regression experiments*, Historia Mathematica **1** no. 4, (1974) 431 – 439, <http://www.sciencedirect.com/science/article/pii/0315086074900330>.
- [23] R. Fruhwirth, *Application of Kalman filtering to track and vertex fitting*, Nucl. Instrum. Meth. **A262** (1987) 444–450.
- [24] P. Astier, A. Cardini, R. D. Cousins, A. A. Letessier-Selvon, B. A. Popov, and T. G. Vinogradova, *Kalman Filter Track Fits and Track Breakpoint Analysis*, Nucl. Instrum. Methods Phys. Res., A **450** no. physics/9912034. 1, (2000) 138–54, <https://cds.cern.ch/record/412374>.
- [25] I. Kisel, *Advances in tracking and trigger concepts*, Journal of Physics: Conference Series **523** (2014) 012022.
- [26] N. Ahmed, *Spurrekonstruktion im NA64 Experiment zur Suche nach Dunkler Materie*. PhD thesis, 2018. Bachelor Thesis, University Bonn.
- [27] V. Blobel, *Software alignment for tracking detectors*, Nucl. Instrum. Meth. **A566** (2006) 5–13, http://www.desy.de/~blobel/blobel_align.pdf.
- [28] B. V. and DESY, *Millepede II*, <http://www.desy.de/~kleinwrt/MP2/doc/html/index.html>.
- [29] V. Blobel and C. Kleinwort, *A New method for the high precision alignment of track detectors*, in *Advanced Statistical Techniques in Particle Physics. Proceedings, Conference, Durham, UK, March 18-22, 2002.* 2002. arXiv:hep-ex/0208021 [hep-ex]. <http://www.ippp.dur.ac.uk/Workshops/02/statistics/proceedings/blobel1.pdf>.
- [30] S. Blusk, O. Buchmuller, A. Jacholkowski, T. Ruf, J. Schieck, and S. Viret, eds., *Proceedings, first LHC Detector Alignment Workshop, CERN, Geneva, Switzerland, 4-6 September 2006.* 2007. <http://cdsweb.cern.ch/record/970621>.
- [31] H. Pereira Da Costa, *Développement de chambres à dérive pour les hauts flux dans l'expérience COMPASS*, 2001. <http://cds.cern.ch/record/1204557>. Presented on 23 Nov 2001.
- [32] S. N. Glinenko, D. V. Kirpichnikov, M. M. Kirsanov, and N. V. Krasnikov, *The exact tree-level calculation of the dark photon production in high-energy electron scattering at the CERN SPS*, Phys. Lett. **B782** (2018) 406–411, arXiv:1712.05706 [hep-ph].

Bibliography

- [33] The NA64 Collaboration Collaboration, D. Banerjee, V. E. Burtsev, A. G. Chumakov, D. Cooke, P. Crivelli, E. Depero, A. V. Dermenev, S. V. Donskov, F. Dubinin, R. R. Dusaev, S. Emmenegger, A. Fabich, V. N. Frolov, A. Gardikiotis, S. G. Gerassimov, S. N. Gninenko, M. Hösgen, A. E. Karneyeu, B. Ketzer, D. V. Kirpichnikov, M. M. Kirsanov, I. V. Konorov, S. G. Kovalenko, V. A. Kramarenko, L. V. Kravchuk, N. V. Krasnikov, S. V. Kuleshov, V. E. Lyubovitskij, V. Lysan, V. A. Matveev, Y. V. Mikhailov, D. V. Peshekhonov, V. A. Polyakov, B. Radics, R. Rojas, A. Rubbia, V. D. Samoylenko, V. O. Tikhomirov, D. A. Tlisov, A. N. Toropin, A. Y. Trifonov, B. I. Vasilishin, G. Vasquez Arenas, and P. Ulloa, *Search for vector mediator of dark matter production in invisible decay mode*, Phys. Rev. D **97** (2018) 072002, <https://link.aps.org/doi/10.1103/PhysRevD.97.072002>.
- [34] Particle Data Group, K. Nakamura, et al., *Review of Particle Physics*, J. Phys. G **37** (2010) 075021, <http://pdg.lbl.gov>.

APPENDIX A

Testing hadronic models

This appendix includes the comparison of residuals obtained from alignment using the previously used method and Millepede. The reduced chi-square comparison plots for the two methods were shown earlier. It also includes the residual versus position plots for the Micromega detectors.

Appendix A Testing hadronic models

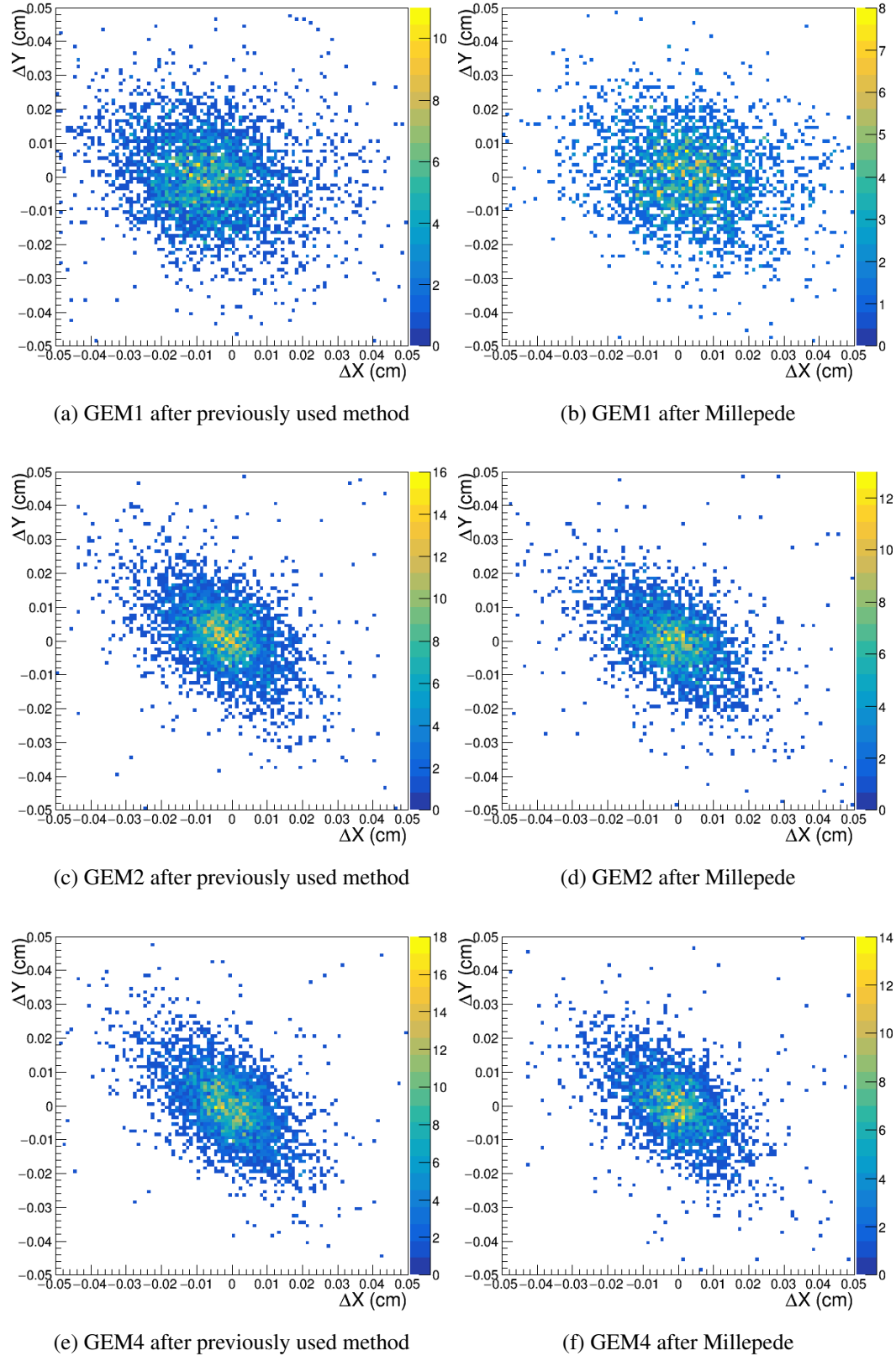


Figure A.1: Residual of GEM detectors.

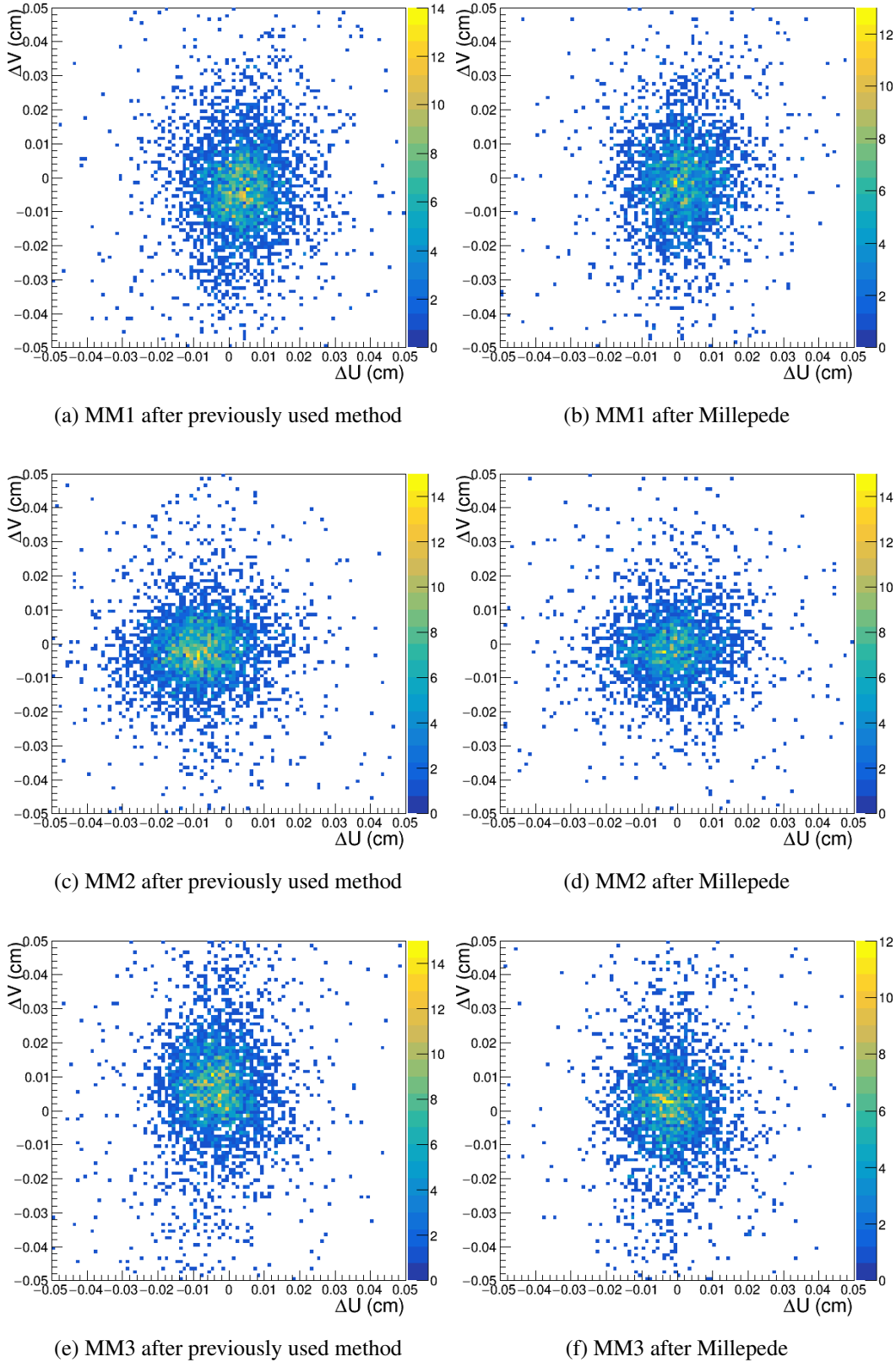


Figure A.2: Residual of Micromega detectors.

Appendix A Testing hadronic models

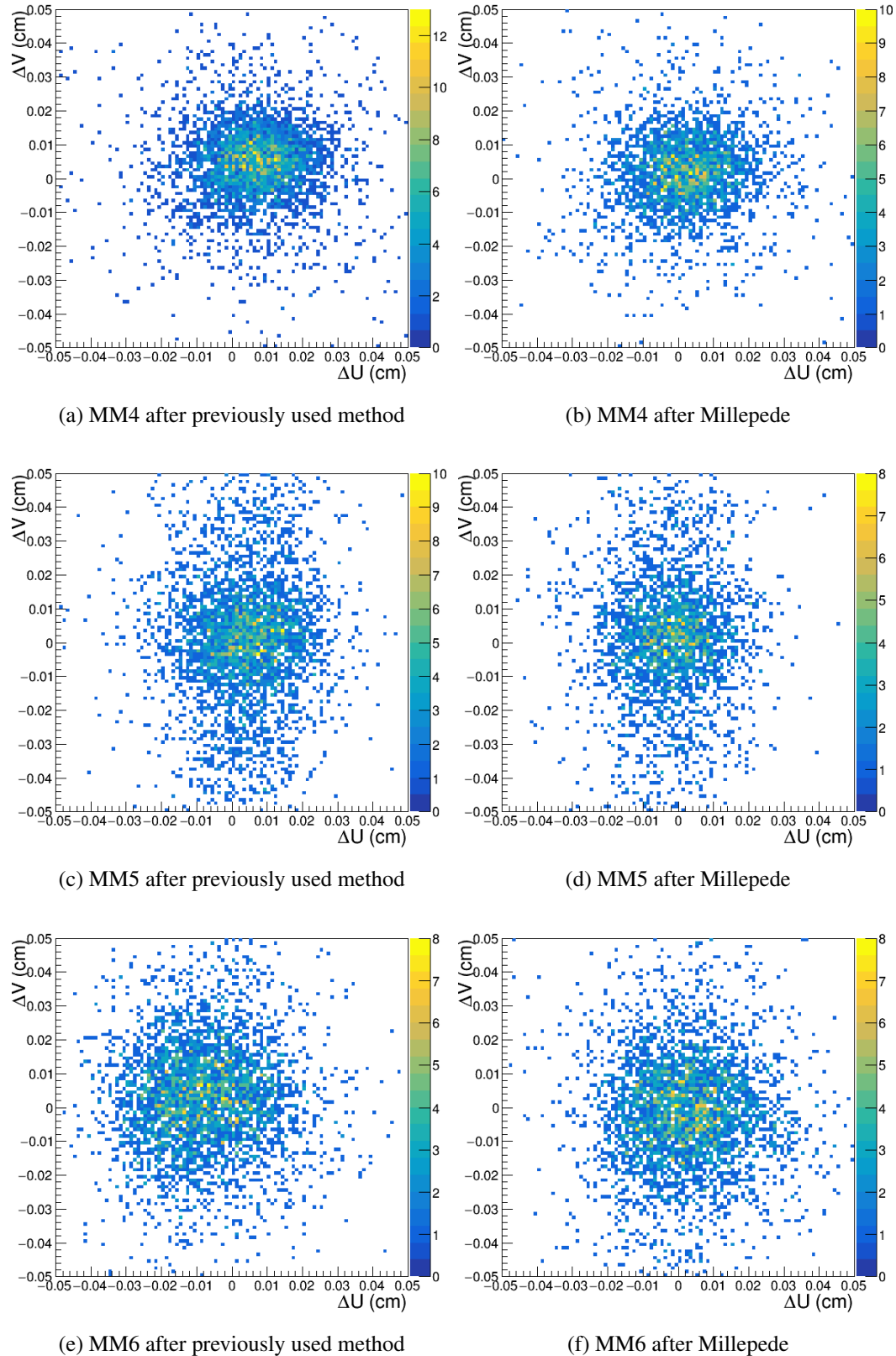


Figure A.3: Residual of Micromega detectors.

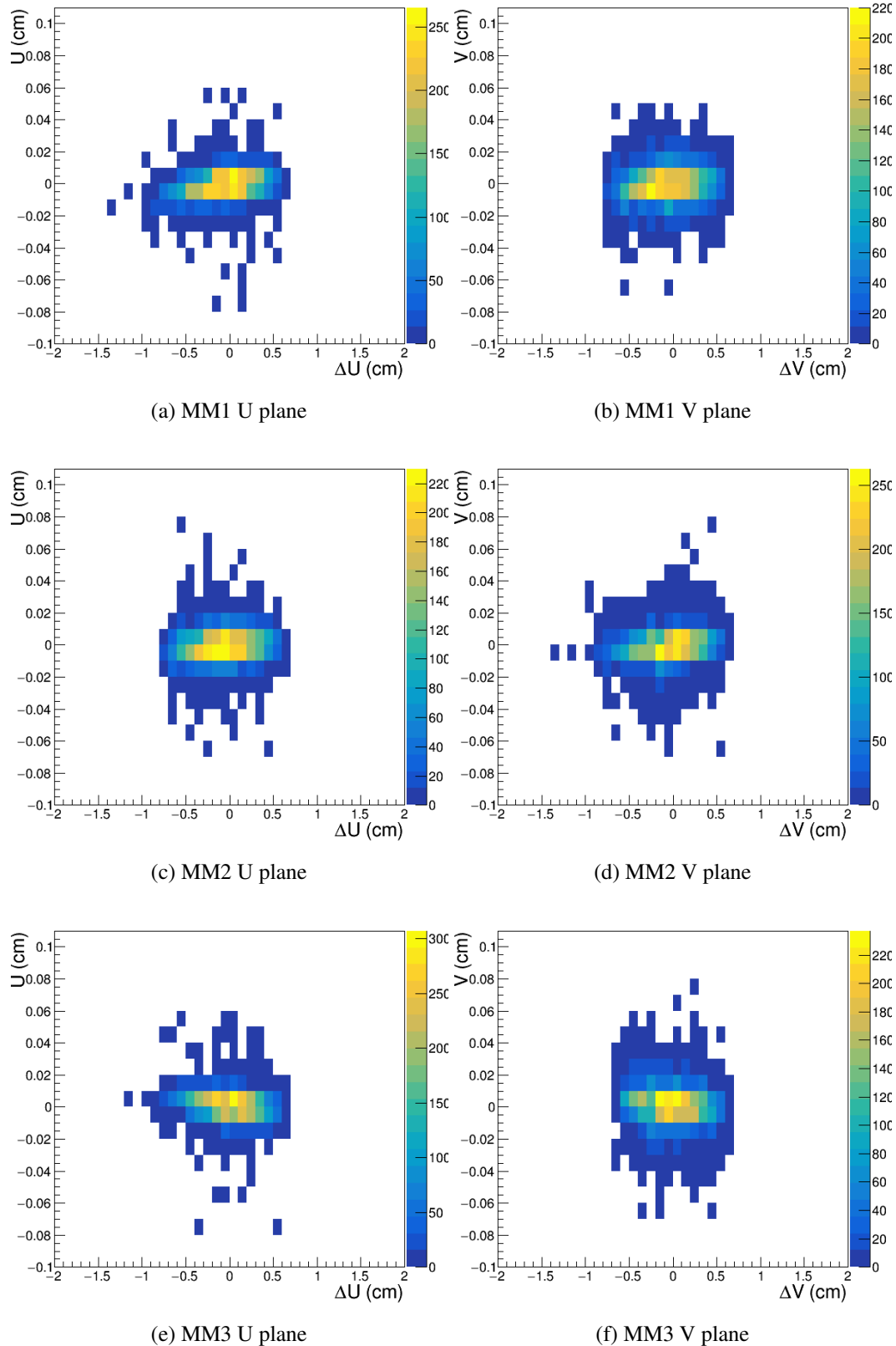


Figure A.4: Residual vs position for Micromega detectors

Appendix A Testing hadronic models

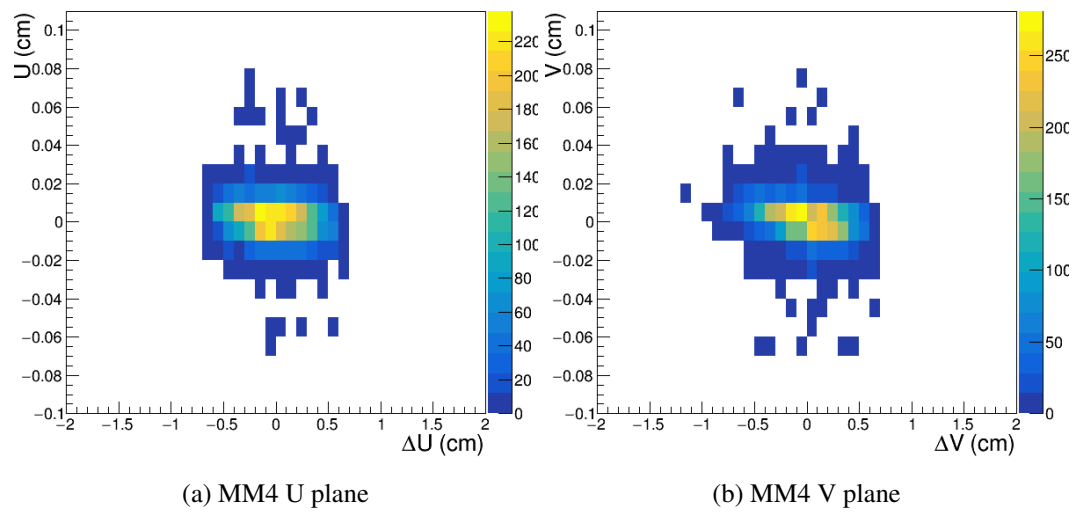


Figure A.5: Residual vs position for MM4

APPENDIX B

Adapting DGH analysis to current Offline

MX01U1	101	0	1	11	149999	0	1	0.001012	4.7205	-0.2347	-17593.5	4.7205	-0.2347	-17593.5	4.7205	-0.2347	-17593.5	0	0	0
Detector Name	Detector -ID	Channel Number	Track -ID	Particle-ID	Particle Energy (MeV)	Time	Beta	Energy Deposited (MeV)	Hit position (X) (cm)	Hit position (Y) (cm)	Hit position (Z) (cm)	Primary hit pos. (X) (cm)	Primary hit pos. (Y) (cm)	Primary hit pos. (Z) (cm)	Last hit pos. (X) (cm)	Last hit pos. (Y) (cm)	Last hit pos. (Z) (cm)	Momentum (X)	Momentum (Y)	Momentum (Z)

Figure B.1: Snippet of the format fed to CORAL

The above figure is a snippet of the modified format which was fed to CORAL for the tracking detector. The line in black is the part which was actually fed to CORAL in a compressed plain text format. The second line in the figure gives a description about the values. The green colour is an indication that the information was available in the output of the simulation while the ones in red were not available and were substituted by some reasonable values. As it can be seen in the figure each plane of the tracking detector is fed individually. For CORAL, the planes were exactly replicated with a shifted z position for each hit. The format for the calorimeters is exactly the same with only the information about the detector name, detector-ID and energy deposited available from the original simulation while the rest is replaced with zero.

List of Figures

1.1	Positron fraction measured by PAMELA (red) along with a theoretical model (black) [1]	1
1.2	Composite image of the bullet cluster. The x-ray emission recorded by Chandra telescope is shown in pink. The blue overlay is the mass distribution of the clusters calculated from gravitational lensing effects. [2].	5
1.3	Scatter plot of fit values for the neutrino mass square and the effective β -decay endpoint E0 together with 1- σ (black) and 2- σ (blue) error contours around the best fit point (cross). [3]	5
1.4	Hypothesized X17 Boson production [4]	5
2.1	Visible mode	25
2.2	Invisible mode	25
2.3	Current limits for invisible mode for 90% C.L. exclusion region in the $(m_{A'}, \epsilon)$ plane [5].	26
2.4	Current limits for invisible mode for 90% C.L. exclusion region in the $(m_{A'}, \epsilon)$ plane. The blue plane is with 2017 data and the dotted line is with 2017+2018 data for NA64. The red line is the region that might explain the X17 boson [5].	26
4.1	Invisible mode setup [6]	35
4.2	Visible mode setup 2017 [10]	36
4.3	Visible mode setup 2018-top view [11]	36
5.1	Left: Strip dimensions of the modules, Right:NA64 Micromega's working principle [14]	40
5.2	A sketch of GEM field lines [19].	41
5.3	Schematic of a triple GEM detector along with the working principle [20] .	41
5.4	Linear regression pictorially.	42
5.5	Pictorial representation of the working principle of a Kalman filter [25]. .	43
6.1	Pictorial representation of the previously used method	48
6.2	Fitting of the residual for the X plane of GEM4	49
6.3	CORAL implementation of Millepede. The black lines signify the order of the steps while the green and red lines depict output and input respectively.	51
6.4	Charge over momentum distribution of all fitted tracks during alignment .	53

List of Figures

6.5	Residual of GEM detectors	55
6.6	Residual of Micromega detectors	56
6.7	Residual of Micromega detectors	57
6.8	χ^2_{red} comparison before and after Millepede alignment implementation . . .	58
6.9	χ^2_{red} comparison of previously used method with Millepede alignment im- plementation	58
6.10	Residual of GEM detectors with downstream Micromegas switched off . . .	59
6.11	Residual vs position for GEM detectors	61
6.12	Angular alignment	62
6.13	χ^2_{red} comparison before and after Millepede T alignment implementation .	62
7.1	Number of simulated signal events at two A' masses as a function of Dark Photon energy [32]	66
7.2	Track reconstruction display from CORAL.	69
7.3	Reconstructed beam momentum in CORAL along with fit parameters. . . .	70
7.4	Fitted beam momentum vs dip angle of incoming track.	71
7.5	Fitted beam momentum vs azimuthal angle of incoming track.	72
7.6	Angle between the outgoing e^+e^- tracks	73
8.1	χ^2_{red} distribution for selected tracks showing the impact of Millepede alignment.	75
A.1	Residual of GEM detectors.	82
A.2	Residual of Micromega detectors.	83
A.3	Residual of Micromega detectors.	84
A.4	Residual vs position for Micromega detectors	85
A.5	Residual vs position for MM4	86
B.1	Snippet of the format fed to CORAL	87